JNC TN9400 2000-021

Enhancement of Nondestructive Evaluation Techniques for Magnetic and Nonmagnetic Structual Components

(Doctoral Fellow Report)

March 2000

O-ARAI ENGINEERING CENTER

JAPAN NUCLEAR CYCLE DEVELOPMENT INSTITUTE

Ⓦ

JNC TN9400 2000 – 021
March, 2000

Enhancement of Nondestructive Evaluation Techniques for Magnetic and Nonmagnetic Structural Components

(Final Report for Doctoral Fellowship)

Zhenmao Chen*

Abstract

In this report, research works performed in the Structural Safety Engineering Group of OEC/JNC are summarized as the final report of the doctoral fellowship. The main objective of this study is for the enhancement of the nondestructive evaluation techniques for structural components of both magnetic and nonmagnetic material. Studies in three topics have been carried out aiming at the quantitative evaluation of crack with the eddy current testing and the validation of a natural magnetic field based NDE method for detecting mechanical damages in a paramagnetic material. In the first part of the study, an approach to the reconstruction of the natural crack was proposed and implemented with an idealized crack model for its validation. In the second part, the correlation of the natural magnetization and the mechanical damages in the SUS304 stainless steel was investigated by using an experimental approach. In part 3, an inverse method of the measured magnetic fields is proposed for the reconstruction of magnetic charges in the inspected material by using an optimization method and wavalet.

As the first work, an approach to the reconstruction of an idealized natural crack of non-vanishing conductivity is proposed with use of signals of eddy current testing. Two numerical models are introduced at first for modeling the natural crack in order to represented it with a set of crack parameters. A method for the rapid prediction of the eddy current testing signals coming from these idealized cracks is given then by extending a knowledge based fast forward solver to the case of a non-vanishing conductivity. Based on this fast forward solver, the inverse algorithm of conjugate gradient method is updated to identify the crack parameters. Several examples are presented finally as a validation of the proposed strategy. The results show that both the two numerical models can give reasonable reconstruction results for signal of low noise. The model concerning the touch of crack surfaces with a conducting band region surrounded by the crack edge, however, is proved more efficient than the model using a conductivity distribution from the point of view of both reconstruction speed and accuracy.

In the second part, an experimental study on the behaviors of the magnetization induced by mechanical damages is carried out. By introducing mechanical damages to a test-piece with a tension or/and a zero-tension fatigue testing and measuring the corresponding leakage flux signal, natural magnetization change is proved and found increasing with the mechanical damages (viz. plastic deformation or fatigue damages) though a saturation occurs when damage gets too large. From the experimental results of fatigue testing

utilizing test-pieces with a central slit, it was verified that observing the natural leakage flux density (leakage flux without applying external magnetic field) is a reasonable way to identify fatigue cracks. A feature parameter (area of the $\varepsilon \sim B$ hysteresis curve) of the in-situ magnetic field signal measured during the fatigue testing is proposed for predicting the fatigue damages, which is found depending on the cyclic number of the applied loading. At last, residual magnetic fields of a magnetized test-piece are also measured and found depending on the applied plastic deformation in case that the plastic strain is not too small. From these experimental results, it is found that the approach detecting natural magnetization is applicable for monitoring the damage status though it may be not efficient for a scanning inspection concerning its small signal magnitude. On the other hand, the method employing permanent magnet is robust against the environment noise but possibly not valid for the ISI of a structural component with a relative low damage level. For practical application, efforts to evaluate the feasibility of the proposed method are necessary for more testing conditions especially its suitability in a practical environment.

For reconstructing the magnetic charges induced by mechanical damages in a test piece of SUS304 stainless steel, inversion methods base on the optimization method and wavelet are proposed and validated by using the measuring results of the second part. The approach for solving this typical ill-posed inverse problem is selected as a way in the least square method category. Concerning the ill-poseness of the system of equations, an iteration algorithm is adopted to its solving in which the designations of initial profile and the total number of iterations are taken as the means of regularization. From examples using simulated input data, it is verified that the approach gives good reconstruction results in case of signals with a relative high S/N ratio. For improving the robustness of the proposed method, a Galerkin procedure with base functions chosen as the Daubechies' wavelet is also developed for discretizing the governing equation. By comparing the reconstruction results of the least square method and those using wavelet discretization, it is found that the wavelet used approach is more feasible in the inversion of noise polluted signals. Moreover, the selection of the maximum iteration number and the weight coefficients used in the objective function are also discussed. Reconstruction of 1-D and 2-D magnetic charges with the least square strategy and reconstruction of an 1-D problem with the wavelet used method are carried out from both simulated and measured magnetic field signals, which in turn, are used as the verification of the suitability of the proposed inversion strategy.

---

* Doctoral Fellow, Structure Safety Engineering Group, OEC/JNC

JNC TN9400 2000－021
２０００年　３月

磁性及び非磁性構造物における非破壊検査技術の向上
(博士研究員終了報告)

陳 振茂 *

要旨

本報告書はJNCにおいて行われた２年間のポストドクター研究の成果を取りまとめたものである。本研究は磁性及び非磁性の構造物を対象に電磁非破壊検査法の向上または新規開発を目指して、渦電流探傷法を用いた自然き裂の形状再構成及び損傷誘起磁化現象の解明と非破壊検査への応用に関する研究を実施した。渦電流検査法の向上には自然き裂の形状を再構成するアプローチを提案し、理想化したき裂モデルに対して再構成を行うことによってその有効性を実証した。自然磁化に関する研究では損傷誘起磁化と損傷の相関の解明及び弱磁性体のSUS304構造物の非破壊検査への適用妥当性を試験手法で評価した。また、測定した磁束漏洩信号から材料内部の磁化分布(損傷の状態と相関する)を再構成するために、最適化手法及びウェーブレットを用いた手法を提案し、実際に測定したデータの逆解析を行った。解析した結果はコロイド法によって計測した磁化に分布と定性的によく一致し、提案手法の有効性を確認した。具体的な内容は次に述べる。

渦電流探傷信号に基づいた自然き裂の逆同定に関して接触き裂の再構成手法を提案・検証した。まず、自然き裂を離散化するために２種類のき裂モデルを提案し、それに基づいてき裂によるECT信号及びその勾配を高速且つ高精度的に計算する手法を開発した。更に上記順問題の高速ソロバー及びモデル化した自然き裂に基づき、最適化手法の共役勾配法を改良し、異なる種類のき裂パラメータを同時に逆推定することに成功した。具体的に矩形き裂に対して再構成を行った結果、２種類のき裂モデル共に接触のあるき裂の再構成に有効であることを実証した。但し、接触がき裂の境界部に限った２番目のモデルはより効率よく再構成することができると判った。本研究の結果は、表面き裂の非破壊検査技術の向上に貢献することが期待できる。

次にSUS304ステンレス鋼における自然磁化と機械損傷の相関に関する試験研究を実施した。単純引張試験及び両振疲労試験を用いて試験片に機械損傷を与え、フラクスゲートセンサーで試験中及び除荷後の磁化特性を測定した。その結果外部磁場をかけなくても塑性変形や疲労損傷により自然磁化が発生し、損傷の増加と伴い飽和することが明らかにした。切欠試験片に疲労き裂を入れた試験から、自然磁化は特に疲労き裂の検査に有効であることが判った。更に疲労試験中測定した磁場信号の処理により、疲労損傷の検出に適用可能な信号の特徴量(磁場・ひずみヒシテリシス曲線の面積)を提案した。最後に塑性変形を与えた試験片に対して永久磁石励磁による残留磁化の分布を測定し、残留磁化は塑性変形が十分大きくなると増加する傾向があると判った。上記内容から、損傷誘起自然磁化は絶対値が小さいものの、特徴量の抽出やセンサーの工夫によって損傷状態の監視に十分適

用可能であると考えられる。一方、自然磁化の測定は走査検査への適用のためにまた努力する必要があるが、これに対して残留磁化に基づいた手法は有効である可能性が高い。なお、提案手法を実機環境への応用に至るまでは、異なる試験条件下の挙動や実環境ノイズの影響の確認などさらなる研究を重ねる必要があると考えられる。

更に自然磁束漏洩から損傷を非破壊的に検査する研究の一環として、測定した磁束信号より材料における損傷による磁荷の再構成を行った。この代表的な非適切問題に最小自乗法に基づいた手法を適用した。初期値や反復計算の回数を適切化の手法とした上反復計算アルゴレズムを利用して得られた線形方程式を解くことに成功した。シミュレーションデータを用いて再構成を行った結果、本手法はノイズの少ない信号に対して有効であることを実証した。また、ノイズに対するロバースト性を向上するために、ウェーブレットに基づいたガラーキン法を積分方程式の離散化に用いられた。最小自乗法の結果と比べることにより、ウェーブレットを用いた手法はS/N比の低い信号に対しても有効であることを明らかにした。更に、反復計算の回数や重み係数の選び方について検討した。実際に最小自乗法は1次元及び2次元問題、ウェーブレットを用いた手法は1次元問題の磁荷分布の再構成に適用し、提案した手法の妥当性を確認した。

* 大洗工学センター、Na安全工学試験部、機器・構造安全工学グループ

Contents

List of Tables

List of Figures

List of Notations

$\boldsymbol{A}$	Magnetic vector potential
$\boldsymbol{A}^f$	Perturbation of magnetic vector potential
$\boldsymbol{A}^u$	Unflawed magnetic vector potential
ϕ	Electric scalar potential
ϕ^f	Perturbation of electric scalar potential
ϕ^u	Unflawed electric scalar potential
$\boldsymbol{B}_0$	Source magnetic induction intensity vector
$\boldsymbol{E}$	Electric field intensive vector
$\boldsymbol{E}^f$	Perturbation of Electric field intensive vector
$\boldsymbol{E}^u$	Unflawed electric field intensive vector
$\widetilde{\boldsymbol{E}}$	Joint electric field intensive vector
μ, μ_0	Permeability of the conductor and free space
$\sigma(\mathbf{r}), \sigma_0$	Conductivity of the conductor and free space
$\mathbf{m}(\mathbf{r})$	Magnetization vector
$q(\mathbf{r})$	Magnetic charge
$\phi_{n.j}(x)$	Wavelet function

List of Abbreviations

BEM	Boundary Element Method
CGM	Conjugate Gradient Method
CCT	Central Crack Tensile test-piece
ECT	Eddy Current Testing
FBR	Fast Breeder nuclear Reactor
EDM	Electro-Discharge Machining
FEM	Finite Element Method
FG	Flux-Gate sensor
ID	Inner Defect
IGA	InterGranulur Attack
ISI	In-Service Inspection
JSAEM	Japan Society of Applied Eletromagnetics and Mechanics
MFM	Magnetic Force Microscope
NDE	Non-Destructive Evaluation
NDT	Non-Destructive Testing
PWR	Pressurized Water Reactor
SCC	Stress Corrosion Crack
SEM	Scanning Electronic Microscope
SG	Steam Generator
TEM	Transmission Electronic Microscope

Chapter 1

Introduction

Chapter 1

Introduction

Nowadays, for enhancing the safety of various critical structure systems such as the machinery of a nuclear power plant, more reliable NonDestructice Evaluations (NDE) are strongly expected by the related industry society. In addition, the improvement of the inspection efficiency is also getting important as it is indispensable for dealing with the costdown issue, which, as well known, may affect the future of the related industries. A quantitative evaluation of cracks and an efficient technique for inspecting the damage state before crack initiation are typical examples of such needs. From the point of view of the merits of the electromagnetic nondestructive evaluation such as no contact, high speed, high sensitivity for surface breaking crack, more and more research activities are performed on this subject aiming at to upgrade the present techniques.

In the electromagnetic NDE, the eddy current testing and the method of magnetic leakage flux are usually applied in the practical inspection. The ECT is efficient in the inspection of massive structural components and is currently applied in the ISI of many critical machinery and in the manufacturing control. The state-of-the-arts of the present ECT technique is that only cracks with a relative large depth possibly be detected and the sizing of the crack can only be performed based on a calibration method. On the other hand, an increasing requirement on the NDE means is to predict the crack before its initiation. However, there is still no satisfactory method for this purpose from the point of view of practical application. Recently, a phenomenon of damage induced magnetization is found for the SUS304 stainless steel and some carbon steels. Considering that the magnetic properties of the material depending on the local microstructure of the material, it is possibly to detect the mechanical damage by measuring the magnetic flux leakage as the damages affect the microstructure of material significantly.

Based on these backgrounds, two study topics are chosen as the research subjects of the present doctoral fellowship. One of them is the upgrade of the ECT technique by establishing an approach for the reconstruction of natural crack in a nonmagnetic material (Inconel 600). Considering the complexity of the natural crack, the modeling of the crack is performed at first. The inverse analysis method for reconstructing of the artificial crack then was extended to solve the parameters of the crack shape, position and conductivity.

The method is implemented for two crack models and satisfactory results were obtained for simulated noise polluted ECT signals. For the study on the correlation of the natural magnetization and the damage status in the material of SUS304 stainless steel, an experimental work for investigating the feature of the natural magnetization, and an inversion analysis for reconstructing the distribution of the magnetization in the material from the measured magnetic field signals are performed. In practical, the natural magnetic flux signals from test-pieces, in which damages from tensile or/and fatigue testing were introduced, were measured by using a film type FG sensor both during the loading procedure and after unloading the test-piece. The residual magnetic fields of the damaged test-piece after magnetized with a permanent magnet are also performed to investigate the possibility to apply it to the damage detection in the SUS304 stainless steel. In the inverse analysis of the measured magnetic field, the parameter to be reconstructed was chosen as the magnetic charge instead of the magnetization vector in order to reduce the ill-poseness of the problem. By using an optimization method and wavelet, the charge distribution is reconstructed from the magnetic field detected from a test-piece containing a fatigue crack, which agrees well with that observed using a colloidal method and in turn, verified the validity of proposed methods.

In the following, the details of these three works are given respectively in the chapter 2, chapter 3 and chapter 4. Concluding remarks and prospect work are summarized at the last part of the report.

Chapter 2

An Approach to the Reconstruction of a Natural Crack using Signals of Eddy Current Testing

Chapter 2

An Approach to the Reconstruction of a Natural Crack using Signals of Eddy Current Testing

2.1. Introduction

Shape reconstruction of cracks in a structural component is an important issue for ensuring safety of the whole engineering structure (e.g. steam generator tubing in a power plant of pressurized water reactor). In addition, a reliable prediction of crack profiles is also indispensable in the efforts to extend the ISI (In-Service Inspection) period which, as well known, connects with a huge economic benefit. The conventional ways of non-destructive testing, however, are still difficult to satisfactorily fulfill such a requirement on the quantitative nondestructive evaluation. Hence, researches are still necessary for upgrading the present NDT technologies in order that the quantitative inspection can be realized with both a reasonable precision and a high efficiency.

As an effort to enhance the technique of crack reconstruction using eddy current testing (ECT), a database used scheme was recently developed for artificial cracks embedded in a conducting tube by incorporating a novel fast forward solver to a reconstruction algorithm of the conjugate gradient method. The validity of the approach has been verified by reconstructing artificial cracks of electro-discharge machining (EDM) from both simulated and measured ECT signals[1],[2]. To apply this method to the practical inspection of surface breaking natural cracks such as a SCC (Stress Corrosion Crack) or an IGA (Inter-Granular Attack), however, more work is needed for both the modeling of natural cracks and the improvement of inversion algorithm. As described in Ref.[3], the reconstruction of multiple cracks and a crack with non-vanishing conductivity are fundamental steps to realize the inversion of practical natural cracks. Bearing mind these backgrounds, we develop an approach for the reconstruction of a single crack of non-vanishing conductivity in this paper. At first, two numerical models are proposed for describing both the shape and conductivity

features of a crack. The rapid simulation of ECT signals arisen from these idealized cracks is considered then by extending the knowledge based fast forward scheme to the case of a touched crack. Thirdly, the crack parameters are solved by using a way of optimization analysis which is developed based on a modified algorithm of the conjugate gradient method and a upgraded code of the rapid forward scheme. Several cracks of typical profiles are successfully reconstructed on a personal computer which in turn, verified the validity of the proposed strategy.

2.2. Modeling of a crack with non-vanishing conductivity

As shown in Fig.2.1, a natural crack usually has a much more complicated geometry than an EDM notch. However, considering features of the fabrication procedure and the application environment, a crack occurred in a SG tube usually appears as an axial or a circumferential one perpendicular to the tube surface. The width of the crack, also, can be assumed varied in a small range. Consequently, it is reasonable to simplify a natural crack as a planar notch of given opening and non-vanishing conductivity at the first step to consider its reconstruction. On the basis of such an assumption, the shape reconstruction of a natural crack becomes a problem to predicate the crack edge curve and/or the conductivity distribution at crack region from the detected pick-up signals.

One of the most direct ways to model a crack is to employ the distribution of conductivity in a selected region which represents the crack edge with a jump of conductivity (hereafter we call it the conductivity model). Usually, such a function of conductivity distribution needs to be discretized in order to treat the crack with a numerical way. A set of box functions is a suitable candidate to be used as the discrete base functions[4],[5]. However, it subjects to a drawback of low approximation order that means a low precision unless enough fine discrete cells are adopted. On the other hand, wavelet functions are recently verified efficient for the expansion of a function with nonstationary property or abrupt change, and the location where jump occurs also can be simply extracted by using the multi-scale analysis technique[6],[7],[8]. Therefore, as the first model for the crack with non-vanishing conductivity, we describe it with a two dimensional function supported within a selected region, and assume the conductivity unchanged in the direction perpendicular to the crack plane. In this case, the distribution of conductivity can be expanded to the following discrete form by employing the Daubechies' wavelet function,

$$\sigma(x,z) = \sum_{k_1}\sum_{k_2} a_{n,k_1k_2}\phi_{n,k_1}(x)\phi_{n,k_2}(z), \tag{2.1}$$

where, $x \in [-l/2, l/2], z \in [-h/2, h/2]$ with l, h being respectively the length and thickness of the selected region where cracks possibly happen. $\phi_{n,k_1}(x)$ and $\phi_{n,k_2}(z)$ are scaling functions with resolution level n that are expressed by the Daubechies' mother wavelet as $\phi_{n,k}(x) = 2^{n/2}\phi(2^n x - k)$, and k_1, k_2 are shift parameters with ranges,

$$2 - 2N \le k_1 \le 2^n - 1 \tag{2.2}$$

$$2 - 2N \leq k_2 \leq 2^n - 1 \tag{2.3}$$

and N is the index of the adopted Daubechies' mother wavelet.

Considering the features of a surface breaking SCC crack, treating it by the conductivity distribution model obviously lacks of efficiency as the conductivity model is a general one suitable for any planar flaws. The drawback caused by this wide feasibility is that it may lead to a significant decrement on the condition number of the system equations discretized from the corresponding inverse problem. In fact, by observing the broken tube segments where natural cracks exist, it is easy to find that a crack region of non-vanishing conductivity usually is along the crack edge. If we assume the conductivity in this region does not vary significantly, the model illustrated in Fig.2.2, i.e., a crack consisting of two regions of different conductivity separated by an extra edge curve, seems a good approximation of the crack we considered (hereafter we call it two-edge model). Although the two-edge model is valid only for a specified case, it is obviously more suitable in applications than the EDM crack (a cavity model of crack), as the later one may gives a much smaller estimation of crack size, if the conductivity in crack region is not zero. The two-edge model can take into account the effect of the touch occurred between the two crack surfaces in the reconstruction procedure by solving both the conductivity and functions describing the two edge curves. In addition, as the two dimensional crack function adopted in the conductivity model is reduced to two 1-d functions, the condition number of the ill-posed inverse problem can be improved significantly. Practically, the crack parameter for this model can be chosen as σ_1, the conductivity at the conducting band region, and $\mathbf{b}$, the coordinate vector of the discrete points of crack edges.

In the following sections, the rapid scheme for forward analysis and the inverse algorithm for parameter optimization will be described respectively for these two crack models. The suitability of these models will be evaluated by applying them to the shape reconstruction with use of simulated ECT signals and signals containing artificial noise.

2.3. An overview of reconstruction method for an EDM notch

2.3.1 Basic formulation for a forward problem[1]

Upon subtracting the $A - \phi$ formulae about $\mathbf{A}^u, \phi^u$, the vector and scalar potentials of the unflawed conductor, from those about $\mathbf{A}, \phi$, the potentials of a conductor with flaw present, one can obtain the following governing equations about the field perturbation $\mathbf{A}^f, \phi^f$ for a low frequency eddy current problem,

$$\frac{1}{\mu_0}\nabla^2\mathbf{A}^f - \sigma_0(\dot{\mathbf{A}}^f + \nabla\phi^f) = -[\sigma_0 - \sigma(\mathbf{r})](\dot{\mathbf{A}} + \nabla\phi), \tag{2.4}$$

$$\nabla \cdot \sigma_0(\dot{\mathbf{A}}^f + \nabla\phi^f) = \nabla \cdot [\sigma_0 - \sigma(\mathbf{r})](\dot{\mathbf{A}} + \nabla\phi), \qquad (in\ conductor) \tag{2.5}$$

$$\frac{1}{\mu_0}\nabla^2\mathbf{A}^f = 0, \qquad (in\ air) \tag{2.6}$$

where, $\mathbf{A}^f = \mathbf{A} - \mathbf{A}^u$, $\phi^f = \phi - \phi^u$ are the potential perturbations due to the presence of a crack, σ_0 is the conductivity of the host material and $\sigma(\mathbf{r})$ is the distribution of conductivity that is equal to 0.0 in crack region and σ_0 in the conductor. As $[\sigma_0 - \sigma(\mathbf{r})]$ vanishes in the conducting area, after FEM-BEM discretization, the Eqs.(2.4)$\sim$ (2.6) reduces to,

$$\begin{bmatrix} \bar{K}_{11} & \bar{K}_{12} \\ \bar{K}_{21} & \bar{K}_{22} \end{bmatrix} \begin{Bmatrix} q_1^f \\ q_2^f \end{Bmatrix} = \begin{bmatrix} \widetilde{K}_{11} & 0 \\ 0 & 0 \end{bmatrix} \begin{Bmatrix} q_1^f + q_1^u \\ q_2^f + q_2^u \end{Bmatrix}, \tag{2.7}$$

where, $\{q^f\} = \{\mathbf{A}^f, \phi^f\}^T, \{q^u\} = \{\mathbf{A}^u, \phi^u\}^T$ are the potentials at every node, $[\bar{K}]$ is the coefficient matrix of the unflawed conductor, and $[\widetilde{K}]$ is the coefficient matrix corresponding to the terms with $[\sigma_0 - \sigma(\mathbf{r})]$. The unknown potential vector $\{q\}$ was divided into two parts: $\{q_1\}$ are the potential values at the node of crack element and $\{q_2\}$ are the remained unknowns. As $[\sigma_0 - \sigma(\mathbf{r})]$ vanishes in region $\Omega - \Omega_c$, $[\widetilde{K}]$ is written as in Eq.(2.7) where the nonzero submatrix $[\widetilde{K}_{11}]$ corresponds to the cells at the crack region.

Multiplying Eq.(2.7) left by $[H] = [\bar{K}]^{-1}$, we find,

$$\begin{Bmatrix} q_1^f \\ q_2^f \end{Bmatrix} = \begin{bmatrix} H_{11} & H_{12} \\ H_{21} & H_{22} \end{bmatrix} \begin{bmatrix} \widetilde{K}_{11} & 0 \\ 0 & 0 \end{bmatrix} \begin{Bmatrix} q_1^f + q_1^u \\ q_2^f + q_2^u \end{Bmatrix}. \tag{2.8}$$

The equations related to the unknowns $\{q_1^f\}$ can be simply separated from the Eq.(2.8). If we denote $[H_{11}][\widetilde{K}_{11}]$ as $[G]$, and the unit matrix as $[I]$, the relation connecting the unflawed field to the field perturbation in region Ω_c is finally deduced as follows,

$$[I - G]\{q_1^f\} = [G]\{q_1^u\}. \tag{2.9}$$

As the unknowns of Eq.(2.9) are limited to the crack region Ω_c, calculation of the disturbed field $\{q_1^f\}$ using this equation is much faster than the conventional FEM-BEM code. This increment of speed comes from the significantly reduced number of unknowns. The information about the conductor and exciting coils are contained in the coefficient matrices $[H_{11}]$ and $\{q_1^u\}$, that can be calculated *a priori* as they are independent of the crack. Thus, once these fields were calculated and stored in data-bases, there is no need to compute them again in the actual calculation of crack fields. Consequently, the computational burden can be reduced significantly.

The basic difference between the Eq.(2.9) and the conventional schemes using VIM is the different type of unknowns. The application of the potentials makes the interpolation of eddy currents a higher order and makes a new FEM element containing crack edge applicable (this will be explained later). Therefore, the evaluation of a crack which is difficult to be treated by other methods, can be efficiently performed with use of the new scheme.

2.3.2 Establishment of data-bases

From ECT signal, some features of a crack such as the position, length and inner/outer property usually can be estimated roughly with a classification method. Thus, it is not

difficult to choose an area including possible cracks and to subdivide it into a grid of small cells. We calculate the unflawed field at Ω_0 using the conventional FEM-BEM code with the excitation current in the probe or a unit potential acting at one of the nodes in Ω_0 respectively. Storing these results in data-bases, the matrices $[H_{11}]$ and $\{q^u\}$ of Eq.(2.9), which are necessary for the fast evaluation of ECT signal, can be extracted directly from the data-bases for any cracks contained in the region Ω_0. Here the property was used that the field at the crack region excited by a unit source corresponds to a column of the inverse matrix $[H_{11}]$.

In case of a conducting tube that is sufficiently long relative to the probe dimensions, the size of the data-bases can be greatly reduced by considering the shift property of the electromagnetic field. If the exciting points are in the same layer (same radial coordinate), the fields excited at different axial (or circumferential) locations will be the same except a shifted axial (or circumferential) coordinate. Thus, we only need to store the field of sources acting at a radial line in the central cross section of the tube. The field due to a unit source at other nodes can be simply found from these data by shifting the coordinates.

2.3.3 The pick-up signal

As the disturbed field $\{q_1^f\}$ can be considered as the unflawed field induced by current dipoles in crack region, it is convenient to calculate the pick-up signals using the reciprocity theorem[10]. For a self induction pancake coil, the impedance change is written as,

$$\triangle Z = \frac{1}{I^2}\int_{coil} \mathbf{E}^f \cdot \mathbf{J_0} dv = \frac{1}{I^2}\int_{flaw} \mathbf{E}^u \cdot (\mathbf{E}^f + \mathbf{E}^u)(\sigma_0 - \sigma(\mathbf{r}))dv, \qquad (2.10)$$

where $(\sigma_0 - \sigma(\mathbf{r}))(\mathbf{E}^f + \mathbf{E}^u)$ is the current dipoles in flaw region and I is the current per turn in the coil. The calculation of the impedance with Eq.(2.10) requires very little computational work as it can be integrated with the help of the known element coefficient matrices directly. The EMF (Electromotive Force) of a mutual induction probe can also be evaluated by using a similar formula. In this case, the fields induced by a virtual current in pick-up coil have to be incorporated[1].

2.3.4 Introducing of a new FEM element

As the data-base have to be established using the grid of given cells *a priori*, only cracks being made up of the cells can be treated by using these data-bases if homogeneous conductivity is a necessary condition in each FEM element. However, as the permeability and permittivity constants of the SG tubes are the same as those of free space, the electric charge at a conductor surface is negligible small like the neglected displacement current[16] for low frequency problem. Hence, the electromagnetic fields are continuous and the corresponding potentials $\mathbf{A}, \phi$ are approximately one order differentiable at the crack edge. In addition with the fact that small grid cells are usually selected for subdividing Ω_0, it is

reasonable to apply the shape function of a normal FEM element in the interpolation of unknown field even for a cell containing crack edge, i.e. with different media. This treatment is similar to what has been proposed in Ref.[17]. Introducing such a new element can enable us to simply treat cracks with arbitrary shape. In such a case, the difference of the material is taken into account in the element coefficient matrices, as the integration over the whole element is reduced to the part related to the crack region.

2.3.5 Algorithm for the inverse problem[2]

We define the mean-square residual as,

$$\varepsilon(\mathbf{c}) = \sum_{m=1}^{M} |Z_m(\mathbf{c}) - Z_m^{obs}|^2 \tag{2.11}$$

where, $\{c\}$ is the vector of crack shape parameters. $z_m(\mathbf{c})$ and z_m^{obs} are the predicted and observed impedance signals at m-th sampling point respectively. The total data number M is equal to the product of the number of scanning points and the number of frequency.

The selection of an object function is very important when noise or model inaccuracies are present. Usually, some weight coefficients or/and some extra constraint conditions are also introduced in the object function in order to avoid the possible local minimum. In the present problem, as we assume that the initial values of the crack position can be chosen as values not too far from the true shape, it is reasonable to regard the the object function as the mean-square error defined by Eq.(2.11) if S/N ratio is not too small.

We optimize the crack shape vector $\{c\}$ by minimizing the mean-square error with the following iteration,

$$\{c\}_n = \{c\}_{n-1} + a_n\{\delta c\}_n, \tag{2.12}$$

where $\{\delta c\}_n$ is the update direction of n-th iteration, which is chosen as the direction parallel to the derivative vector $\{\frac{\partial \varepsilon}{\partial c_i}\}$ in the steepest descent algorithm. a_n is a step-size parameter determined as the value maximumly reducing the residual. In the conjugate gradient method, the vector $\{\delta c\}$ in Eq.(2.12) is adjusted to a new direction by considering the convergence history in order to accelerate the convergence.

To calculate the derivative $\partial\varepsilon/\partial c_i$, it is efficient to apply the method using adjoint field. The formulae of this method are as follows,

$$\frac{\partial \varepsilon}{\partial c_i} = 2Re\left\{\sum_{m=1}^{M}\{Z_m(\mathbf{c}) - Z_m^{obs}\}^* \frac{\partial Z_m(\mathbf{c})}{\partial c_i}\right\}, \tag{2.13}$$

with the derivatives of impedance signal evaluated with the following equation,

$$\frac{\partial Z_m(\mathbf{c})}{\partial c_i} = -\int_S \mathbf{E}_t^m(\mathbf{r}) \cdot \tilde{\mathbf{E}}_t^m(\mathbf{r}) \frac{\partial s(\mathbf{c},\mathbf{r})}{\partial c_i} ds, \tag{2.14}$$

where, $\tilde{\mathbf{E}}$ is the adjoint electric field. $s(\mathbf{c},\mathbf{r}) = 0$ is the function of the crack edge. The integral region S is a ribbon shaped surface with width equal the crack opening h_0 and along

the crack edge. In Eq.(2.14), the electric field was replaced by its tangential component as no current flows across the conductor surface. For applying the edge equation of $\mathbf{r} = \mathbf{s}(\mathbf{c}, \mathbf{t})$, the Eq.(2.14) becomes,

$$\frac{\partial Z_m(\mathbf{c})}{\partial c_i} = -\int_S \mathbf{E}_t^m(\mathbf{r}) \cdot \tilde{\mathbf{E}}_t^m(\mathbf{r}) \frac{\partial \mathbf{s}(\mathbf{c}, \mathbf{t})}{\partial c_i} \cdot \mathbf{n} d\mathbf{t}, \tag{2.15}$$

where, $\mathbf{n}$ is the normal unit vector at point $\mathbf{t}$.

For SG tubing with crack perpendicular to its surface, the field is self-adjoint that can simplify the Eq.(2.14) further. For step size parameter a_n, it can be calculated with $a_n = P/Q$ and[10],

$$P = Re\left\{\sum_m (Z_m^{n-1} - Z_m^{obs})^* \frac{\partial Z_m^{n-1}}{\partial a_n}\right\}, \qquad Q = \sum_m \left|\frac{\partial Z_m^{n-1}}{\partial a_n}\right|^2. \tag{2.16}$$

2.3.6 Shape parameters of an EDM crack

We limit our problem further to the surface breaking cracks considering the property of ECT. Assuming inner/outer and axial/circumferential properties were known from the phase property of ECT signal prior to the inversion, it is reasonable to express the crack with an open piecewise line like the way described in Fig.2.3. A constraint condition is needed in this discretization to impose the two end points p_1 and p_{n_c} located at the surface of conductor. Written as equation, the discretized edge curve becomes,

$$x(t) = s_1(p_1, ..., p_{n_c}, t) = x_{p_i} + \frac{x_{p_{i+1}} - x_{p_i}}{t_{i+1} - t_i}(t - t_i), \quad t \in [t_i, t_{i+1}] = \Gamma_i, \tag{2.17}$$
$$i = 1, 2, ...n_c$$

$$z(t) = s_2(p_1, ..., p_{n_c}, t) = z_{p_i} + \frac{z_{p_{i+1}} - z_{p_i}}{t_{i+1} - t_i}(t - t_i), \quad t \in [t_i, t_{i+1}] = \Gamma_i, \tag{2.18}$$
$$i = 1, 2, ...n_c - 1$$

where $p_1, .., p_{n_c}$ are n_c points equally spaced at the crack edge. x_{p_i}, z_{p_i} and t_i are the rectangular and curve coordinates of the point p_i respectively. The first and last points are located at the corresponding surface point with same x value. The variation of the edge is expressed by the variation of coordinates as follows,

$$\delta s(\mathbf{c}, \mathbf{r}) = \delta \mathbf{r} = \delta s_1(\mathbf{c}, t)\mathbf{i} + \delta s_2(\mathbf{c}, t)\mathbf{k} = \sum_i \frac{\partial s_1(\mathbf{c}, t)}{\partial x_{p_i}} \delta x_{p_i} \mathbf{i} + \sum_i \frac{\partial s_2(\mathbf{c}, t)}{\partial z_{p_i}} \delta z_{p_i} \mathbf{k}, \tag{2.19}$$

where, $\mathbf{i}, \mathbf{k}$ denote the unit vectors along the x and z direction. Substituting Eq.(2.19) into Eq.(2.14) with $\partial s_1(\mathbf{c}, t)/\partial x_{p_i}$ and $\partial s_2(\mathbf{c}, t)/\partial z_{p_i}$ derived from Eqs.(2.17) and (2.18), the derivatives of the impedance Z_m are expressed in term of the electric field by the following integrals,

$$\frac{\partial \mathrm{Z_m}}{\partial \mathrm{x_{p_i}}} = -\sigma_0 \int_{-\frac{h_0}{2}}^{\frac{h_0}{2}} \left\{ \int_{\Gamma_i} \mathrm{E_{mt}^2} \frac{(\mathrm{t_{i+1}} - \mathrm{t})}{(\mathrm{t_{i+1}} - \mathrm{t_i})} \frac{(\mathrm{z_{p_{i+1}}} - \mathrm{z_{p_i}})}{(\mathrm{t_{i+1}} - \mathrm{t_i})} \mathrm{dt} + \int_{\Gamma_{i-1}} \mathrm{E_{mt}^2} \frac{(\mathrm{t} - \mathrm{t_{i-1}})}{(\mathrm{t_i} - \mathrm{t_{i-1}})} \frac{(\mathrm{z_{p_i}} - \mathrm{z_{p_{i-1}}})}{(\mathrm{t_i} - \mathrm{t_{i-1}})} \mathrm{dt} \right\} \mathrm{dy},$$

$$i = 1, 2, ...n_c \tag{2.20}$$

$$\frac{\partial Z_m}{\partial z_{p_i}} = -\sigma_0 \int_{-\frac{h_0}{2}}^{\frac{h_0}{2}} \left\{ \int_{\Gamma_i} E_{mt}^2 \frac{(t_{i+1} - t)}{(t_{i+1} - t_i)} \frac{(x_{p_i} - x_{p_{i+1}})}{(t_{i+1} - t_i)} dt + \int_{\Gamma_{i-1}} E_{mt}^2 \frac{(t - t_{i-1})}{(t_i - t_{i-1})} \frac{(x_{p_{i-1}} - x_{p_i})}{(t_i - t_{i-1})} dt \right\} dy,$$

$$i = 2, 3, ..., n_c - 1 \tag{2.21}$$

where, the integration along the thickness direction of crack is carried out with the variable y from $-h_0/2$ to $h_0/2$.

If the crack parameter c_i was chosen as the step length of the modification along the normal direction of the crack edge as shown in Fig.2.3, the derivative with respect to this parameter can be obtained by imposing the point p_i move along the normal direction. Thus, the derivative with respect to c_i is equal to the partial derivative at the normal direction $\mathbf{n}_{p_i}$,

$$\frac{\partial Z_m}{\partial c_i} = \nabla Z_m \cdot \mathbf{n}_{pi} = \frac{\partial Z_m}{\partial x_{p_i}} n_{x_{p_i}} + \frac{\partial Z_m}{\partial z_{p_i}} n_{z_{p_i}}. \tag{2.22}$$

Moreover, we only need to choose the point number $n_c = 4$ for dealing with a rectangular crack. In this case, the derivatives with respect to the independent crack parameters (such as, the depth of the crack and the x coordinate of the two ends) can be obtained from the derivatives of Eqs.(2.20) and (2.21) using the transform matrix $[T]$ as,

$$\left\{ \frac{\partial Z_m}{\partial c_i} \right\} = [T] \left[\left\{ \frac{\partial Z_m}{\partial x_{p_i}} \right\}^T, \left\{ \frac{\partial Z_m}{\partial z_{p_i}} \right\}^T \right]^T. \tag{2.23}$$

2.4. Extension of the fast forward strategy

Theoretically, the forward scheme developed for predicting ECT signals of a cavity crack is also suitable for a crack with non-vanishing conductivity if the element with multiple media[1] is applicable for treating the change of conductivity. However, in case of models for a natural crack, much more complicated distribution of conductivity may happen in an element. Even for the two-edge model, different combinations of the edge curves also may lead to a complex distribution in an element containing part of the crack edges. Therefore, modifications are necessary in order that the analysis code for a cavity crack can be extended to the problem of distributed conductivity. In this section, we derive basic formulae for the fast simulation of the signals coming from the two models separately with the emphasis placed on the difference with the procedure for a cavity crack.

2.4.1 Formulation for the conductivity model

If we assume the conductivity changing smoothly at the crack region besides the crack edge, the formulae for a cavity crack can be extended without much modifications. As the difference between a cavity crack and a crack with non-vanishing conductivity occurs only

in the distribution of conductivity, we can treat a crack of the conductivity model by taking this difference into account in the coefficient matrix $[K]$ of Eq.(2.9), the only term possibly affected by the distribution of $\sigma_0 - \sigma(\mathbf{r})$. Practically, the conductivity in the formulae for each sub-matrix of $[K]$ should be considered as a variable[2]. Taking sub-matrix $[N_2]$ as an example, it becomes,

$$[N_2] = \int_{\Omega_c} (\sigma_0 - \sigma(\mathbf{r}))[N][N]^T dv, \tag{2.24}$$

where $[N]$ is the matrix of shape function of FEM by which the potentials are discretized. The integral in Eq.(2.24) can be simply calculated with use of the Gauss integration by treating the conductivity as a variable at each Gauss point like,

$$[N_2] = \sum_l \sum_m \sum_n w_l w_m w_n (\sigma_0 - \sigma(\mathbf{r}_{lmn}))[N(\mathbf{r}_{lmn})][N(\mathbf{r}_{lmn})]^T, \tag{2.25}$$

where, w_l, w_m, w_n are the weight coefficients, and $\mathbf{r}_{lmn}$ is the coordinate vector corresponding to the $lnm - th$ Gauss point.

The derivatives with respect to the coefficients of the wavelet expansion can be derived with use of the equation given in Ref.[9],[10] by replacing the base function as the scaling function of Daubechies' wavelet. Considering the compact support property of the wavelet function, the integral becomes,

$$\frac{\partial Z_m}{\partial a_{n,k_1k_2}} = \int_{-h}^{h} \{ \int_{S_{k_1k_2}} (\sigma_0 - \sigma(r))|\mathbf{E}_m(x,y,z)|^2 \phi_{k_1}(x)\phi_{k_2}(z) dxdz \} dy, \tag{2.26}$$

where, $S_{k_1k_2}$ is the joint area of the support of the two dimensional wavelet $\Phi_{n,k_1k_2}(x,z) = \phi_{n,k_1}(x)\phi_{n,k_2}(z)$ and the selected zone of crack. The ranges of the subscripts k_1 and k_2 are the same as those given in Eq.(2) and (3). The Eq.(2.26) can also be calculated by applying the Gauss integration to each subregion selected according to the resolution level of the wavelet bases.

2.4.2 Formulation for the two-edge model

The two-edge model is a specific case of the conductivity model. Therefore, the calculation of the pick-up signals can be performed with a similar way like those just stated. However, as the description of the crack has been modified, a new formulation is necessary for predicting the gradients. In addition, it is more efficient if we take the features of the two-edge model into account during the forward analysis as it possibly be separated into two problems of a cavity crack. This property can simplify the implement procedure of the derived formulae as the code for a cavity crack is applicable directly. Follows is the basic formulation corresponding to this idealized model of a natural crack.

For the forward analysis of a crack of the two-edge model, it is easy to find that the coefficient matrix $[H]$ in Eq.(2.9) has no difference with that for a cavity crack or a crack of the conductivity model if the analysis region was selected the same. At the same time, in spite of the effects of crack shapes on the coefficient matrix $[K]$, this matrix can be derived

from the coefficient matrices of two cavity cracks defined respectively by the two edge curves. Similarly, the gradients with respect to the crack parameters of the two-edge model can also be derived from the gradients corresponding to the two cavity cracks respectively.

Keeping in mind the property of linear dependence of the coefficient matrix $[K]$ on the conductivity, we can find that each element coefficient matrix contained in $[K]$ can be expressed as the following equation,

$$[K]_e = \frac{\sigma_1}{\sigma_0}[K_1]_e + \frac{(\sigma_0 - \sigma_1)}{\sigma_0}[K_2]_e = \alpha_1[K_1]_e + (1-\alpha_1)[K_2]_e, \tag{2.27}$$

where, $[K_1]_e$ is the element coefficient matrix for the cavity crack surrounded by the inner edge, $[K_2]_e$ is of that defined by the outer edge, and $\alpha_1 \equiv \sigma_1/\sigma_0$.

To calculate the gradient with respect to crack parameters of the two-edge model, we can apply the formulae for a cavity crack [Eq.(2.20),(2.21] to each discrete point at the two edge curves, with the electric-field adopted as those calculated using the coefficient matrix given in Eq.(2.27). Denoting the gradient for the crack surrounded by the inner edge as $\partial\bar{Z}_1/\partial b_{1,i}$ and those defined by the outer edge as $\partial\bar{Z}_2/\partial b_{2,i}$, they can be obtained from the following equations in addition with a linear coordinate transformation[2],

$$\begin{aligned}\frac{\partial\bar{Z}_m}{\partial x_{p_i}} &= -\sigma_0\int_{-h/2}^{h/2}\int_{\Gamma_i}|\mathbf{E}_{tm}|^2\frac{(t_{i+1}-t)}{(t_{i+1}-t_i)}\frac{(z_{p_{i+1}}-z_{p_i})}{(t_{i+1}-t_i)}dtdy \\ &+ \int_{-h/2}^{h/2}\int_{\Gamma_{i-1}}|\mathbf{E}_{tm}|^2\frac{(t-t_{i-1})}{(t_i-t_{i-1})}\frac{(z_{p_i}-z_{p_{i-1}})}{(t_i-t_{i-1})}dtdy, \\ &\qquad i = 1, 2, ...n_c\end{aligned} \tag{2.28}$$

$$\begin{aligned}\frac{\partial\bar{Z}_m}{\partial z_{p_i}} &= -\sigma_0\int_{-h/2}^{h/2}\int_{\Gamma_i}|\mathbf{E}_{tm}|^2\frac{(t_{i+1}-t)}{(t_{i+1}-t_i)}\frac{(x_{p_i}-x_{p_{i+1}})}{(t_{i+1}-t_i)}dtdy \\ &+ \int_{-h/2}^{h/2}\int_{\Gamma_{i-1}}|\mathbf{E}_{tm}|^2\frac{(t-t_{i-1})}{(t_i-t_{i-1})}\frac{(x_{p_{i-1}}-x_{p_i})}{(t_i-t_{i-1})}dtdy, \\ &\qquad i = 2, 3, ..., n_c - 1\end{aligned} \tag{2.29}$$

the actual gradients for a crack of the two-edge model can be predicted by using the following equations, i.e., for points located at the edge of inner side,

$$\frac{\partial Z_m}{\partial b_{1,i}} = \frac{\sigma_1}{\sigma_0}\frac{\partial\bar{Z}_{1,m}}{\partial b_{1,i}} = \alpha_1\frac{\partial\bar{Z}_{1,m}}{\partial b_{1,i}}, \tag{2.30}$$

for those at the outer edge,

$$\frac{\partial Z_m}{\partial b_{2,i}} = \frac{\sigma_0-\sigma_1}{\sigma_0}\frac{\partial\bar{Z}_{2,m}}{\partial b_{2,i}} = (1-\alpha_1)\frac{\partial\bar{Z}_{2,m}}{\partial b_{2,i}}. \tag{2.31}$$

In these equations and those at follows, the subscript m denotes the number representing the order of sampling points of ECT data which is equal to the product of scanning steps and the number of applied frequency.

For α_1, the parameter of conductivity, one has,

$$\frac{\partial Z_m}{\partial \alpha_1} = \sigma_0\int_{-h/2}^{h/2}\left\{\int_{S_2}|\mathbf{E}_m|^2\Phi_{n,k_1k_2}(x,z)dxdz\right\}dy$$

$$- \sigma_0 \int_{-h/2}^{h/2} \left\{ \int_{S_1} |\mathbf{E}_m|^2 \Phi_{n,k_1k_2}(x,z) dx dz \right\} dy \tag{2.32}$$

or,

$$\frac{\partial Z_m}{\partial \alpha_1} = \frac{\partial \bar{Z}_{m,2}}{\partial \alpha_1} - \frac{\partial \bar{Z}_{m,1}}{\partial \alpha_1}. \tag{2.33}$$

In case of a crack like that illustrated in Fig.2.3, the expressions of the gradients with respect to the parameters described in the figure are as follows,

$$\frac{\partial Z_m}{\partial b_i} = \frac{\sigma_1}{\sigma_0} \frac{\partial \bar{Z}_{m,2}}{\partial b_{1,i}} = \alpha_1 \frac{\partial \bar{Z}_{m,2}}{\partial b_{1,i}}, \tag{2.34}$$

$$\frac{\partial Z_m}{\partial b_{i+3}} = \frac{\sigma_1}{\sigma_0} \frac{\partial \bar{Z}_{m,2}}{\partial b_{1,i}} + \frac{\sigma_0 - \sigma_1}{\sigma_0} \frac{\partial \bar{Z}_{m,1}}{\partial b_{2,i}} = \alpha_1 \frac{\partial \bar{Z}_{m,2}}{\partial b_{1,i}} + (1-\alpha_1) \frac{\partial \bar{Z}_{m,1}}{\partial b_{2,i}}, \tag{2.35}$$

$$\frac{\partial Z_m}{\partial \alpha_1} = \frac{\partial \bar{Z}_{m,2}}{\partial \alpha_1} - \frac{\partial \bar{Z}_{m,1}}{\partial \alpha_1}, \tag{2.36}$$

$$i = 1, 2, 3.$$

On the basis of Eqs.(2.34), (2.35), (2.36), we developed a code for the rapid calculation of signals and their corresponding gradients for the idealized cracks. The validity of this approach has been verified by comparing its numerical results with those of the conventional FEM-BEM hybrid code which has been verified accurate for ECT problems through a long term of validations and applications[11],[12]. Fig.2.4 depicts a comparison of the impedance signals calculated by using the FEM-BEM hybrid code and those of the present rapid scheme. Good agreement is obtained within a much shorter CPU time which, in turn, verified the validity and efficiency of our new scheme. The small difference comes from the adopted different numbers of mesh layers which is difficult to be a large number for the FEM-BEM code because of the limited computer resources.

2.5. Inverse procedure

According to features of the pick-up signals, it is not difficult to determine an area where a natural crack possibly exist in the conductor to be inspected. This region then can be applied for the establishment of the data-bases needed by the fast forward solver. On the basis of these pre-calculated data, the pick-up signals and the corresponding gradients can be predicted utilizing the formulae proposed in the last section for a given crack. Therefore, in order to solve the crack parameters from an inverse problem, we only need to introduce an algorithm keeping in mind the fact that the pick-up signals and gradients have been known prior to each iteration step.

As both of the pick-up signals and gradients can be efficiently predicted by using the fast forward solver, here we choose the conjugate gradient method for the reconstruction of crack parameters as what has been done in the case for a cavity crack[13],[14],[15]. The crack parameters, on the other hand, are chosen as the coefficients of wevelet expansion for the

conductivity model and the coordinates of discrete points at crack edge in addition with the unknown conductivity for the two-edge model.

2.5.1 A crack of the conductivity model

The objective of the optimization of crack parameters is to minimize the difference between the observed and predicted pick-up signals. Usually, the square residual of the observed and the simulated signals subjected to some constraint conditions is adopted as the object function. For a crack of the conductivity model, the conductivity at the boundary of the selected crack region is equal to the value of the base material. This condition can be selected as constraints upon the square residual, i.e. we impose the coefficients of the discrete expansion to satisfy the boundary condition at points located at the crack edge,

$$f_i = \sum_{k_1=-2N+2}^{-1} \sum_{k_2=-2N+2}^{2^n-1} a_{n,k_1k_2}\phi_{n,k_1}(-1)\phi_{n,k_2}(z_i) = 0, \tag{2.37}$$

$$g_i = \sum_{k_1=-2N+2}^{-1} \sum_{k_2=-2N+2}^{2^n-1} a_{n,k_1k_2}\phi_{n,k_1}(1)\phi_{n,k_2}(z_i) = 0, \tag{2.38}$$

$$h_i = \sum_{k_1=-2N+2}^{2^n-1} \sum_{k_2=-2N+2}^{-1} a_{n,k_1k_2}\phi_{n,k_1}(x_i)\phi_{n,k_2}(1) = 0, \tag{2.39}$$

$$i = 1, 2, ...2^n + 2N - 2,$$

where, the selected zone of a crack has been transformed into a square region with side length equal 2 and with its center located at the coordinate original point. The points used in the above equations, say, $(-1, z_i), (1, z_i), (x_i, 1)$, are equally spaced at the edges of the square besides that in the side of crack opening.

These equations are very strong constraint conditions for the procedure determining the coefficients of conductivity distribution. This may worsen the condition number of inverse problem and lead to failure in convergence. A way to avoid this difficulty is to apply the method of moment, i.e. instead of Eqs.(2.37), (2.38), (2.39), we impose them to be satisfied from the point of view of a weighted average. By multiplying wavelet bases $\phi_{n,k_1}(x)$ (or $\phi_{n,k_2}(z)$) to the two sides of Eqs.(2.37), (2.38), (2.39) and taking integration, the following conditions can be obtained as a weaken form of the constraint conditions,

$$f_{k_2} = \sum_{k_1=-2N+2}^{-1} a_{n,k_1k_2}\phi_{n,k_2}(0) = 0, \tag{2.40}$$

$$g_{k_2} = \sum_{k_1=-2N+2}^{-1} a_{n,k_1k_2}\phi_{n,k_2}(1) = 0, \tag{2.41}$$

$$h_{k_1} = \sum_{k_2=-2N+2}^{-1} a_{n,k_1k_2}\phi_{n,k_2}(0) = 0, \tag{2.42}$$

$$k_1, k_2 = 2 - 2N, ...2^n - 1,$$

where, the orthogonal property of wavelet bases has been applied.

The Eqs.(2.40), (2.41), (2.42) can be taking into account in the object function by using the Lagrange multiplier method as,

$$\varepsilon = \sum_m w_m \left|[Z_m(\mathbf{b}) - Z_m^{obs}]\right|^2 + \sum_i |(\alpha_i f_i + \beta_i g_i + \lambda_i h_i)| \tag{2.43}$$

where, $Z_m(\mathbf{b})$ is the impedance signals at m-th sampling point arisen from a crack with a parameter vector $\mathbf{b}$ predicted at the previous step. Z_m^{obs} is the observed impedance signals from ECT inspection. Coefficients $\alpha_i, \beta_i, \lambda_i$ are the Lagrange multipliers that can be treated with a similar way like that for the crack parameters.

Actually, the reconstructed conductivity at edges of the selected region has no significant difference if the selected region is enough large comparing with the true crack. In this case, the constraint conditions do not affect the optimization procedure notably. Therefore, it is reasonable to neglect the effect of these extra terms in the object function if we choose a larger analysis region.

The coefficient of conductivity can be determined with an iteration algorithm of the conjugate gradient method by minimizing the object function (2.43) or that with the constraint conditions neglected. However, as we have to reconstruct all the coefficient at each iteration step, the analysis area at every step must be taken as the whole selected region. This obviously will result in a large computation burden even for a conductivity change localized in a small area.

2.5.2 Reconstruction of a crack of the two-edge model

For the reconstruction of a crack of the two-edge model, the algorithm of the conjugate gradient method is also valid after some modifications. In this case, we take the object function as the residual square again and updating the crack parameters partly along the direction of gradient vector. In the follows, we give this inverse algorithm with an emphasis upon the difference with the scheme for a cavity crack[2].

As the first step of the inversion, we need to select an appropriate initial profile for the crack. This is not difficult as we can simply find a cavity crack who gives an impedance signal similar to the measured data by using the code developed for an EDM crack. This procedure is very fast as only discrete points at one edge curve need to be determined. Using the parameters of the selected cavity crack, the initial values of the two-edge model can be chosen by, (1) set the outer edge as the same as the edge of the cavity crack just decided, (2) set the inner crack as that determined by the outer edge and a given band width, and (3) set the initial value of the conductivity parameter as a value around 0.5.

Comparing with the case of a cavity crack, the most significant difference in the iteration procedure is that two types of crack parameter are necessary to be reconstructed, viz, the size of the crack and the conductivity. It is easy to find that, as the units of these two types of parameter are different, the gradient with respect to these parameters may be very different (even much different order). This will lead to a quite different convergent speed for these two types of parameter if a normal algorithm of conjugate gradient method

is applied directly. To overcome this difficulty, here we propose a scheme by improving the optimization algorithm. The basic ideas of this procedure is that, the updating direction and step size will be calculated separately for the parameters in different type by partly using the formulae of the conjugate gradient method.

For the parameters related to the crack size, i.e. the coordinate of the two-crack edges, corresponding to the modification direction of gradient $\{\partial\varepsilon/\partial b_i\}$, the formula for the step length a_1^n is,

$$a_1^n = P_1^n / Q_1^n \tag{2.44}$$

where,

$$P_1^n = Re\left\{\sum_m [Z_m^{n-1}(\mathbf{b}, \alpha_1) - Z_m^{obs}]^* \sum_i \frac{\partial Z_m^{n-1}}{\partial b_i}\frac{\partial \varepsilon^{n-1}}{\partial b_i}\right\} \tag{2.45}$$

$$Q_1^n = \sum_m \left|\sum_i \frac{\partial Z_m^{n-1}}{\partial b_i}\frac{\partial \varepsilon^{n-1}}{\partial b_i}\right|^2 \tag{2.46}$$

For step length related to the parameter of conductivity at the band region surrounding the crack, it becomes,

$$a_2^n = P_2^n / Q_2^n \tag{2.47}$$

where,

$$P_2^n = Re\left\{\sum_m [Z_m^{n-1}(\mathbf{b}, \alpha_1) - Z_m^{obs}]^* \frac{\partial Z_m^{n-1}}{\partial \alpha_1}\frac{\partial \varepsilon^{n-1}}{\partial \alpha_1}\right\} \tag{2.48}$$

$$Q_2^n = \sum_m \left|\frac{\partial Z_m^{n-1}}{\partial \alpha_1}\frac{\partial \varepsilon^{n-1}}{\partial \alpha_1}\right|^2 \tag{2.49}$$

Based on the formulae above, the iteration equation for updating the crack parameters can be written as,

$$\{\mathbf{b}^n, \alpha_1^n\}^T = \left\{\mathbf{b}^{n-1} + a_1^n\{\frac{\partial Z_m^{n-1}}{\partial b^{n-1}}\}, \alpha_1^{n-1} + a_2^n \frac{\partial Z_m^{n-1}}{\partial \alpha_1^{n-1}}\right\}^T . \tag{2.50}$$

2.6. Implementation and numerical results

On the basis of the formulae described in the previous sections, two codes have been developed respectively for the conductivity model and the two-edge model. In this part we present some typical reconstruction results of these two codes for validating the proposed method. The feasibility and efficiency of the method related to the two models are compared finally from the point of view of possible applications to the inspection of SG tubing.

We choose a self induction pancake coil of 100 turns as the probe for ECT inspection which was winded with an outer radius 1.6 mm, an inner radius 0.5 mm and a thickness 1 mm. The probe is arranged in parallel over the inner surface of tube with a lift-off equal to 1. mm. The excitation frequency is chosen as 400kHz which is a typical one in the practical inspection of SG tubing. The scanning is performed axially along the crack from -10 mm

to 10 mm and with the step length chosen as 0.5 mm. These 41 impedance data are used for the reconstruction of all the crack parameters. As a need of the fast forward solver, two data-bases are established with the possible crack region selected as a 10 mm × 1.27 mm × 0.2 mm cubic zone and subdivided into 20 × 8 × 1 cells.

2.6.1 Results for the two-edge model

To investigate the efficiency of the two-edge model, we have implemented the algorithm at first for the crack parameters described in Fig.2.4. For a crack with arbitrary shape, this code can be simply extended by changing the number of crack parameters. In order to validate the algorithm for different type of parameters, the size parameters of the crack are reconstructed in both the conditions of a known and an unknown conductivity parameter. The results show that, the modified scheme of the conjugate gradient method can give satisfactory reconstruction even for the case with different types of parameter.

Fig.2.6 depicts a comparison of the impedance signals arisen from a reconstructed crack and the simulated impedance which we used as the observed data. The true shape of the crack, as shown in Fig.2.7, is assumed to be an inner one with a maximum depth equal to 50% of the tube thickness. In this case, the conductivity parameter α_1 at the conducting band region was taken as a known value (=0.5). Excellent reconstruction results are obtained in this case though the convergence speed is not as fast as the case of a cavity crack. The results shown in Fig.2.6 and Fig.2.7 are obtained at the 300-th iteration. The CPU time used is about 3 hours on a personal computer(Gateway GP6-333).

Fig.2.8 and Fig.2.9 shows another reconstruction results for a crack with an unknown conductivity after 300 iterations. The reconstructed conductivity parameter is 0.102 for a true value of 0.1. In this case, we chose the initial conductivity as half of the base conductor and start the iteration from the initial crack size predicted by using the code for a cavity crack. The modified algorithm was adopted to update the two types of parameter respectively. Very good convergence result is found again for both the shape parameters and the conductivity. From the satisfactory reconstruction results given here, we come to a conclusion that the reconstruction of crack parameters of different types is possible.

Comparing with the reconstruction of a cavity crack, the iteration number of the present method is much larger for a similar accuracy (over 10 times). This decrement of convergence speed is considered caused by the greatly increased number of local minimum. In other word, the signals from different set of parameters may be very similar although the parameter is much different. This leads to that the step size of updating becomes a small value. From this point of view, more effort is necessary in the near future to accelerate the convergence in order this method possibly to be applied more efficiently in the practical data processing.

2.6.2 Results for the conductivity model

In Fig.2.10 and Fig.2.11, the reconstructed results using the conductivity model are depicted. The iteration number and CPU time corresponding to these results are respectively 100 and over 16 hours on the same personal computer. The significantly increased computational work is caused by the large number of unknowns, as field at the whole selected crack region must be solved at each iteration. In addition, the large number of crack parameters also enlarges the computation burden for estimating the gradient vector. In these results, the resolution level was used as 4 and the index of the Daubechies' wavelet was chosen as 5. The true profiles of the crack is the same as that described in the Fig.2.9. One can find the shape of the crack approximately from the estimated distribution of conductivity given in Fig.2.10. However, the jump of conductivity at the crack edge has not been recovered well. This means that it is not very efficient of the conductivity model to reconstruct a crack with an abrupt conductivity jump without much more iterations. This is because that, even for an impedance signal very similar to that arisen from the true crack, the corresponding conductivity may show much bigger error comparing with the true distribution.

Comparing with the results of the two-edge model, reconstructing conductivity directly is obviously not efficient and accurate especially for a crack with a conductivity jump. Therefore, for the reconstruction of a SCC in SG tubing, using the two-edge model is reasonable.

2.6.3 Effect of random noise

To consider the robustness of the present inverse scheme, the reconstruction is undertaken with observed data added by artificial noise in this part. By adjusting the maximum value of the noise component, we find that the new inverse scheme can give acceptable estimation of crack shapes even for signals with 20% noise.

In calculation, the observed ECT data Z^{sobs} was generated with the following formula which combines the simulated ECT data Z^{sim} with a white noise,

$$Z_m^{sobs} = Z_m^{sim} + \alpha |Z_{max}^{sim}| \xi_m, \tag{2.51}$$

where, α is the proportion of the noise in the whole signal, ξ_m is random values within $[-1.0, 1.0]$ and is generated by a short computer code of the white noise, $|Z_{max}^{sim}|$ is the maximum value of the simulated ECT data.

In Fig.2.12 and Fig.2.13, the reconstructed crack shape and impedance signals are compared with the true ones. In this case, the true crack is selected the same as that utilized in Fig.2.8 and Fig.2.9 again. 5% white noise was added to the observed signals. It is easy to find that, although the reconstruction precision is not as high as the case without noise included, satisfactory crack parameters are obtained with a similar computational burden. The reconstructed value of the conductivity is 0.144 with the true value used as 0.1, the same as the case of Fig.2.8 and Fig.2.9. Fig.2.14 and Fig.2.15 depict the reconstructed crack shape and impedance signals in case of 10% noise. Satisfactory crack parameters are predicted again within a similar computational time.

2.7. Conclusions

In this paper, by proposing new models for a stress corrosion crack and extending the inverse scheme of a cavity slit, the reconstruction of an idealized natural crack with non-vanishing conductivity was successfully realized at a personal computer. The simulation results depicted that the model with two edges and unknown constant conductivity is better than the conductivity model in efficiency and more suitable for the practical problems. By performing reconstruction with use of signals containing artificial noise, the new approach was demonstrated both robust and feasible for predicting profiles of the idealized crack model. More work is necessary for investigating the efficiency of the present method for a measured signal and for the problem with an unknown position of crack plane.

2.8. References

[1] Z.Chen, K.Miya, and M.Kurokawa, Rapid prediction of eddy current testing signals using $\mathbf{A} - \phi$ method and database, NDT&E international, Vol.32, No.1, 29-36, 1998.

[2] Z.Chen and K.Miya, ECT inversion using a knowledge based forward solver, J. Nondestr. Eval., Vol.17, No.3, 157-165, 1998.

[3] Z.Chen, W.Cheng and K.Miya, Shape reconstruction of natural cracks using a fast forward solver, in Proc. of 2-nd Japanese-French Joint Seminar on Eddy Current NDT, 104-111, 1997.

[4] Z.Badics et al., Rapid flaw reconstruction scheme for 3-d inverse problems in eddy current NDE, in Stud. Appl. Electromagn. Mech., Vol.12, 303-309, eds. T.Takagi et al., IOS press, 1996.

[5] H.A.Sabbagh and L.D.Sabbagh, Inverse problems in electro-magnetic non-destructive evaluation, Int. J. of Appl. Electromagn. in Mater. V.3, 253-261, 1993.

[6] Daubechies, Orthonormal bases of compactly supported wavelet, Commun. Pure Appl. Math., 41, 909-996, 1988.

[7] G.Mallat, A theory for Multiresolution Signal decomposition: the wavelet representation, Commun. Pure Appl. Math., 41, 674-693, 1988.

[8] Z.Chen, Y.Yoshida and K.Miya, Analysis of relations between the defect shapes and the wavelet coefficients of ECT data, in Studi. Appl. Electromagn. Mech., Vol.8, eds. R.Collins and et al., IOS press, 295-302, 1995.

[9] S.Norton and J.Bowler, Theory of ECT inversion, J. Appl. Phys. Vol.73, No.2, 501-512, 1993.

[10] J.R.Bowler, Eddy current interaction with an idea crack, I. the forward problem, J. Appl. Phys. Vol.75, No.12, 8128-8137, 1994.

[11] M.Kurokawa, K.Suguyama and K.Miya, An inverse analysis with the current vector potential $\mathbf{T}$, in Simulation and Design of Applied Electromagnetic Systems, Ed., T.Honma,

Elsevier, 197-200, 1994.

[12] T.Takagi, et al, Benchmark models of eddy current testing for steam generator tube: experiment and numerical analysis, Int. J. Appl. Electromagn. in Materials, Vol.4, 149-162, 1994.

[13] L.Udpa and S.S.Udpa, eddy current defect characterization using neural networks, Mater. Eval. Vol.48, No.1, 50-54, 1990.

[14] R.Zorgati and et al, eddy current testing of analyses in conductive materials, II. Quantitative imagine via deterministic and stochastic inversion technique, IEEE Tran. Magn., Vol.28, No.3, 1850-1862, 1992.

[15] J.Pavo and K. Miya, Reconstruction of crack shape by optimization using eddy current field measurement, IEEE Trans. on Mag., Vol.30, No.5, 3470-3410, 1994.

[16] J.A.Tegopoulos and E.E.Kriezis, Eddy currents in linear conducting media. Elsevier Science Publisher, 1985.

[17] M.Gramz, and et al., A crack element concept for a FEM analysis of eddy current distribution in a long cylinderical bar with a crack, in Nondestructive Testing (Proceedings of the 12th world conference), Opsit, p1035, 1989.

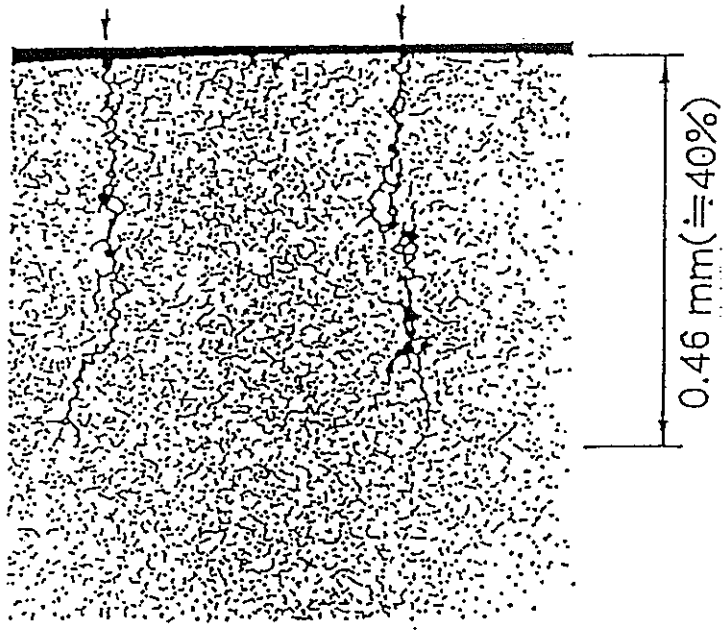

Fig.2.1 A viewgraph of typical SCC cracks in a SG tube

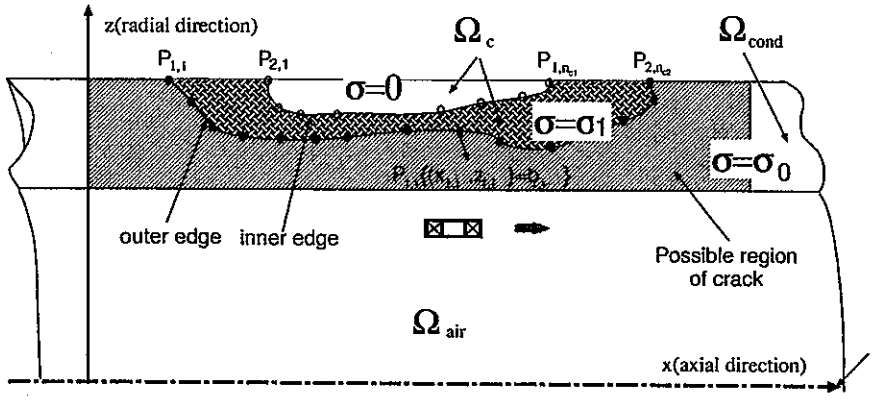

Fig.2.2 The two-edge model for a crack with touch

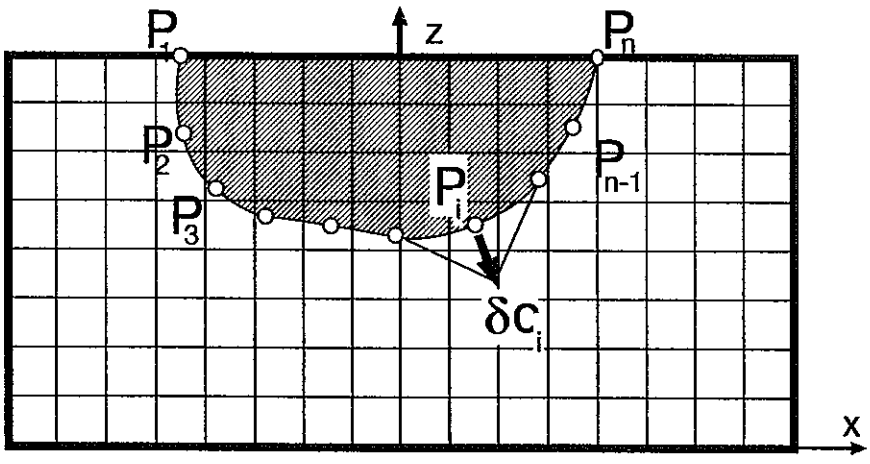

Fig.2.3 Discret parameters of an EDM crack

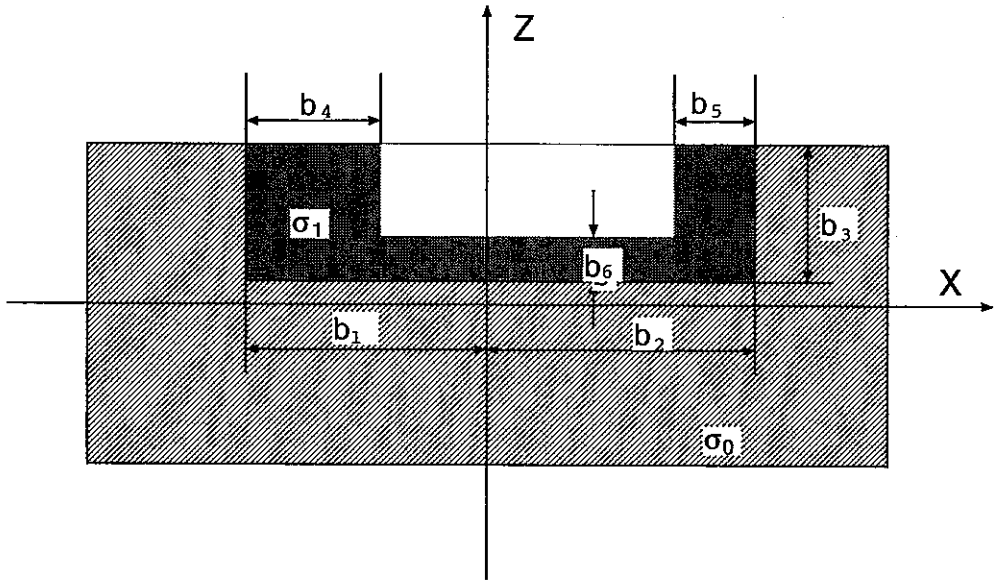

Fig.2.4 Crack parameters of two-edge model in case of a rectangular crack

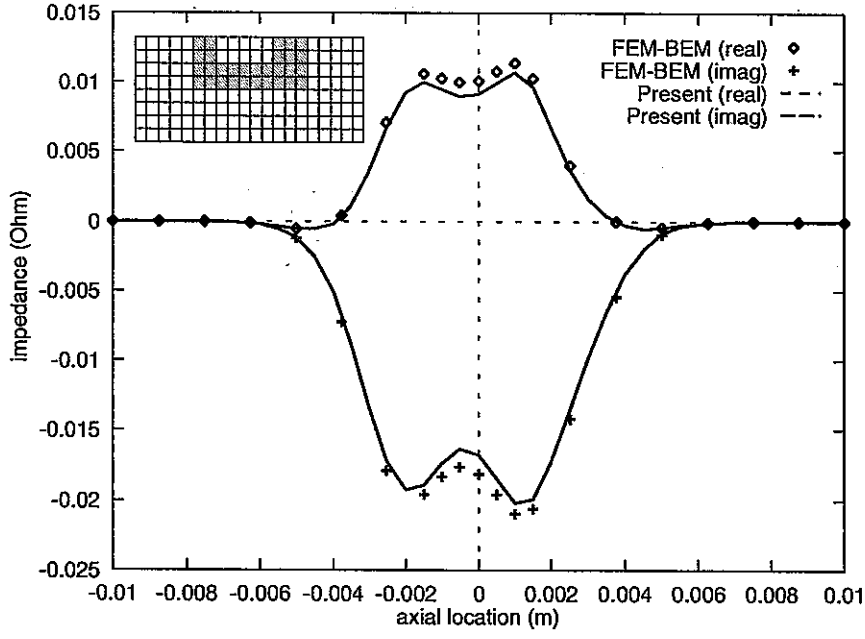

Fig.2.5 Comparison of simulated impedance signals by the FEM-BEM code and by the present method

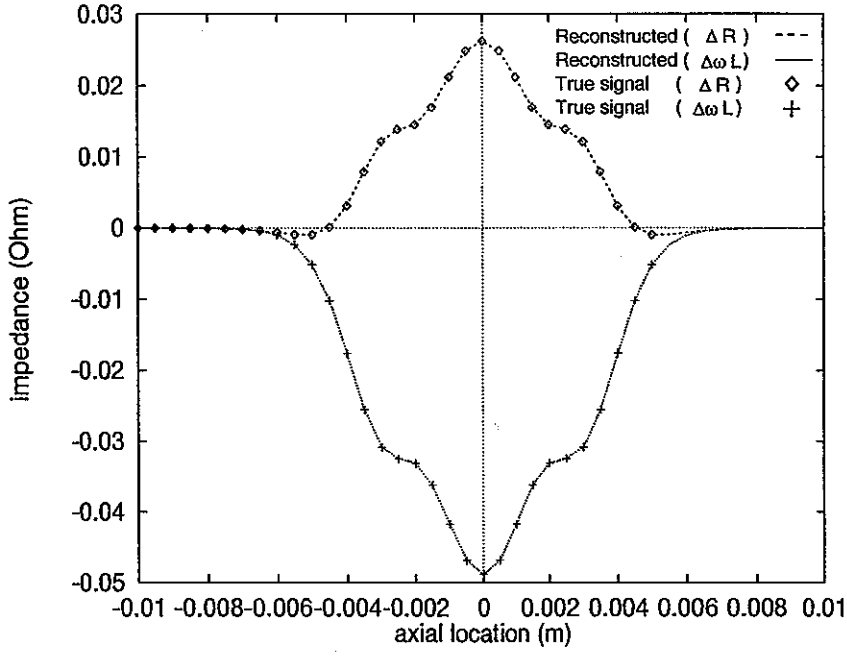

Fig.2.6 Impedance signals due to the reconstructed crack (known conductivity of the conducting band region)

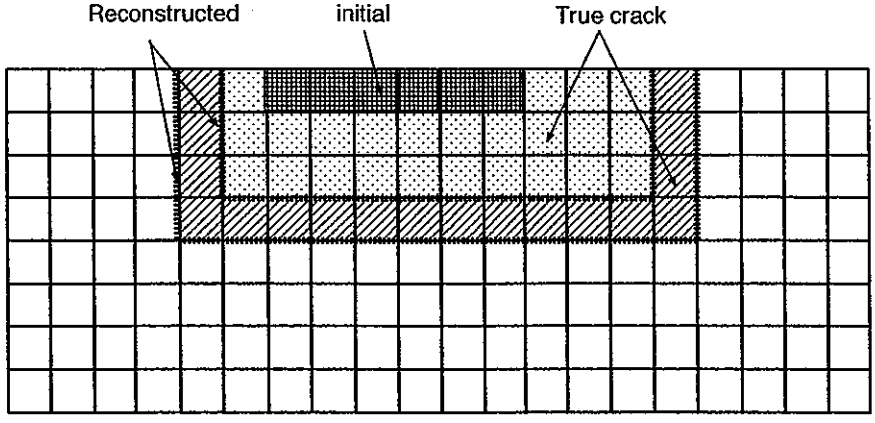

Fig.2.7 Reconstructed crack shape in case of known conductivity

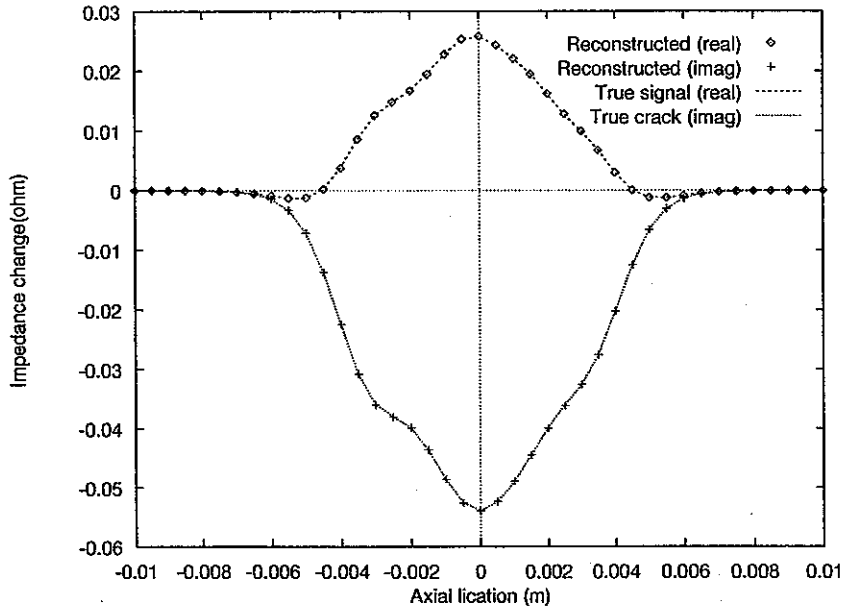

Fig.2.8 Impedance signals arisen from the reconstructed crack (with reconstructed conductivity for the conducting band region)

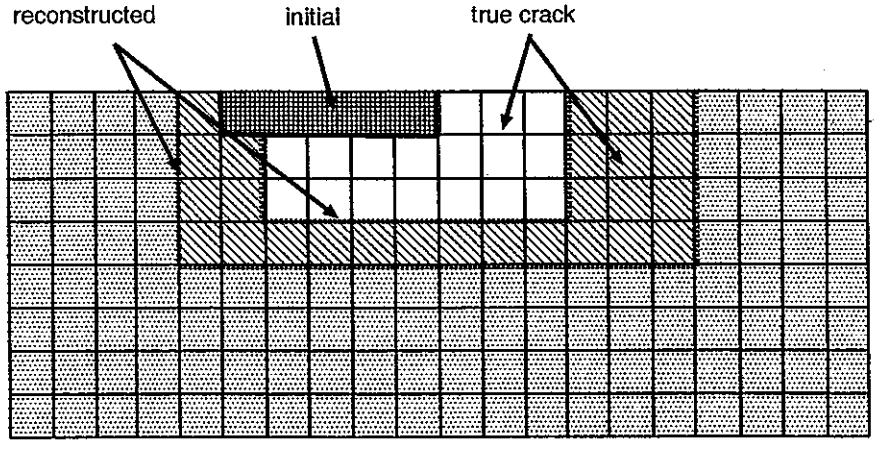

Fig.2.9 Reconstructed crack shape in case of unknown conductivity

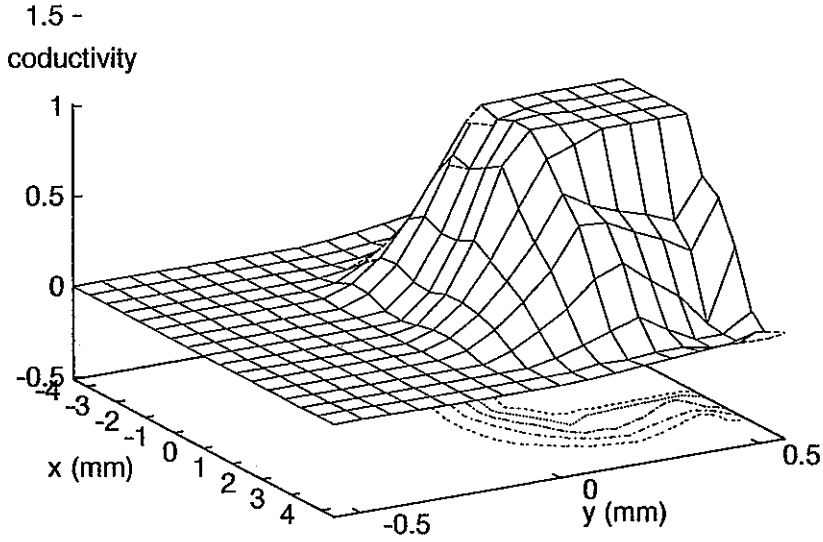

Fig.2.10 Reconstructed distribution of conductivity

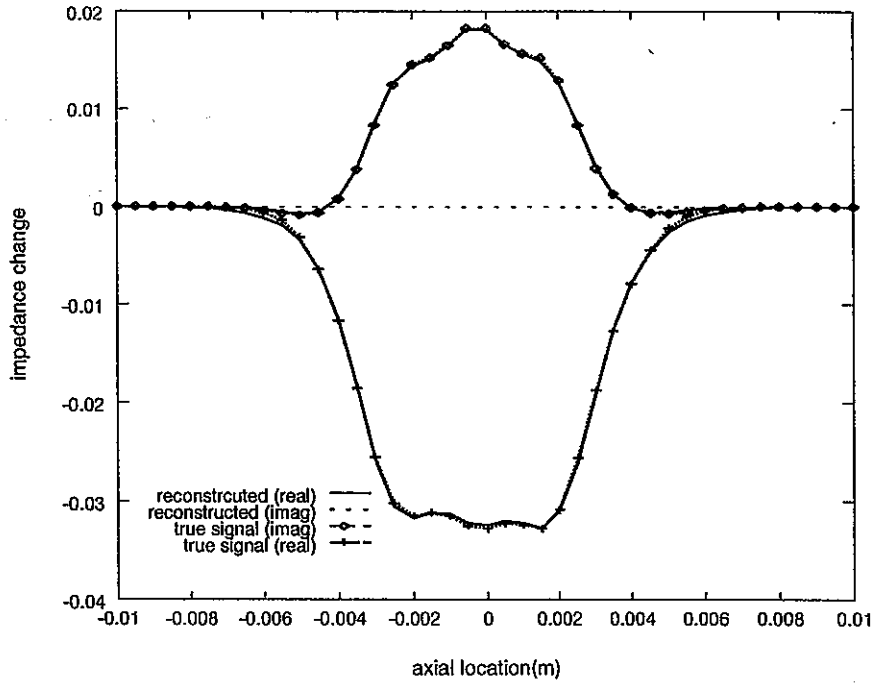

Fig.2.11 Comparison of impedance signals

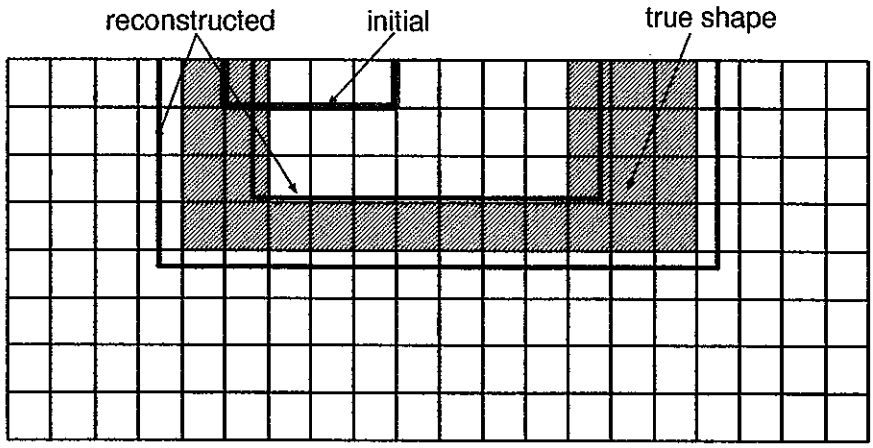

Fig.2.12 Comparison of the reconstructed crack shape with the true one (5% noise)

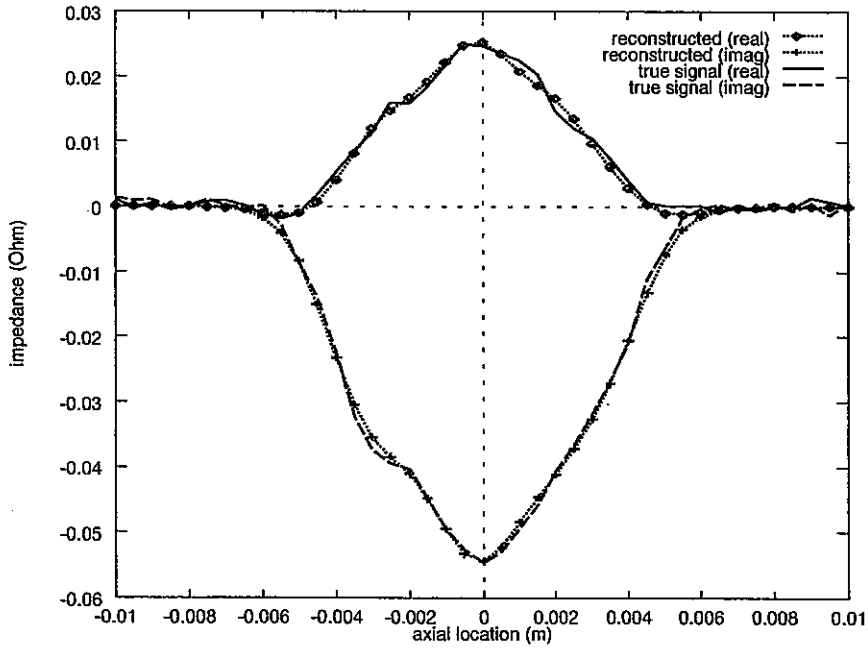

Fig.2.13 Comparison of impedance signals (5% noise)

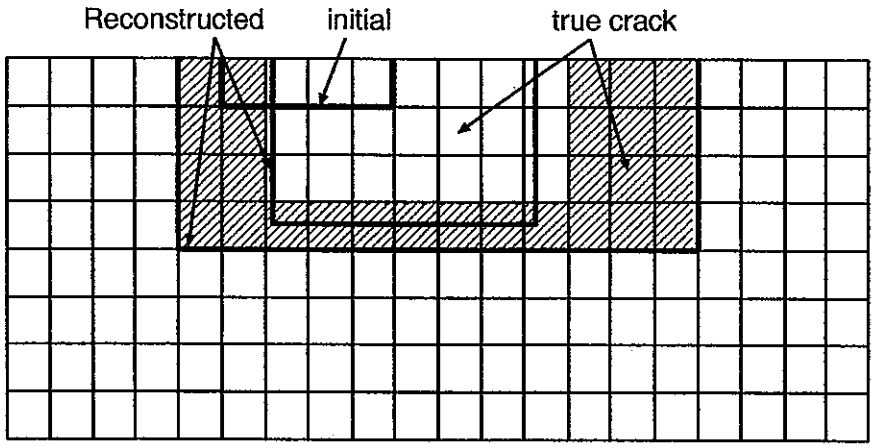

Fig.2.14 Comparison of the reconstructed crack shape with the true one (10% noise)

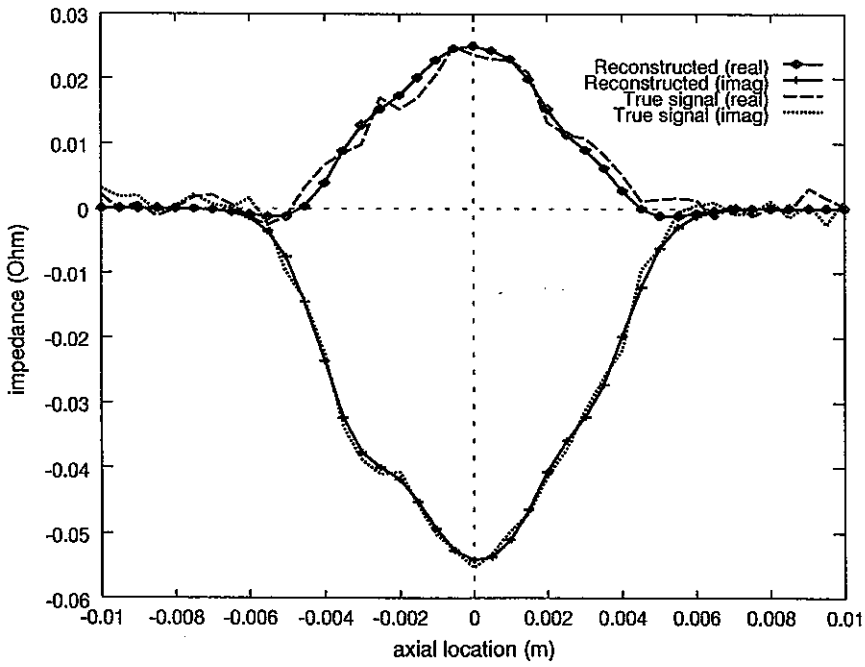

Fig.2.15 Comparison of impedance signals (10% noise)

Chapter 3

Experimental Study on the Correlation of Natural Magnetization and Mechanical Damages

Chapter 3

Experimental Study on the Correlation of Natural Magnetization and Mechanical Damages

3.1. Introduction

Recently, it was found that a magnetization occurs in the vicinity of a fatigue crack even in an environment without any external magnetic field (excepting the field of the earth) for the austenitic stainless steel of SUS304 type and some other normal carbon steels[1],[2]. The reason of such a phenomenon is considered as an effect of the magnetic property alternating that may arise from the mechanical damage and may result in an leakage of magnetic flux without applying external exciting field (hereafter, we call it a natural magnetic field)[3],[4]. This phenomenon shows a possibility to identify the mechanical damages by detecting the natural magnetic leakage flux. An obvious merit of such method is that the noise arisen from the surrounded structural component will not appear as there is no need to magnetize the material. A quantitative evaluation of damage is also possible if the correlation of the magnetizations and the local damage state is clarified.

In view of the background stated above, the correlation of mechanical damages and the corresponding natural magnetization is investigated in this work by detecting the leakage flux density nearby the surface of a test-piece in which mechanical damages are introduced by using a tension or a fatigue testing. An advanced film type flux-gate (FG) sensor[5], which is efficient for a weak static field, is applied in the experimental system for measuring the natural magnetic field that is usually in a same order or even less than the magnetic field of the earth. The natural magnetic fields are measured both during the mechanical testing (in-situ) and after unloading (off-situ). In practical, the experiment is performed in a procedure as follows: at first, the phenomenon of the natural magnetization is demonstrated

for SUS304 stainless steel by using standard test-piece and tensile testing. Then, the magnetic flux leakages were measured during and after the tensile testing for the same kind of test-piece under cyclic tensile loading in order to investigate the correlation of the natural magnetization and damages of plastic deformation. To evaluate the possibility of the damage status inspection for a key structure component in practical environment, signals of the magnetic leakage flux are measured during the fatigue testing. In this case, the distribution of the leakage magnetic field is measured at selected loading step numbers in an off-situ state for studying the evolution of damages at different fatigue stage.

On the other hand, though the flux leakage method is considered efficient for the ferromagnetic material, there is still no report for its application to the nonmagnetic/paramagnetic materials [3]. To clarify this question, the magnetic properties such as the residual magnetic field of a damaged material need to be known. As such measurement can be performed with the same experimental setup by just adding a magnetizing procedure (for instance, using a permanent magnet), this is also chosen as a testing subject of present experiment.

3.2. Experimental Issues

3.2.1 Test material and test-pieces

Aiming at application of the new flux leakage method to the NDE of structural components of new generation nuclear power plants, e.g. a plant of Fast Breeder nuclear Reactor (FBR) or that of the thermal fusion reactor (for instance, ITER), the stainless steel of SUS304 type is chosen as the target material to be inspected in this study. In order to perform zero-tension fatigue testing, a standard button type CCT test-piece[6] is selected considering the condition of our material testing system. 24 test pieces are fabricated from a raw material plate with the test-piece axis in parallel with the rolling direction. The present material is being used in the experimental FBR plant MONJU for taking advantage of its high performance in a high temperature environment. The chemical composition the material and the shape of the test piece is shown in table 3.1 and Fig.3.1 respectively. The gauge region is the central part of the test piece that is in a plate geometry and sized 40 mm×20 mm×5 mm. For several test-pieces, through central notches (3 mm × 0.3 mm slit or hole with 0.3 mm diameter) are fabricated by using the EDM technique for guarding the position of crack initiation. The location of the central artificial crack is illustrated in the Fig.3.1 by taking a slit as example. Concerning the compress loading in the fatigue testing at both room temperature and 650°C, the thickness of the test-piece is selected as 5 mm, i.e. a relative short and thick geometry is chosen for preventing buckling.

Table 3.1 Composition of the SUS304 A3 material (wt%)

C	Si	Mn	P	S	Ni	Cr
0.05	0.55	0.82	0.021	0.003	8.78	18.38

To measure the distribution of the macro-strain that is necessary for investigating the damage-magnetization relation, 2 sets of grating lines in a pitch of 0.08 mm have been etched to a 30 mm × 20 mm region on one of the planar surface of the test-piece for producing fringe pattern that is necessary in the moire method for the strain calculation[7],[8]. The grating lines are etched only with a 3 μm depth, which allows the strain measurement being performed without affecting the distributions of the strain and the magnetization. A glass grating mask is also made with use of the same grating pattern used for the test-piece surface. A fringe pattern will appear once this standard grating mask be overlaid on the surface of a deformed test-piece.

3.2.2 Measuring Method and Experimental Set-ups

a). Measurement of the magnetic field

To measure the magnetic leakage flux density induced by the mechanical damages, a sensor valid for small and static field is necessary. The Hall effect sensor is not feasible in this case as it can not work even in the measurement of the magnetic field of the earth. A SQUID (superconductor quantum interference device) is a very sensitive equipment for the weak magnetic field. Unfortunately, the necessity for a magnetic field shielding and the low space resolution protect this device from to be applied to the present subject. On the other hand, a conventional flux-gate sensor that has a sensitivity between the sensors mentioned above also has a drawback of low space resolution.

Recently, a new kind of FG sensor has been developed by the Shimatsu Corporation based on the photolithography technique. The film sensor is in a square shape with a side length about 1.0mm. The sensitivity of this sensor is about 0.0001Gs that can answer the needs of present application. The principle of the FG sensor can be described simply as follows:

As shown in Fig.3.2, the sensor consists of a core, an exciting coil, and 2 pick-up coils. The pick-up coils are connected in a differential way that makes the output signal becomes zero if no any external field presented. Once the sensor is set into a magnetic field, the balance of the two pickup coils will be disturbed, viz., one of it will change to $V + \Delta V$ and the other becomes $V - \Delta V$ where the ΔV is proportion to the magnetic field component shown in the Fig.3.2. Consequently, a signal of $2\delta V$ will be read that depends on the intensity of the external magnetic field linearly if the frequency is not too large.

From the principle described above, one may worry about the effect of the exciting field of the sensor on the magnetic field of the test-piece as a residual field possibly to be caused in a magnetic object when an exciting current moves over it. Fortunately, considering the fact that the excitation magnetic field is small and mainly concentrated in the ferrite core of the sensor, the effect from its leakage can be neglected for the problem we are dealing with. This fact is demonstrated when we perform a scanning near a surface of a demagnetized test-piece in which a slit exists. In fact, there is no significant perturbation detected near the slit. Therefore, omitting the effect of the exiting field is reasonable.

b). Measurement of the macro-strain distribution

As well known, the optical method is effective for the measurement of the strain distribution though it may give a lower precision than the method using a strain gauge. Considering the objective of the present experiment, say, investigating the homogeneity of the strain distribution during a simple tensile testing for the test-piece stated above, a method using moire fringe pattern is chosen.

The principle of the moire method is simple. At first, 2 sets of fine grating lines are printed on the surface of the test piece before deformation and the same grating lines are also printed on a standard glass mask. A fringe pattern will appear when the standard grating mask is overlaid on the deformed test-piece and the strain can be calculated by using the following formula,

$$\varepsilon_x = \frac{1}{f_x}\frac{\partial N_x}{\partial x}, \quad \varepsilon_y = \frac{1}{f_y}\frac{\partial N_y}{\partial y} \tag{3.1, 3.2}$$

$$\gamma_{xy} = \frac{1}{f_x}\frac{\partial N_y}{\partial x} + \frac{1}{f_y}\frac{\partial N_x}{\partial y} \tag{3.3}$$

where, $f_x = M_x/L_x$(lines/m) with M_x the total number of the grating lines in the x direction, L_x the length of the grating region in the x direction and the same for the y subscript case. The sensitivity of this method depends on the pitch Δ of the printed grating lines as the minimum strain detectable is $1/M$. Though the numbers of the fringe lines N_x, N_y are integer values, it can be treat as real variables by using a proper interpolation method.

For practical testing, the fringe patterns are caught after unloading the test piece unlike the situation shown in the schematic diagrams of Fig.3.3 concerning the difficulty of the in-situ measurement. The image of fringe patterns is converted into digital data through a CCD camera of 500,000 pixels and a high speed image board, and the strain distribution is calculated with a data processing code based on the formulae above on a personal computer. The setup of the moire method system is shown in the Fig.3.4 where the test-piece and glass mask (standard grating) is set on a specially designed instrument which can ensure the relative position and orientation of the glass mask and the test-piece which is important for enhancing the measuring accuracy.

c). In-situ measuring system of magnetic field

Fig.3.3 shows a flow-chart of the in-situ measuring system. 6 film type flux-gate sensors are set to the measuring point by using a specially designed instrument, which fixed at the topside of the test-piece as shown in Fig.3.5 to detect the magnetic field change during the tensile and fatigue testing (in-situ). A Shimatsu material testing machine (No AF-40) is applied as the mechanical loading system. The load limit of the machine is 5 ton and the maximum stroke is 50 mm. The sensors are fixed to the upper side of the test piece that does not move during both the tension and fatigue testing. The location of the sensors related to the test piece is shown in the Fig.3.6 and the lift-off of the sensors is taken as about 0.5 mm by adjusting the micrometer of the fixing instrument. The location of the sensors can

also controlled by using another 2 micrometers, in other word, the fixing instrument allows the sensors to be arranged to any space point (of-cause the moving area of the sensors is limited considering the range of the micrometer). Though the fixing instrument allow the sensors to be set for measuring both the component in-plane and that perpendicular to the plate surface, we choose the in-plan component to measure as it can be performed with a smaller lift-off. The output of the sensors are transferred to the computer with use of a special amplifier and a data acquiring system called Thermo-Wave. The post processing of the measured data is performed on the personal computer using commercial codes and that specially developed during this study.

d). Off-situ 2-d scanning system

The distribution of the leakage magnetic field is measured off-situ by scanning the unloaded test-piece on a x-y stager. The experimental setup is shown in Fig.3.7. After magnetic field measurement, the plastic deformation is measured by catching the moire fringe patterns.

The scanning area is selected as a square region with side lengths of 30 mm. Being the same with the case of the in-situ measurement, the lift-off is chosen as 0.5 mm for the scanning of the horizontal components. In the case of the vertical component measurement, the practical lift-off is larger than the distance between the sensor and the test-piece surface considering the size of the sensor itself. The scanning path is like that shown in Fig.3.6 but with the pitch in the x direction chosen as 1 mm. As the stager is not an automatic one, the movement of the stager needs to be driven by hand with a screw system. The pitch along the axial direction of the sensor is not a constant that can be determined from the speed of the scanning and the sampling system. The flux density at the data point with pitch of 1 mm both in the x and y directions are obtained by interpolating the measured data numerically.

e). System for magnetizing the test piece using a permanent magnet

To investigate the residual magnetization property of the test piece during a cyclic tensile testing, the test piece needs to be demagnetized/magnetized at each loading cycle. Magnetizing the test piece under the same conditions is necessary for realizing the research objective. Considering this requirement, the following magnetizing procedure is chosen that enable the the difference of the residual field due to the magnetizing system to be minimized.

At first, the test piece is set to the instrument that is designed for the position control in the strain measurement (the moire method). The instrument then was put on the table of the x-y stager with the center of the test piece coincided with that of the permanent magnet but with a different z coordinate. This operation is used to ensure the setting instrument to be set at the same location for each magnetizing step, which can be realized by adjusting the permanent magnet first to the center of the test-piece and then moving off perpendicularly to a position far away. Before each loading step, the test piece is demagnetized and arranged

to the same position of the instrument referring the counter of the equipped micrometers. Setting the instrument to x-y table at the position determined in the first step (according to the marks made on the table of the x-y stager), the relative position of the magnet and the test-piece can be ensured with a high accuracy. For magnetizing the test-piece, the permanent magnet is moved downward at first to a position touching with the test-piece surface, and then set to a $50\mu m$ lift-off. The permanent magnet is moved then in a path of (x, y) = (0 mm,0 mm) $\rightarrow$ (0 mm,-20 mm) $\rightarrow$ (0 mm,20 mm) $\rightarrow$ (0 mm,0 mm), and finally moved up vertically to a far position. Though the magnetization is not uniform for this magnetizing method, the residual field does not change a lot for different magnetizing step if virgin test-pieces are used.

In this work, a permanent magnet consisting of 3 cylinder magnets (length: 3 mm, diameter: 5 mm, $B_r \simeq 0.1$T) is employed. The axis of the magnet is set in parallel with the axis of the test-piece. The setup of the magnetizing system is shown in Fig.3.8.

3.2.3 Experimental Procedure

The number of the utilized test-pieces and their testing conditions are summarized in table 3.2. The test-pieces are demagnetized by using an electromagnetic demagnetizer (Hozan HC-21) before setting them to the material test machine. Strain control is applied for all the tensile and fatigue testings. In case of the tensile testing, the flux density at the central part of gauge region is in-situ detected while the distributions of the leakage magnetic field are measured on the x-y stager after unloading the test-piece. For the test-pieces of number NDT14 and NDT12, they were unloaded after each ε_{max} (see Table 3.2) was reached for magnetic field distribution measurement with the 2-d scanning. In case of the fatigue testing, the in-situ measuring of the magnetic field is performed with the sensors set at the same locations used in the tensile testing for all the loading cycles. However, the 2-d scanning for the distributions of magnetic field is performed only for the test-piece that was unloaded at given cyclic number. Once a crack initiated, the fatigue testing can be stopped automatically according to a threshold minimum loading value set beforehand.

The measurement of the 2-d distribution of the strains is only performed for the test-piece NDT14 and NDT13. The unloaded test-piece is set to the specially designed instrument, and the glass mask is overlaid. The moire fringe patterns were taken into the computer and the fringe line information was extracted by processing the obtained image data i.e. calculating the discrete values of the $N_x(x, y), N_y(x, y)$. The strain is calculated then by using a code based on the Eq.(3.1) and Eq.(3.2). This procedure is carried out for each loading step listed in the table 3.2 for NDT14. The results show that the strain measured by the push type strain sensor agrees well with that obtained by the moire method, which in turn shows that the local concentration of deformation is not significant for these two test-pieces and loading patterns.

Table 3.2 Measured test-pieces and their test conditions

No. of Test-Piece	Central Notch	Experimental Conditions
ndt2	no slit	ε_{max} = 3%, 6%, 9%, Loading speed 0.01%/sec
ndt21	slit	ε_{max} = 3%, Speed: 0.01%/sec
ndt14	no slit	0.2%, 0.5%, 1%, 2%, 3%, Speed: 0.01%/s
ndt12	no slit	0.2%, 0.5%, 1%, 2%, 3%, 6.0%, Speed: 0.01%/s
ndt21	slit	Range: ± 0.25%, Speed: 0.1%/sec, N=1, ~ 940
ndt20	slit	Range: ± 0.25%, Speed: 0.1%/sec, N=1, ~ 980
ndt14	no slit	Range: ± 0.25%, Speed: 0.1%/sec, N=1, ~ 4600
ndt13	slit	Range: ± 0.25%, Speed: 0.1%/sec, N=1, ~ 63000

3.3. Experimental Results

3.3.1 Results of the tensile testing

a). Measuring results of the flux density

Fig.3.9 shows an in-situ measuring result for test-piece NDT2 during a tensile testing from 0% to a maximum strain of 3%. The test conditions are listed in the table 3.2 where 3%, 6%, and 9% mean that the test-piece was unloaded after total strain 3%, 6%, 9% was reached respectively. The results shown in the figure is the case during the tension to 3%. From this result, it is clear that the magnetizations have occurred in the gauge region. As the test-piece was demagnetized before the tension and there is no external magnetic field changed during the testing, such a magnetization is obviously caused by the applied deformation or loading. On the other hand, though small magnetic fields have been detected at the elastic period, the magnetization increases much faster when plastic strains occurred, and saturate at last when the plastic deformation getting too large. In addition, the magnetization did not disappear after the loading was released. These results tell us that the magnetizations arise from the plastic damages but not from the effect of inverse magnetostriction. Fig.3.10 shows the in-situ measuring results for the NDT2 test-piece during tension from 2.8% (the residual strain of the first tensile testing) to 5.8%. It is clear that the change of the detected flux density is much smaller than that happened for the virgin material test-piece, or in other word, a saturation has happened in this case.

To investigate the property of the magnetization distribution, the 2-d distributions of the leakage flux density have been measured after unloading the test-piece. Fig.3.11 gives the distribution of the B_y component of the flux leakage at a plane 0.5 mm over the test-piece surface (lift-off 0.5 mm). A large magnetic leakage can be found at the bottom side of the test piece that shows a valley pattern inclined with the axis of the test-piece. This phenomenon associates us with a possibility of a global plastic slipping i.e. Ludas band. In other word, as we consider the magnetization arises from the damages of plastic deformation, more plastic damages may exist in the bottom side of the test-piece. To

investigate the damage state of this test-piece, small samples are cut out from the unloaded test-piece after the 3rd tensile cycle (from ε_r=5.55% to ε_{max}=8.55%). As a result, it was found that the number of slipped grains at the bottom side is about 2 times over comparing with that at the topside. The detail observing results of the microstructure will be given in the following subsection.

Fig.3.12 depicts the B_y distribution of the test-piece NDT2 unloaded after maximum strain 5.8% was reached. One can find that there is no much difference from that shown in the Fig.3.11. This result agrees with the conclusion obtained from the in-situ measurement, i.e. the magnetization did not change much for the plastic deformation of a high level as a result of the saturation.

If the peaks of the flux density detected at the bottom side of the test-piece is a result of the slipping lines, the distribution of the magnetization at the tips of the slit after a tensile testing is of interesting for the verification of this conjecture. For this purpose, a tensile testing was applied to the test-piece NDT21 with the maximum strain selected as 3%. Fig.3.13 shows a in-situ measuring result of the B_y. Comparing with Fig.3.9, it is obviously that the detected flux density is much smaller than that of the case of NDT2. In addition, the distribution of B_y did not show significant difference in the vicinity of the crack tips. This result can be explained as that, though there is local slipping near the tips of slit, the magnetization did not change a lot because the slipped grains did not gather in same direction like the case of the test-piece NDT2 (the difference of the local and global slipping). This difference may comes from the the loading history, the geometry of the test-piece or the random property of the material grains. From this point of view, the assumption that a global slipping can led to a large magnetization does not conflict with this experimental result.

b). The microstructure of the test-piece NDT2 after large tensile deformation

As mentioned in the previous subsection, small samples are cut out from the test-piece NDT2 from selected positions as shown in Fig.3.14. For all the samples, observations using a normal optical microscope are performed at first. In the Fig.3.15, the microstructures at positions along the central line of the test-piece (top side, bottom side and in the button region) and at the edge of the test-piece (top side and bottom side) are given. No much difference was identified in the volume fraction of the δ ferrite phase at the top side, bottom side and at the button region (virgin materials). However, content of the ferrite phase is different at different rolling lines (the volume fraction at the central site is larger than that at the edge part) for the test-piece NDT2. Therefore, though the δ phase exists for a virgin SUS304 material, its volume fraction is not so large (less than 1%) and may not be uniform.

To investigate the difference of the microstructure between the top side and the bottom side of the test-piece NDT2, a scanning electronic microscope (SEM) is also utilized in the observations of the samples mentioned above. Fig.3.16 shows images of SEM for 2 samples taken from the top and the bottom of the gauge region respectively. It is clear that local slipping have taken place at many grains. The slipping lines are in two patterns crossed each

other with a slipping angle of about ±25°. For considering the effect of the local slipping, the numbers of the slipped grains at the samples of the top side and the bottom side were counted under an optical microscope. Table 3.3 gives some results about the number of the slipping grains. The number at the bottom side is about 2 times over comparing with that at the top side.

Table 3.3 Comparison of the number of the slipped grains

Region	Position	Number of locally slipped grains
Bottom side (peak region)	edge site	32
	central site	71
Top side (weak region)	edge site	16
	central site	36

Considering the nonmagnetic property of the austenitic phase in the SUS304 material, slipping lines shall not result in a natural magnetization directly excepting those occurred in the grains of δ phase. However, as the magnetic field is much larger at the bottom side where slipping lines have a higher density, some magnetic phase may nucleated in the austenitic area, say, a martensite transformation may occurred[9]. To conform this conjecture, a higher resolution observation is also performed by using a transmission electronic microscope (TEM). Fig.3.17 shows an example of the TEM images at the bottom side of the the gauge region. From Fig.3.17(a), one can find some special zones (black region) appeared at the positions where 2 sets of slipping lines cross each other, Fig.3.17(b) is a zoom in image of this special zone. Fig.3.18 gives the x-ray diffraction images at these positions. It is clear that the special zones in the Fig.3.17 are martensite phase as they have a bcc crystal structure. This means that the martensite transformation is a practical phenomenon for SUS304 material even under a simple tensile loading and at a room temperature.

c). The results of the moire method

From the results described above, it is possibly that the natural magnetization is mainly caused by concentrated plastic deformation such as the effect of the ludars band. However, it is not easy to understand the local concentration of deformation for the present testing conditions as it is approximately a plan stress problem if the affect of the grain size and the thickness of the test-piece can be omitted

To investigate the correlation between the magnetizations and the macro-strain, the distribution of the strain is measured by using the moire method as described previously. A typical fringe pattern for the test-piece NDT14 unloaded after the tension to maximum strain of 4.4% is shown in the Fig.3.19. From this figure, it is difficult to find that a concentrated deformation has occurred during the tensile testing. Actually, the results from the moire method agree well with that measured from the push type strain sensors as shown in table 3.4. Other measurement results of the NDT14 after cyclic tensile loading and those of NDT13 after fatigue testing support this assumption. On the basis of these

results, one can not deny the possibility that a global slipping may led to a large natural magnetization. Actually, the flux density for the test-piece NDT14 and NDT13, in which no local deformation is found, is also very small. However, even for this case, the occurrence of the magnetization has also been verified.

Table 3.4 Comparison of the strains measured by the moire method and the strain sensor

Moire method	0.35%	0.91%	2.05%	3.52%
Strain sensor	0.36%	0.95%	2.19%	3.78%

Fig.3.20 and Fig.3.21 depict the in-situ measuring results of test-piece NDT14 during tension with strain range 0.08% $\sim$ 0.5% and 0.35% $\sim$ 1.08% respectively. The magnetization has been induced again though it is much smaller than that of the test-piece NDT2. However, the magnetization is in the same order with that measured from the test-piece with a central slit (NDT21). In other word, the magnetization in a small magnitude can be induced even in case that there is no global slipping band occurred. In this case, this magnetization can be considered as a result of the anisotropy in the δ phase grains of the SUS304 material that may be caused by the dislocations and other mechanical damages from the plastic deformation.

3.3.2 Results of the Fatigue Testing

a).The results of the test-piece with central slit

To investigate the affect of a fatigue crack on the natural magnetization, zero tension fatigue testings have been performed for the test-piece NDT21 (with a residual strain of about 2.8%) and NDT20 (virgin material). The testing conditions listed in the table 3.2 were applied at a room temperature. For the test-piece NDT21, through fatigue cracks of about 3mm were initiated after about 900 cycles at both the two tips of the central slit. The distribution of the flux density B_y measured after unloading is shown in Fig.3.22. From the figure, it is easy to find that a significant magnetic field signal was detected at the vicinity of the fatigue crack. On the other hand, fatigue cracks of about the same length also have been initiated at the tips of slit after about the same cycles for the test-piece of virgin material. The distribution of the flux density for this case is given in Fig.3.23, from which one can find that the magnetizations are induced again nearby the fatigue cracks. Comparing with the results shown in the Fig.3.22, the magnetization for a virgin material test-piece is smaller than that of the test-piece with a residual strain. Based on these results, one can conclude that a fatigue crack in a SUS304 structure component can be recognized nondestructively by monitoring the leakage signal of the natural magnetic flux.

b). Magnetizations near the fatigue crack

Visualizing the distribution of the magnetization at vicinity of the crack is important for investigating the principle of the magnetizing procedure and is also necessary for validating the code for inverse analysis, which is necessary in the prediction of the magnetization

distribution in the material from the measured flux density signals. As a jointed study of a research committee of the JSAEM named "the research committee for the electromagnetic fracture and its application to the nondestructive evaluation", the feature of the material nearby the fatigue crack was investigated by observing the surface magnetization with a magnetic colloidal method and by observing the surface distribution of the magnetic grains using the magnetic force microscope (MFM) for samples cut from the central part of the test-piece NDT21. The work was performed by the group of prof. Nakasone of TUS (Tokyo University of Science) with cooperation with groups at the national institute of metals of STA and the Mechanical Engineering Laboratory of the MITI Japan. Fig.3.24 shows a result of the colloidal method where the distribution of the magnetization in the vicinity of the fatigue cracks is illustrated [10]. From the figure, it is clear that the magnetizations mainly localized nearby the edge of the fatigue crack. In other regions including the region near the central slit, the magnetization is not significant. This result agrees with the prediction of the inverse analysis summarized in the first report of this work [11] and the inversion results of the measured data using a neuronetwork approach [12].

To investigate the distribution of the magnetic phase in the material near the crack, the MFM [10],[13] was used to visualize the microstructure at the test-piece surface and in the material. The measurements were performed after the interested region being cut out and polished by mechanical means. In order to reduce the affect of the mechanical machining, a further chemical polishing is also carried out. Fig.3.25 shows the position of the selected areas of the MFM scanning and Fig.3.26 gives a typical MFM image near the crack edge in case without chemical polishing. It is easy to find that, unlike the image obtained in the region far from the crack region, a maze like magnetic domain structure is clearly observable. This result tells us that even for the paramagnetic material like SUS304 steel, a magnetic domain structure is also possibly exist when fatigue damages was introduced, or in other words, magnetic phase is possibly transformed to a high volume fraction in the vicinity of crack. However, as the maze like magnetic domain is usually considered as a result of the mechanical polish, a chemical polishing is also applied for observing the real structure of magnetic domain induced by the mechanical damages. Fig.3.27 depicts a result of MFM observation for the same area shown in the Fig.3.24 for the test-piece after chemical polish. A cross slipping line system can be recognized in this figure, and a relative high force region can be found at the cross point of these slipping lines. This result agrees well with the observation result of the test-piece with tensile deformation, i.e., the martensite transformation is caused by the mechanical damage (slipping) at the region of the crack occurred during the crack propagation. As there is no similar magnetic domain structure was verified at a position far from the fatigue crack, one can consider the plastic deformation induced martensite transformation may only happens for a plastic strain of a high level.

c). Fatigue testing results for test-pieces without slit

For clarifying the evolution of the magnetization before the crack initiated, test-pieces

without central slit are also applied to the fatigue testing. Unlike the experiment of the test-piece NDT21 and NDT20, the in-situ signals during the fatigue testing are also measured. The introducing of a high accuracy A/D converter makes this possible as the data acquiring system used for the NDT21 and NDT20 is a relative old version one which has a precision even smaller than the magnitude of the natural magnetic field signals.

For test-piece NDT14, which has been applied in the cyclic tensile testing as described in subsection 3.1(c), the fatigue testing was terminated automatically at a cyclic number of about 4600 as the test-piece broken at a unexpected position (the top of the planar region where a small initial defect happened due to a failure in the fabrication of the grating lines). Therefore, the behaviors of the magnetization during crack initiation has not been caught. Fortunately, this defect is not fatal for the result of the tensile testing described in the last subsection as the defect is not significant and is far from the gauge area. Fig.3.28 shows a typical wave form of the detected flux density signals at the starting period of the testing with a comparison to that of the test-piece NDT13. The magnetic field changes with the oscillated deformation in the period of the applied loading (strain) though a phase different between them and a double period component can be recognized.

In case of test-piece NDT13, the fatigue experiment was performed successful until a fatigue crack initiated in the gauge region though it is not at the central area. The testing was suspended at cyclic numbers of 2000, 4000, 7000, 10000, 13000, 16000, 19000, 37200, and 54300, and the distributions of the flux density B_y were measured at these cyclic numbers for the unloaded test-piece that was performed carefully in order to terminate the testing at a state of zero strain (the strain monitored by the push type strain sensor). There is no significant magnetization change was conformed in the distribution of magnetic field in these 2-d scanning. This means the damage induced magnetization is smaller the the environment noise at least. Consequently, detecting the damages state before crack initiation is difficult by scanning natural magnetic field without using a shielding or other means for enhancing S/N ratio. After restarting the fatigue testing from cyclic number 54300, the test machine was stopped at cyclic number 63007 automatically as threshold value of the minimum loading was reached. After unloading, a tiny surface crack of about 2mm long was observed at the upside of the test-piece. In this case, a little perturbation can be distinguished in the distribution of the magnetic field though it is much smaller than that of the case of NDT21 and NDT20 (Fig.3.29).

Fig.3.30 shows the time history of some typical signals detected from the test piece NDT13. At the beginning of the testing, a relative large magnetic field change was found in its direct component. However, this change was saturated at about 10 cycles though a change at the amplitude of the magnetization wave can be identified. To show the phase change of the magnetic field signals and that of the strains, the hysteresis curves of the measured magnetic field signal are plotted versus the applied strain and stress referring the method used for fatigue detection based on the magnetostrition penomenon[14]. As examples, Fig.3.31 shows the hysteresis curves at the cyclic number of 10, 620, 3700, 7000, 19000 and 63000 versus the applied strain and Fig.3.32 shows those versus the applied

loading (stress). From Fig.3.31, it is easy to find that the area of the hysteresis curves increased with the increasing cyclic number. In the curves just given, the affects of the noise was reduced with a simple filtering operation, i.e., the high frequency noise is reduced by taking the signal as the summation of the neighboring sampling points (5 points were used) and the low frequency noise was reduced by just summing up the signals with those at the neighboring periods.

Comparing the signals of the virgin test-piece with that obtained from the test-piece with residual strain, one can find that the main different is the wave form (Fig.3.28). The peak value due to the tensile load is obviously smaller in the case of the virgin material.

3.3.3 Results in case with a magnetizing procedure

The results described in the previous sections are data for natural magnetic field. It is found that the field value is not large if considering its application to the damage inspection. In other word, though the method using natural magnetic field can be used to identify the fatigue cracks and even possibly to be used for its classification and sizing, the inspection of the damages is no easy as the signal is in a same order with the magnetic field of the earth and even smaller. This means that the noise at a practical environment may makes the signals of 2-d scanning being polluted and may led to a unbelievable inspection result.

Instead of applying the natural magnetic field to evaluate the damage status, another possibility is to measure the magnetic coefficients of the deformed material like what has been done for the magnetic materials [3], i.e. to detect the damage in the nonmagnetic/paramagnetic material with a similar way with that used for the ferromagnetic materials. For this purpose, the magnetic property of the test-piece NDT12 with different plastic damages was investigated by using the same loading procedure with the test-piece NDT14 and the magnetizing method described in the previous section. In practical, the test-piece was demagnetized at first, and a permanent magnet was used to magnetize the test-piece then with the procedure described in subsection 2.3(e). The leakage magnetic flux of the magnetized test-piece was measured before setting it to the loading system. Having applied strains to a maximum value listed in the table 3.2, the test-piece was unloaded and the distribution of the magnetic field was measured again. This procedure then was repeated for each tensile cycle of the NDT12. From this experiment, the behaviors of the magnetized test-piece under tensile and fatigue loading, and the evolution of the residual magnetic field for different plastic damages can be obtained.

Fig.3.33, Fig.3.34 and Fig.3.35 show the distribution of the magnetic field after magnetizing the demagnetized test-piece NDT12 that has been loaded to a maximum strain of 1.0%, 2.0% and 6.0% respectively. The figures for the other strain cycle are not given here as the results for the maximum strains less than 2.0% is almost the same with that for the virgin material. In addition, it is also verified that the residual magnetic field for different test-piece does not change much. However, after 2.% strain applied, the B_r begin to get larger. As shown in the Fig.3.33, the maximum $B_{r,y}$ becomes over-range though the

magnetizing procedure is just the same. On the other hand, the $B_{r,y}$ did not change much after 200 fatigue cycles of a 0.5% strain range were applied to the test-piece NDT12 (after tension to strain 6%).

Figs.36 $\sim$ 39 show the in-situ measuring results of the changes of the flux density for the magnetized test-piece. One can find from these results that a significant change of magnetization occurs due to the plastic deformation. Unlike the effect of the inverse magnetostriction [14], the signals of the detected magnetic field shows an irreversible property. In the Fig.3.34 and Fig.3.35, the magnetic field changed in the elastic region is very small comparing with that occurred at the area of the plastic deformation. However, for the elastic deformation of the test-piece with residual strain, the magnetization in the material changes with the applied loadings. In other word, the magnetization does not variate proportion to the plastic deformation but depending on the strain in a similar pattern of the stress-strain relation. However, the magnetization is irreversible if one notice that the magnetization did not decrease much when the loading released. It is also can be find that the proportional limit of the stress corresponds to the proportion point of the signal of the flux density signal in case of a large residual strain (more than 1.0%).

Fig.3.40 gives the in-situ signal of the magnetic field during fatigue testing for the test-piece after tension to 6.0% and magnetized with the permanent magnet. The direct component of the magnetic field changes rapidly at the first several loading cycles and then becomes slower. The amplitude of the vibrated signals is also getting smaller with the increasing cyclic number. Comparing with the magnetic field of the tensile testing, one can find that they change with a similar pattern. This means that the properties obtained from the tensile testing may applied to the test-piece subject to fatigue loadings.

3.4. Discussions

3.4.1 The principle of the natural magnetization

Based on the experimental results described in section 3, the principle of the damage induced natural magnetization can be considered as the follows:

For the simple tensile testing of a relative lower strain range, the magnetization occurs mainly due to the anisotropy caused by the plastic deformation, or in other words, due to the plastic damages in the test-piece such as the dislocations and slipping lines in the grains or at the grain edges [15],[16]. The damages affect the direction of the axis of easy magnetization and make the spontaneous magnetization in the grains of magnetic phase changing direction to the easy axis with a higher possibility. Actually, as shown in the previous sections, grains of the δ ferrite phase exist in the SUS304 stainless steel though its volume fraction is not so large comparing with the austenitic phase. These magnetic grains is considered as the source of the paramagnetic property of this material. A magnetic domain structure may occurs in these magnetic grains and its direction may be affected by the anisotropy of the material. Once dislocations or slipping occurred due to a plastic deformation, some domain walls will be moved in order to make the total potential being minimized that may led to the natural magnetization. However, for the tension of a large strain, the martensite transformation is also possibly happen that can led to an extra natural magnetization considering the volume fraction increment of the magnetic phase.

This explanation of the natural magnetization is reasonable considering the phenomena we find in the experiments. The occurrence of the large magnetization of the test-piece NDT2 can be considered as the result of a large local slipping and the martensite transformation. A global slipping (Ludas band, not only slipping in grains) may result in a strong anisotropy in the test-piece. However, the occurrence of global slipping is not only depending on the conditions of the plastic deformation. A local microstructure and the loading history may also affect the formation of the global slipping band. This is the reason why there is no large natural magnetizations observed for the other test pieces, say, there are no global slip lines happened for test-piece NDT21, NDT14 and NDT2. If there is no global slipping lines occurred, the natural magnetization will be small as the slipping lines in the grains may take different directions as shown in the observation results of the microstructure (Fig.3.16). On the other hand, the results of the flux density in the magnetized test piece is much larger than that for the demagnetized ones. This can also been explained by the conjecture above. In this case, the magnetic domain walls are moved due to the energy of the external magnetic field, which enables a global magnetization. Once damages are introduced by a mechanical energy, some domain walls will move back or to the easy axis as the present direction is not stable that makes the detected leakage flux density decreased. Considering the coexistence of the two sets of slipping lines that is crossed each other, this decrement is not difficult to be understood.

In case of the fatigue cracks at the tips of the central slit, the principle of the natural magnetization is a little different. In this case, in addition to the magnetizations induced with the same mechanism of the tensile testing, the martensite transformation occurred near the fatigue crack as a result of the cross slipping and mechanical energy may plays a major role of the natural magnetic field. Of cause the increment of the magnetic phase is not equal to more natural magnetic field because of the random orientation of the spontaneous magnetization of the magnetic domains. However, as the anisotropy is more significant than the simple tensile testing considering the stress concentration, more magnetic phase can led to a large natural magnetization. This can be considered as a reason of that the natural magnetic field at the crack vicinity of the deformed test-piece is larger than those of the virgin material.

Actually, from the observation results of the magnetic colloidal method and the MFM, the possibility of the martensite transformation in a fatigue testing is conformed. Though the results of the colloidal method only can show that a large magnetization exists in the vicinity near the crack, whether it is from the slipping or the martensite transformation can not be distinguished. However, from the results of the MFM image, one can say that the magnetic phase exists in a much larger volume fraction comparing with the area without stress concentration and the area of virgin material. This can be considered as an evidence of the martensite transformation. In fact, the TEM observation of NDT2 supports this consideration. Actually. the martensite transformation of the NDT2 can be considered being caused by a tension-tension fatigue testing of 3 fatigue cycles.

3.4.2 The correlation of the magnetization and the plastic strain

Excepting the test-pieces with a global slipping and those magnetized using a permanent magnet, the magnetization signals are very small and even weaker than the magnetic field of the earth. The change of the magnetization is mainly occurred at the first stage of the plastic deformation, i.e. the natural magnetization will saturate when the plastic deformation gets too large. Fig.3.41 shows the flux density change at tensile loading cycle (different residual strain) for test-piece NDT14 and NDT2. It is obviously that the change of the magnetization in a test piece with high residual strain is much smaller than that happened in the virgin material.

As the natural magnetization is possibly affected by the state of the local deformation, (for instance, the magnetization of a test-piece with global slipping is much larger than that in a test-piece with same or more residual strain), it is not easy to apply the signal of the natural flux density to quantitative prediction of the state of the macrostrain, or the state of the mechanical damage of the plastic deformation. However, considering the fact that the magnetization do changes with the increasing mechanical damages for all the situations, the detection of the flux density signal is a possible way for monitoring the change of the state of the mechanical damages since a global slipping is hard to take place in the practical structural component. However, even for such applications, efforts

for reducing the environment noise is also important.

3.4.3 Correlation of the fatigue damages and the feature parameters of the detected magnetic field signals

From the measured 2-d distribution of the leakage magnetic field for the test piece unloaded during the fatigue testing, it is difficult to identify fatigue damages from the detected signal as the signal of the magnetization is very small and is polluted by the environment noise. This means that a 2-d scanning of the natural magnetic field may not gives a valuable information related to the status of the fatigue damages. However, if we compare the time history of the magnetic flux density, one can find a significant difference for signals of test pieces in different residual strain. This tells us that some feature parameters of the detected signals may connect with the damages, which consequently, can be used as the parameter to monitor the damage state of the test piece[14].

Fig.3.42 gives an evolution of the area of the hysteresis curve of flux density versus the applied strains (see Figs.31,32) and Fig.3.43 shows the change about the signal of the sensor 1. From these results, it is clear that the area increases rapidly at the first stage of the fatigue life. After about 10,000 cycle, the increment of the area becomes slower. On the other hand, Fig.3.44 gives a corresponding evolution procedure of the amplitude of the flux density signals. Unlike the area of the hysteresis, the amplitude does not change much at the first stage but increase linearly at the last period of the fatigue life. From these result, we can say that the area of the hysteresis curve is a suitable parameter for monitoring the fatigue damage, i.e., if the change of the area getting slower, which means the fatigue life limit is approaching.

3.4.4 The possibility to detect plastic damages from magnetic material parameters of the SUS304 steel

Fig.3.45 shows a correlation of the maximum residual flux density for the test pieces with different residual strain. From the figure, we can find that the maximum residual magnetization did not change a lot for the residual strain of 1% or smaller. For the residual strain greater than 2%, the $B_{r,max}$ gets large linearly. This phenomenon can be considered as the effect of the the martensite transformation as it can make the volume fraction of the magnetic phase gets larger, which in turn, can led to the increment of the residual magnetic field of the damaged material. From this point of view, the residual magnetic fields is possibly to be applied to the prediction of the volume fraction of the martensite phase, or in other words. the plastic damages can be identified nondestructively by monitoring the residual magnetic field if the damage state is not too small.

Considering the similarity of the mechanical damages from the tensile plastic deformation and from the fatigue testing, one may guess that the fatigue damage can also be detected by measuring the residual magnetic field. In other word, the maximum residual magnetic field is possibly to be used to predict N/N_f for a fatigue loading in small strain

range, though it may not be sensitive at the first stage of the fatigue life.

In table 3.5, the proportional limit of the of the $\varepsilon \sim \sigma$ and $\varepsilon \sim B_y$ curves are summarized. The maximum changes of the magnetic field of the 6 sensors for the loading cycles described in the section 3.3 are also listed in the table. The definitions of the $\varepsilon_p, \varepsilon_{py}$ and B_y^{max} are depicted in Fig.3.46. From this table, one can find that these 2 proportional limits are nearly the same for test-piece with residual strain over 1%. In addition, the change of the magnetic field during the tensile testing also stop to increase after 1% tensile strain was applied. These results show that the mode of damage may change at a plastic strain within tensile strain 1% $\sim$ 2%. Actually, this phenomenon agrees with the change of residual magnetic field and the saturation phenomenon of the natural magnetization.

Table 3.5 Comparison of the proportional limit ε_y of the $\varepsilon \sim \sigma$ curve and ε_{by} of $\varepsilon \sim B_y$ curve, and B_y^{max}, the change of the magnetic field during tensile testing to ε_{max}

	0.2%	0.5%	1.0%	2.0%	3.0%
ε_y (%)	0.107	0.122	0.157	0.165	0.188
ε_{by} (%)	0.2	0.213	0.153	0.151	0.182
B_y^{max}(Gs)	0.23	0.50	0.62	0.62	0.64

3.4.5 The possibility to detect damage by using the natural magnetization

From the experimental results and discussions given in the previous subsections, we can find that though the natural magnetic field is useful in the detection of a large fatigue crack, it is not easy to be applied to the evaluation of the damage state by scanning the natural magnetic field during a in-service inspection. However, it is possibly to be applied for monitoring the change of the damage status by set a magnetic sensor to positions that are considered as the weak point of the key structure component. As the signal of the natural magnetic field is not so large, more efforts for enhancing the sensing system is necessary such as employing a shielding device for protecting the environment noise. On the other hand, the feature parameter (area of the $B \sim \varepsilon$ hysteresis curve for instance) proposed in the previous subsection is sensitive to the fatigue damage, and is possibly to be applied to a structure component subjecting to a transverse loading. However, this method also has a drawback, as the area of the hysteresis curve or the amplitude of the signals need the information of the loading or strain. Unfortunately, this information may be not available for problems such as a low cycle fatigue or damage of creep testing.

Unlike the method using the natural magnetic field, the method predicting the residual magnetic field is more robust against the environment noise as a result of the external magnetizing. In addition, the measurement of the residual magnetic field is easy to be performed as an in-service inspection method. A high space resolution of the measurement can also be realized by using a small exciting coil (or permanent magnet) coupled with a magnetic field sensor. However, the correlation of the residual magnetic field and the fatigue damage (N/N_f) needs to be demonstrated later for the SUS304 material.

3.5. Conclusions and Prospect Work

Based on the experimental results described in the previous sections and the discussions, the following concluding remarks are obtained,

1. Natural magnetizations occurs for the SUS304 stainless steel due to a mechanical damage especially at the vicinity of the fatigue cracks. The natural magnetic field can be considered as the results of a mechanical damage (from the plastic deformation or a fatigue testing). Therefore, the measurement of the natural magnetic field can be considered as an efficient method for the NDE of fatigue cracks as the noise from the magnetizing procedure can be removed. On the other hand, because of the saturation phenomenon and the affect of global slipping, detecting the status of mechanical damages before a crack initiated is difficult by scanning the natural magnetic field. However, the natural magnetic field can be applied in the monitoring of the damage status of a given point if the environment noise can be reduced by using a special measuring system.

2. The area of the field-strain hysteresis curve increases with the increasing fatigue cyclic number. The amplitude of the magnetic field signal is also getting larger especially at the last period of the fatigue life. These parameters can be applied to the online monitoring of the status of the fatigue damage for key structure components subjecting cyclic loadings.

3. At a room temperature, the martensite transformation is also possibly to be occurred for a relative large tensile loading. At the tips of the fatigue crack, a martensite transformation also possibly happens due to a cyclic loading even of a small strain range. The reason of the natural magnetic field can be considered as result of both the anisotropy due the plastic damage and the increment of the magnetic phase due to the martensite transformation.

4. The residual magnetic field changes significantly for a test-piece with large plastic deformation. However, at a low plastic deformation level, the residual magnetic field will not change a lot. This phenomenon may be applicable for the detection of the martensite transformation and the damage recognition for materials with large mechanical damage.

As prospect work, the following subjects are important:

1. Investigating the correlation of the N/N_f and the feature parameter of the measured natural magnetic field for various test conditions and test-pieces.

2. Checking the correlation of the maximum residual magnetic field B_r with the density of the martensite phase and the N/N_f parameter and evaluating the possibility to be applied to the detection of fatigue damages.

3.6. References

[1] R.B.Mignogna, and et al., Passive nondestructive evaluation of Ferromagnetic materials during deformation using SQUID gradiometers, IEEE Trans. Appl. Supercond., Vol.3, No.1, pp1922-1925, 1993.

[2] Report of research committee on electromagnetofracture and its applications on non-destructive evaluation of degradation and damages, JSAEM report, JSAEM-R-9803, 1998.

[3] A.Gilanyi, K.Morishita, T.Sukegawa, M.Uesaka, and K.Miya, Magnetic nondestructive evaluation of fatigue damage of ferromagnetic steels for nuclear fusion energy system, fusion engineering and design, Vol.42, pp485-491, 1998.

[4] K.Yamada, and et al, Nondestructive cross evaluations of iron-based materials by magnetic sensors and laser speckle interferometry, Proc. Int. Symp. Mag. Mater., 1998.

[5] Y.Yamada, and et al., Application of thin-file flux-gate sensor, New Ceramics, No.2, pp15-18, 1998.

[6] T.Kunio and et al., Experimental method for fracture mechanics, Asakura Publisher, 1984.

[7] B.Han, Recent advancements of moire and microscopic moire interferometry for thermal deformation analysis of microelectronics devices, Experimental Mechanics, Vol.38, No.4, pp278-288, 1998.

[8] Y.Morimoto and et al., Moire analysis of strain by Fourier transformation, Trans. JSME, Vol.54-A, No.504, pp1546-1551, 1987.

[9] Y.Ozaki and et al., Elementary Metallography, Asakura Publisher, 1978.

[10] Y.Nakasone, Collaborative study on a new magnetic nondestructive evaluation of degradation in a stainless steel, Proceedings of the MAGDA'Brisbane, 2000.

[11] Z.Chen, K.Aoto, and S.Kato, Passive electromagnetic NDE for mechanical damage inspection by detecting leakage magnetic flux, I. Reconstruction of magnetic leakage magnetic flux, JNC report, JNC TN9400, 99-061, 1999.

[12] S.Takaya, G.Perad, T.Demachi and K.Miya, Inverse analysis of magnetization distribution for diagnosis of non-ferromagnetic steel, Proceedings of the MAGDA'Brisbane, 2000.

[13] T.Suzuki and K.Hirano, Fatigue damage analysis of austenitic stainless steel by magnetic force microscope, Proceedings of ECF12, Vol.1, pp97-102, 1997.

[14] A.Yoshinaga, and B.Yoshii, Detection of torsion fatigue in steels by using the effect of magnetostriction, Trans. JSME, pp343-369,1977.

[15] S.Chikazumi, and et al., Hand book of magnetic material, Asakura Publisher, 1975.

[16] S.Takahashi, Correlation of magnetization and dislocation in the region approaching to saturation, Report JSAEM, JSAEM-R-9704, pp27-38, 1998.

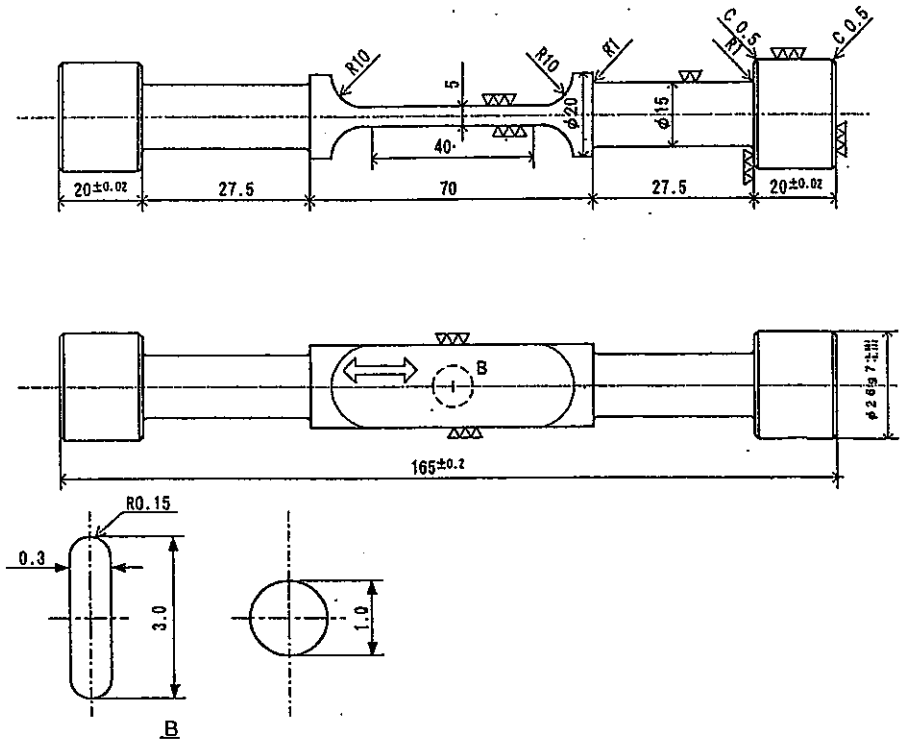

Fig.3.1 Shape of the button type CCT test-piece

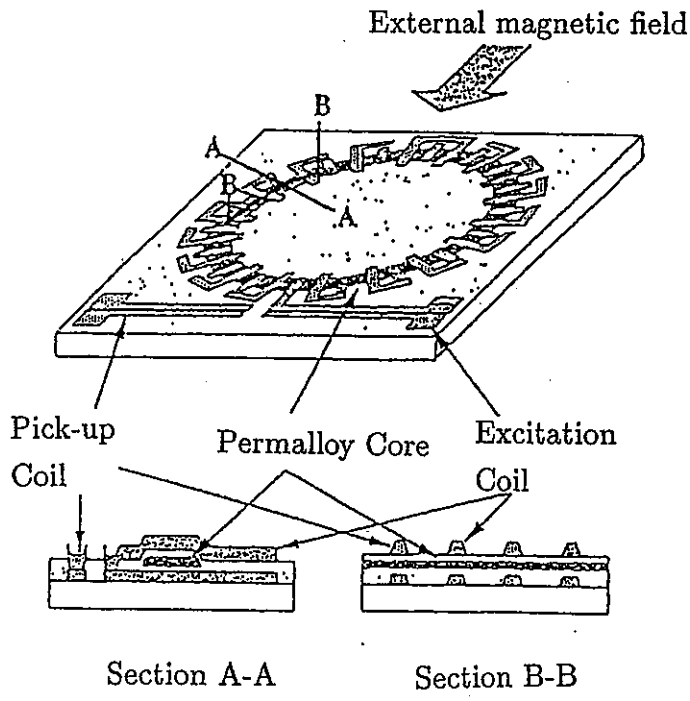

Fig.3.2 Principle diagram of the FG sensor

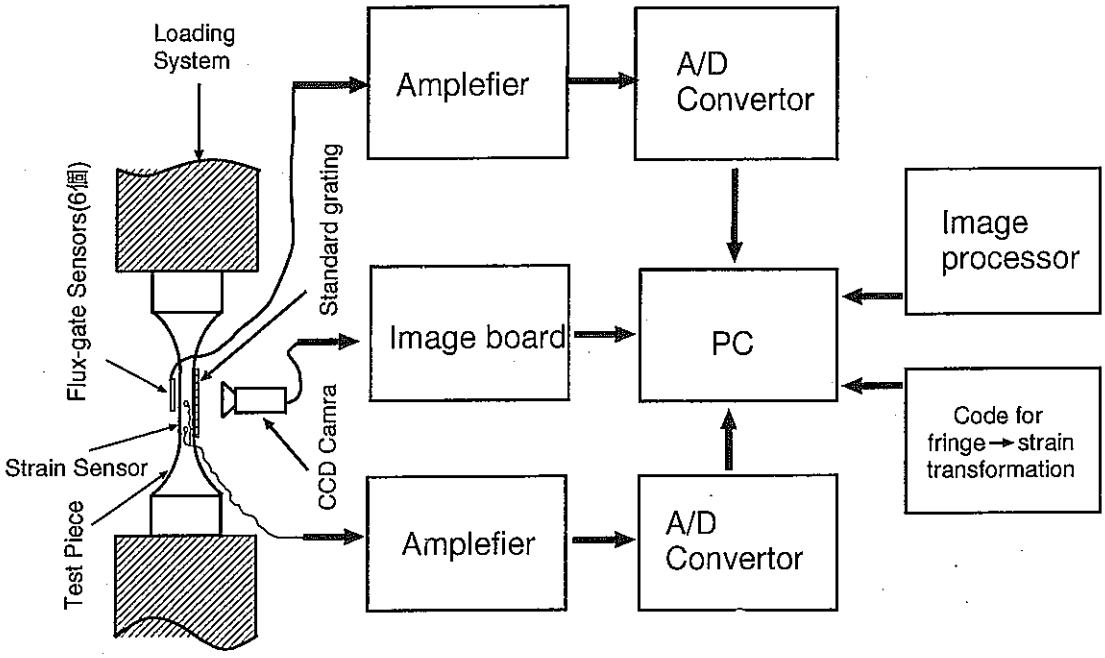

Fig.3.3 Schematic diagrams of the in-situ measuring system

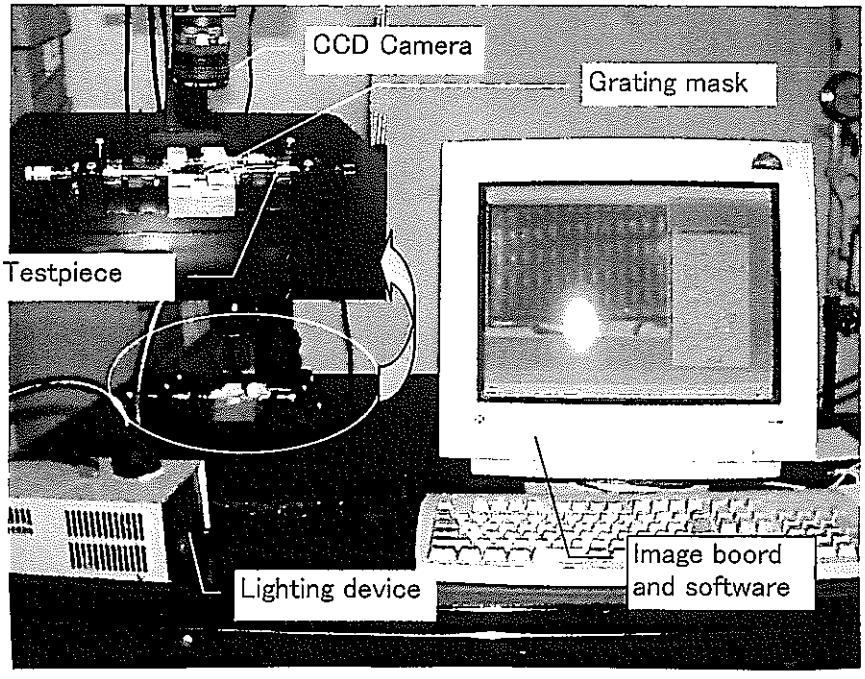

Fig.3.4 The measuring system of moire method

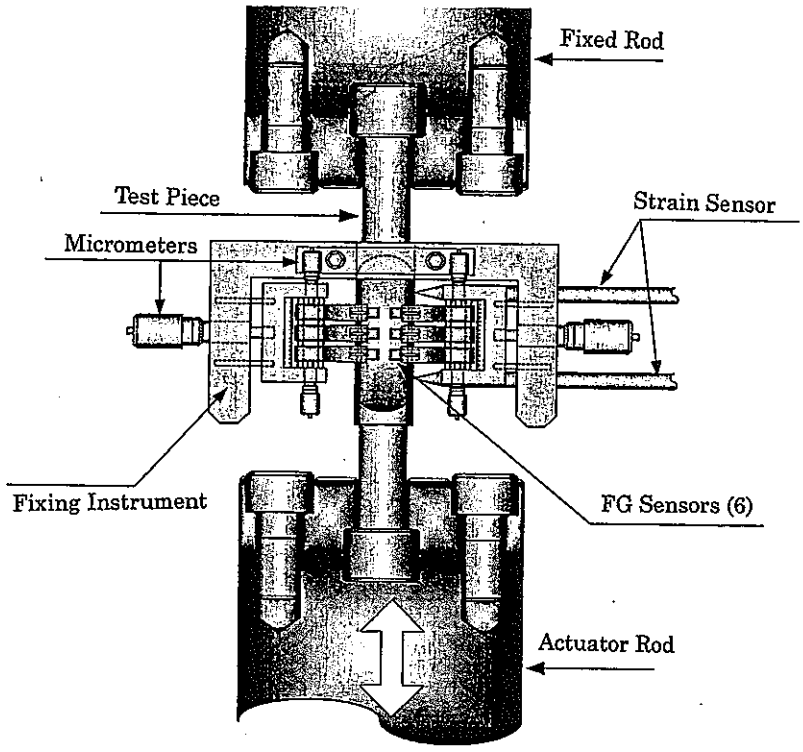

Fig.3.5 Fixing instrument for setting sensors

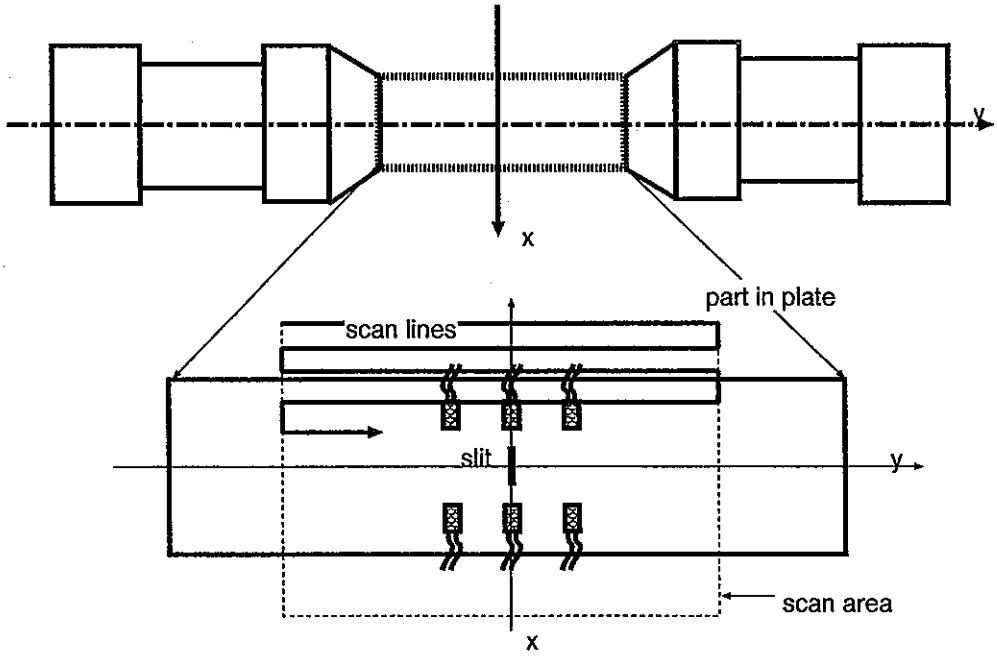

Fig.3.6 Setting locations of the FG sensors

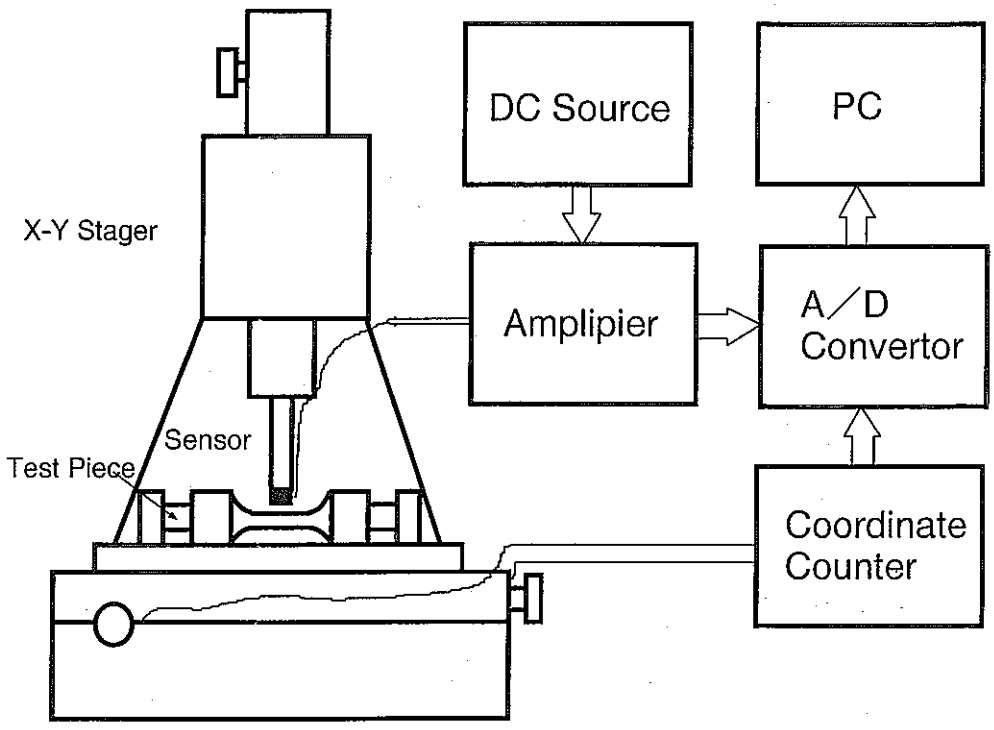

Fig.3.7 Experimental setup of the off-situ scanning system

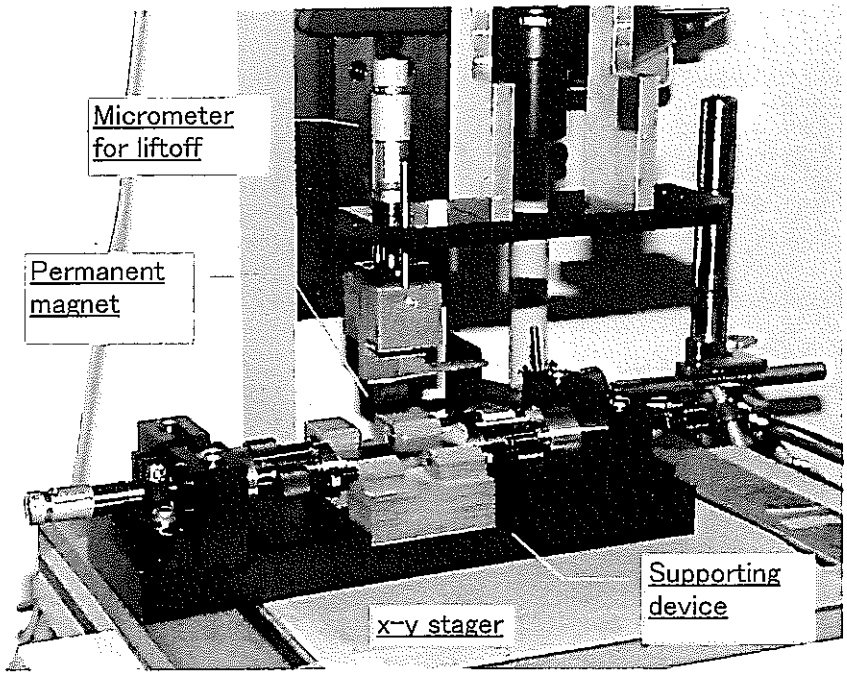

Fig.3.8 Setup of the magnetizing system

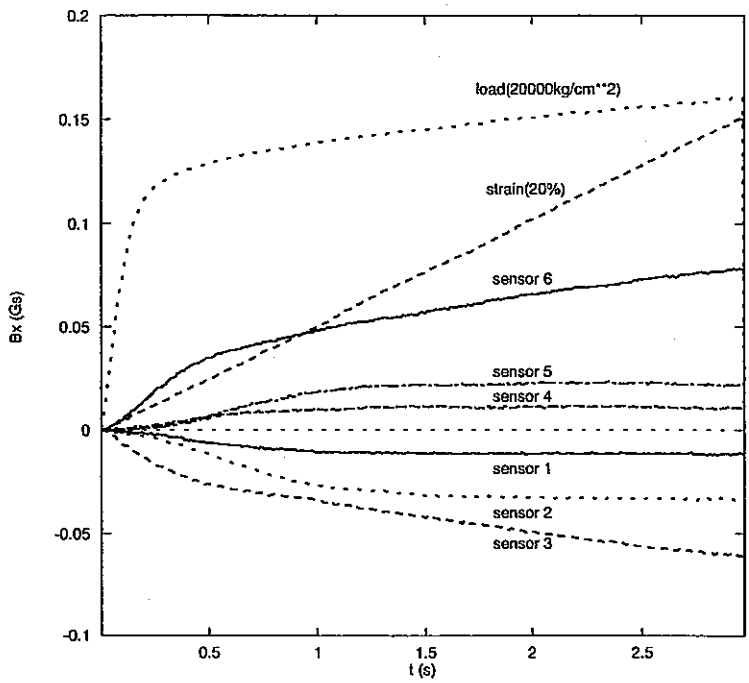

Fig.3.9 In-Situ measuring result of NDT2 during tensile testing (0% ~ 3%)

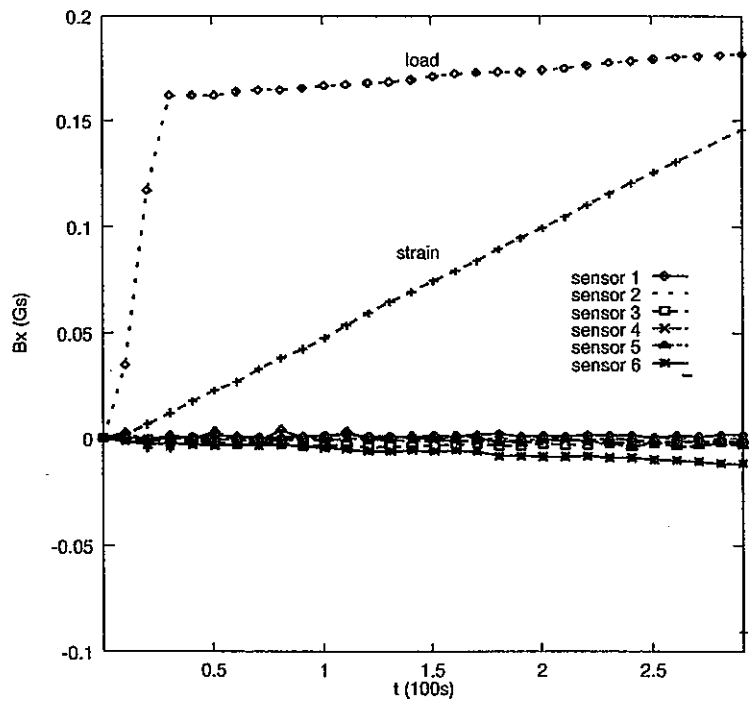

Fig.3.10 In-Situ measuring result of NDT2 during tensile testing (3% ~ 6%)

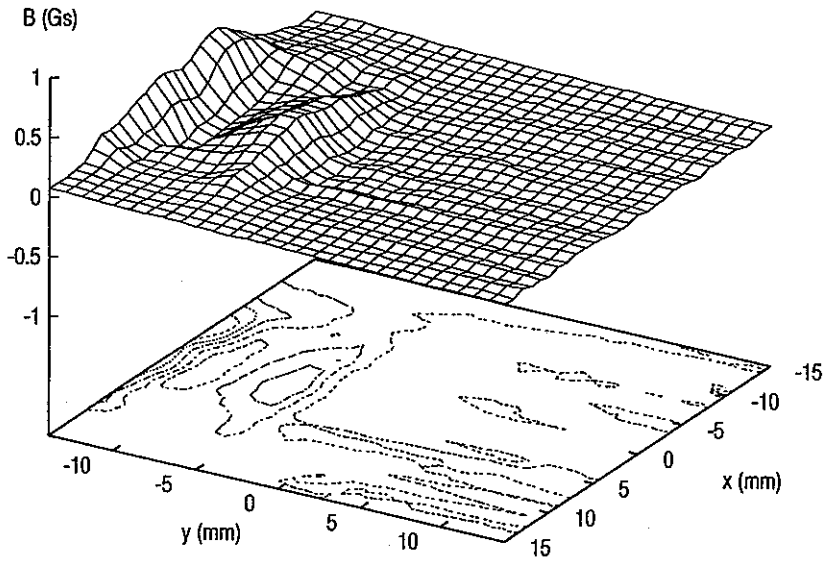

Fig.3.11 Distribution of the natural magnetic field after tensile testing (NDT2, 0% ~ 3%)

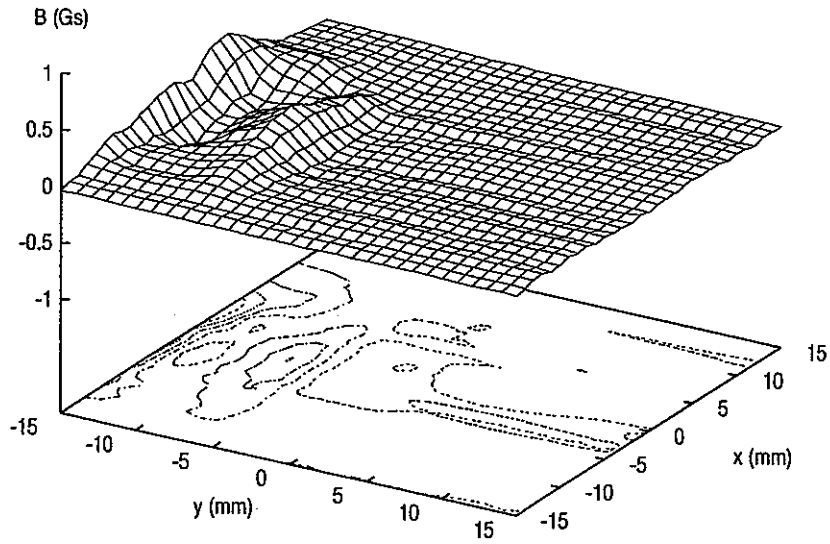

Fig.3.12 Distribution of the natural magnetic field after tensile testing (NDT2, 3% ~ 6%)

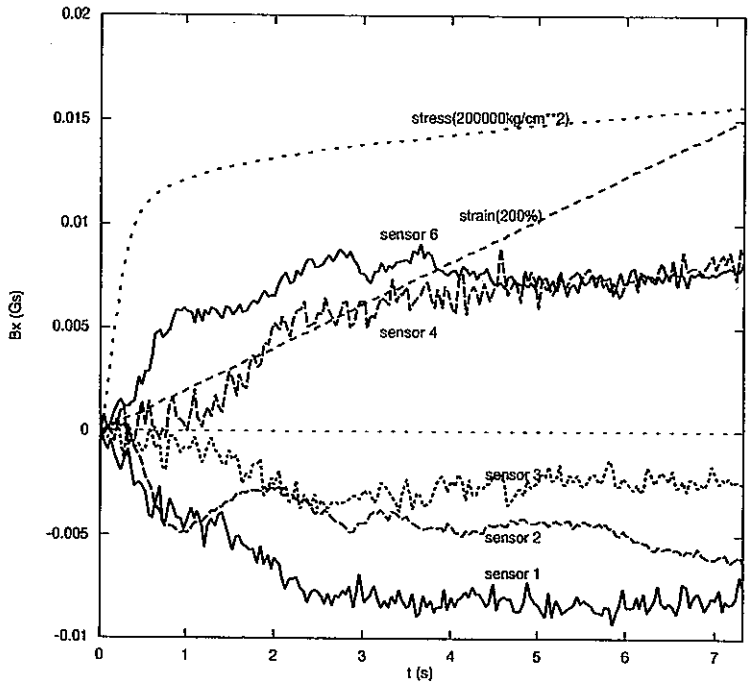

Fig.3.13 In-Situ measuring result during tensile testing (NDT21, 0% ~ 3%)

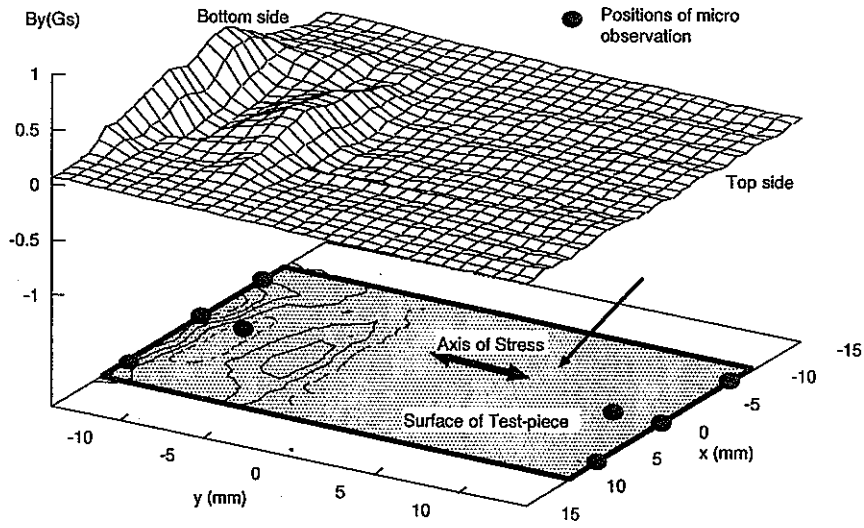

Fig.3.14 Location of the samples cut out from the test-piece NDT2 after tensile testing (NDT2, 6% ~ 9%)

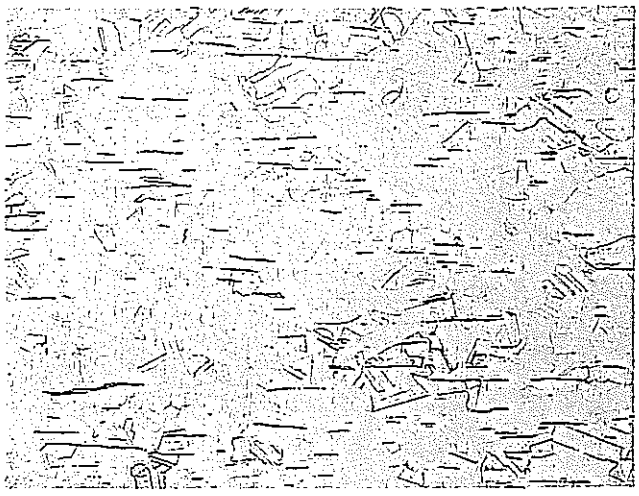

a). Center of the top side

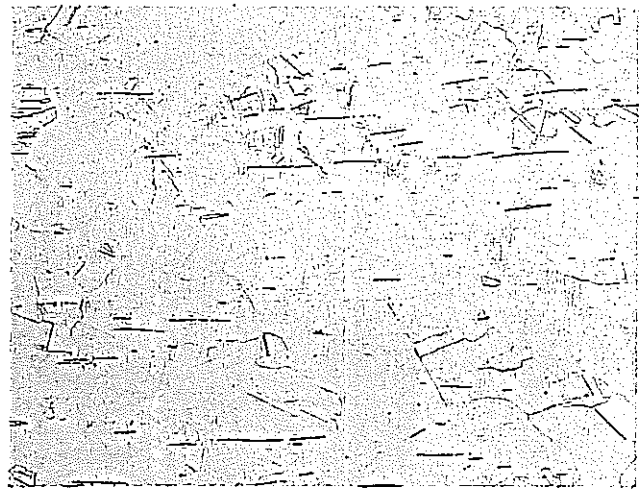

b). Right hand of the top side

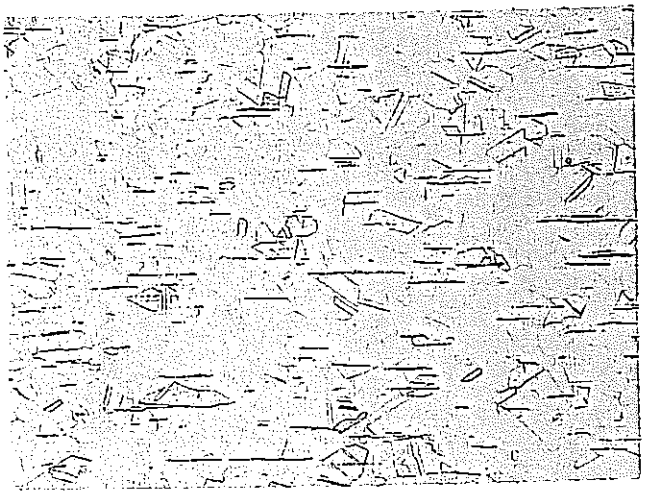

c). Center of the bottom side

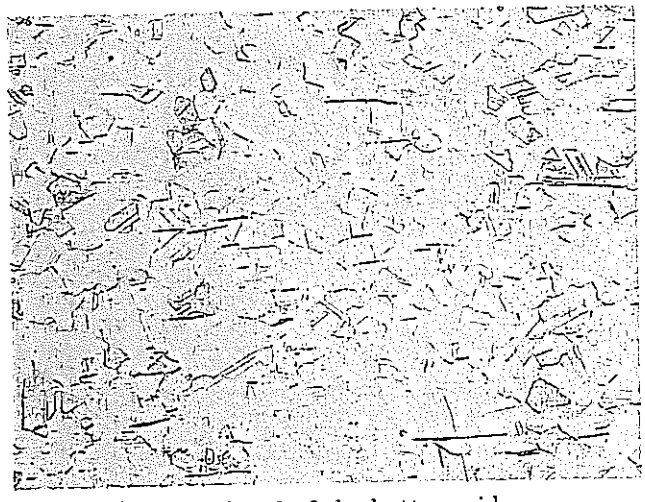

d). Right hand of the bottom side

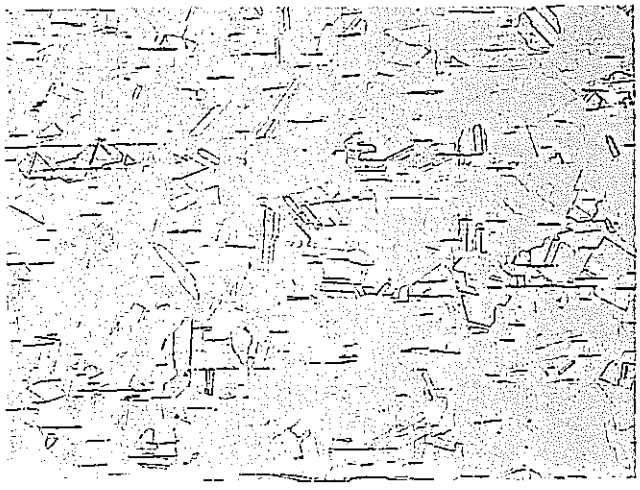

e). Vrigin material

Fig.3.15 Comparison of the microstructure of the samples taking out from different positions (NDT2, after 9% tension)

Sample at the top side

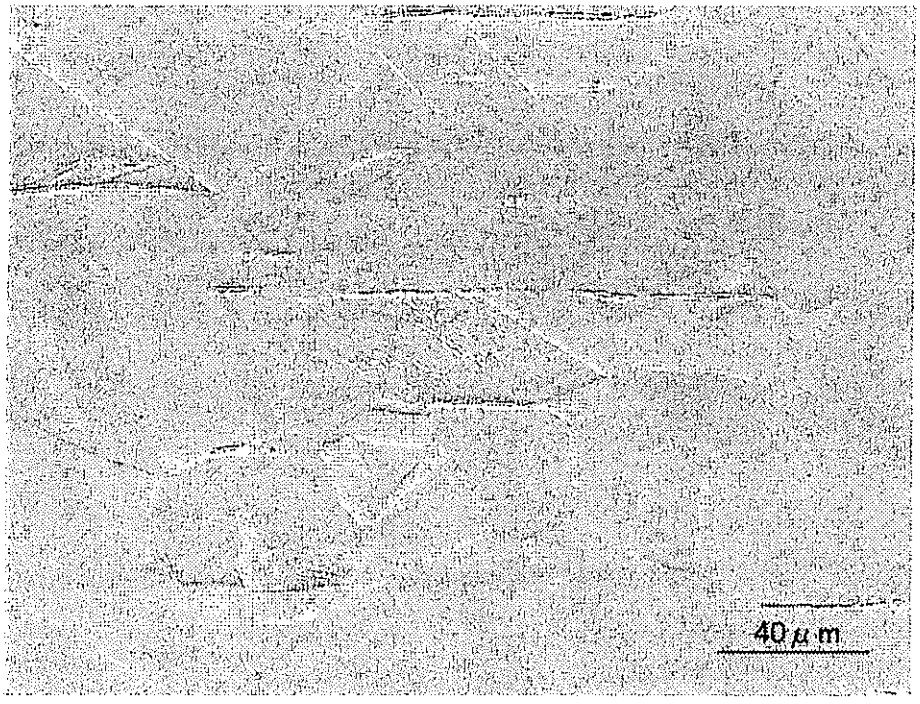

Sample at the bottom side

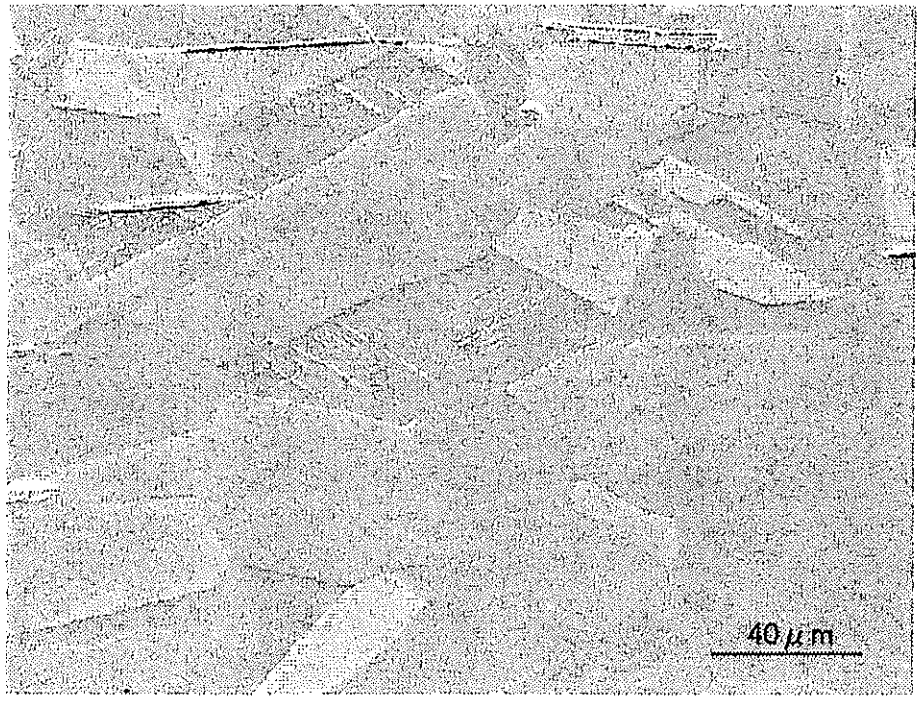

Fig.3.16 Comparison of the local slipping of the sample at the top and bottom side of the tesepiece NDT2 (after 9% tension)

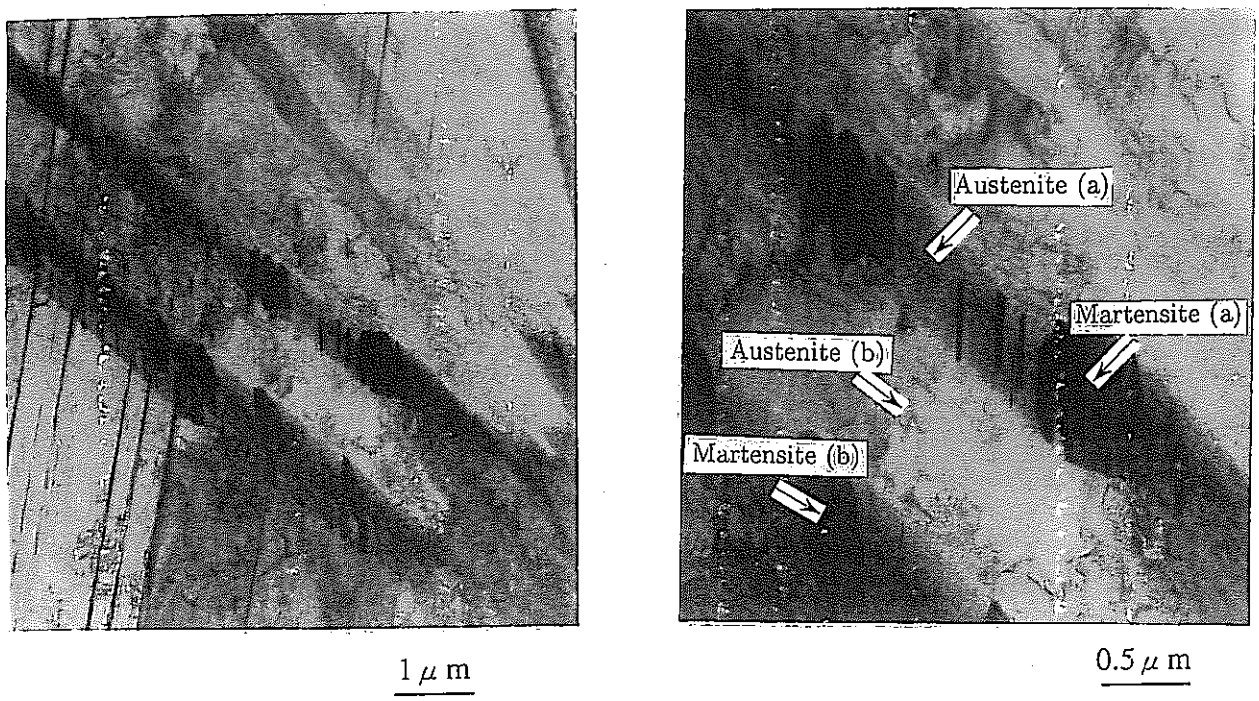

Fig.3.17 TEM image of sample cut from the bottom side of the tesepiece NDT2 (after 9% tension)

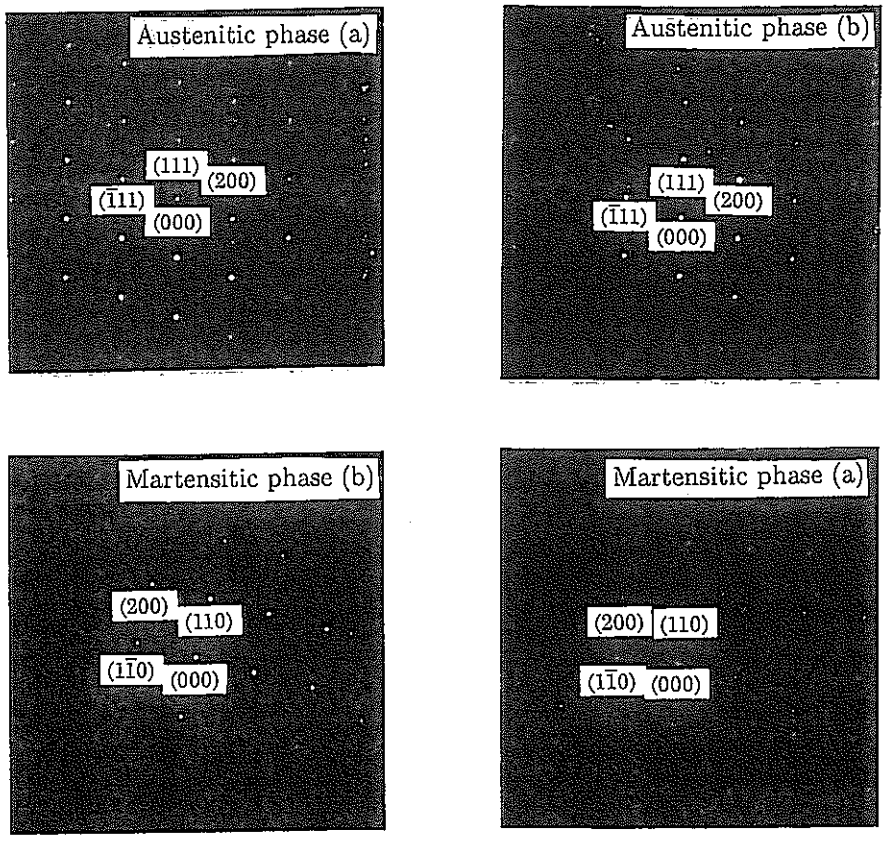

Fig.3.18 X-ray diffraction images for determining the property of the various phases shown in the Fig.3.17

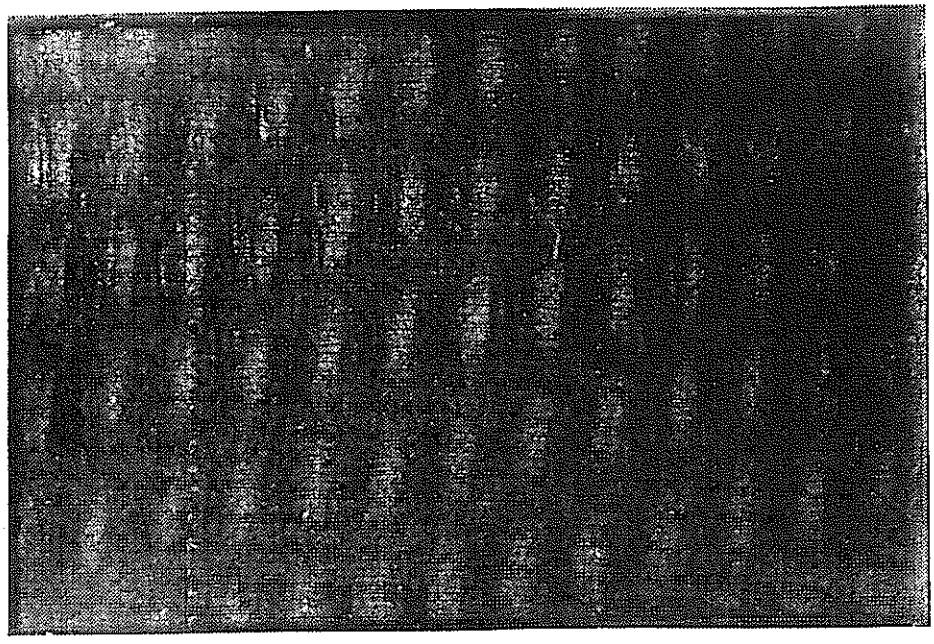

Fig.3.19 An example of fringe pattern of the moire method for test-piece NDT14 unloaded after tensile testing ($\varepsilon \simeq 3.78\%$)

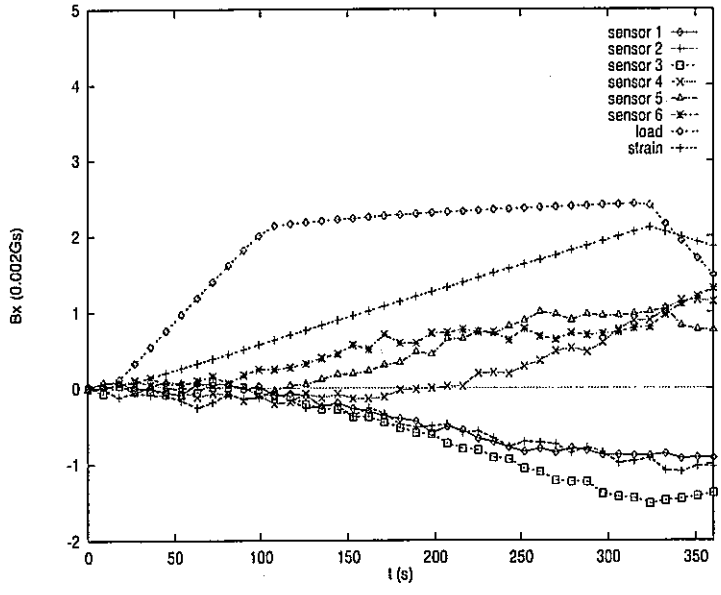

Fig.3.20 In-Situ signals for test-piece NDT14 and strain range 0.08% ~ 0.5%

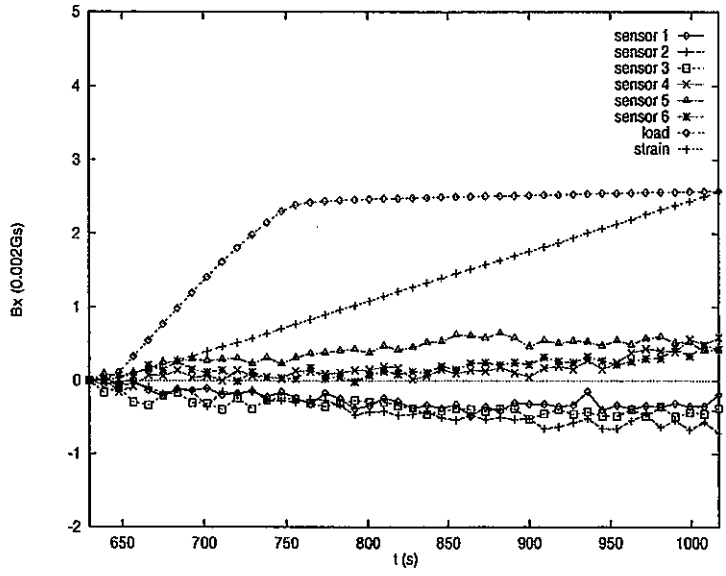

Fig.3.21 In-Situ signals for test-piece NDT14 and strain range 0.35% ~ 1.08%

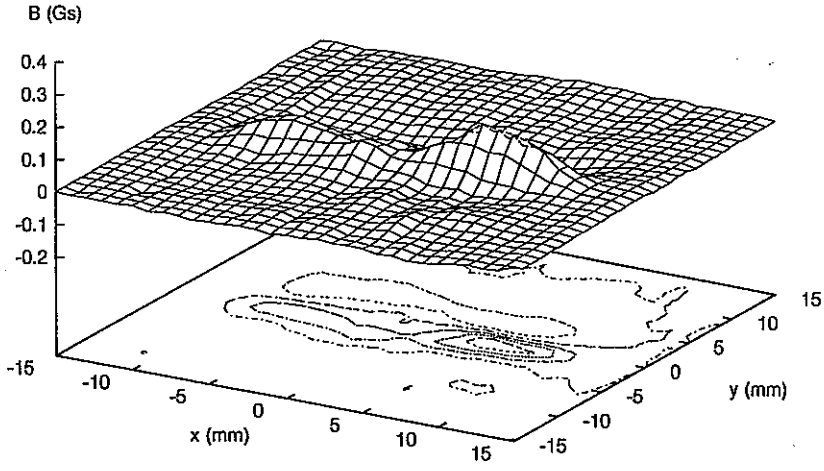

Fig.3.22 Distribution of the flux density for test-piece NDT21 after fatigue crack was initiated

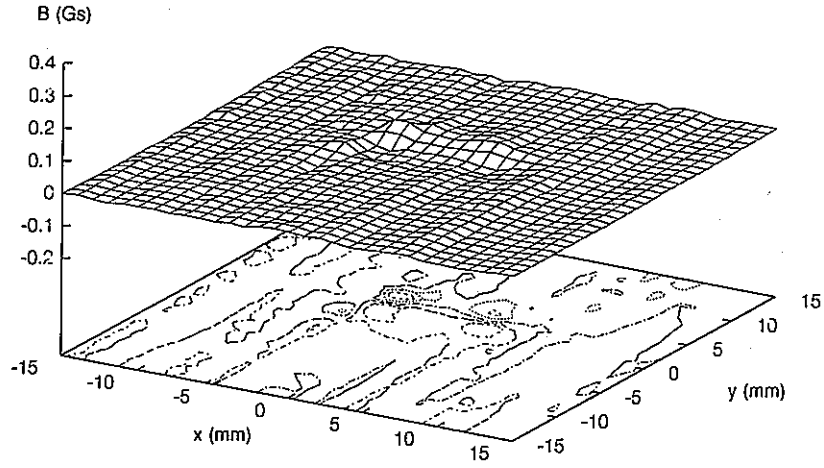

Fig.3.23 Distribution of the flux density for test-piece NDT20 after fatigue crack was initiated

Fig.3.24 The magnetization image at the crack tip of the test-piece NDT21 obtained by using the colloidal method (Provided by Prof.Y.Nakasone, To be published)

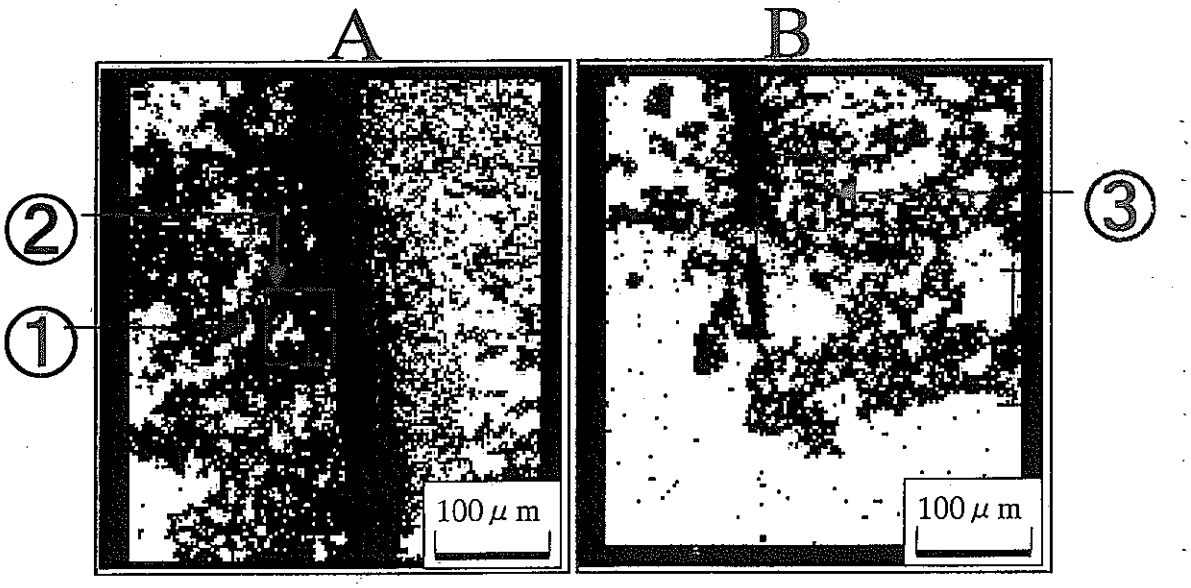

Fig.3.25 The observing areas of the MFM (Provided by Prof.Y.Nakasone, To be published)

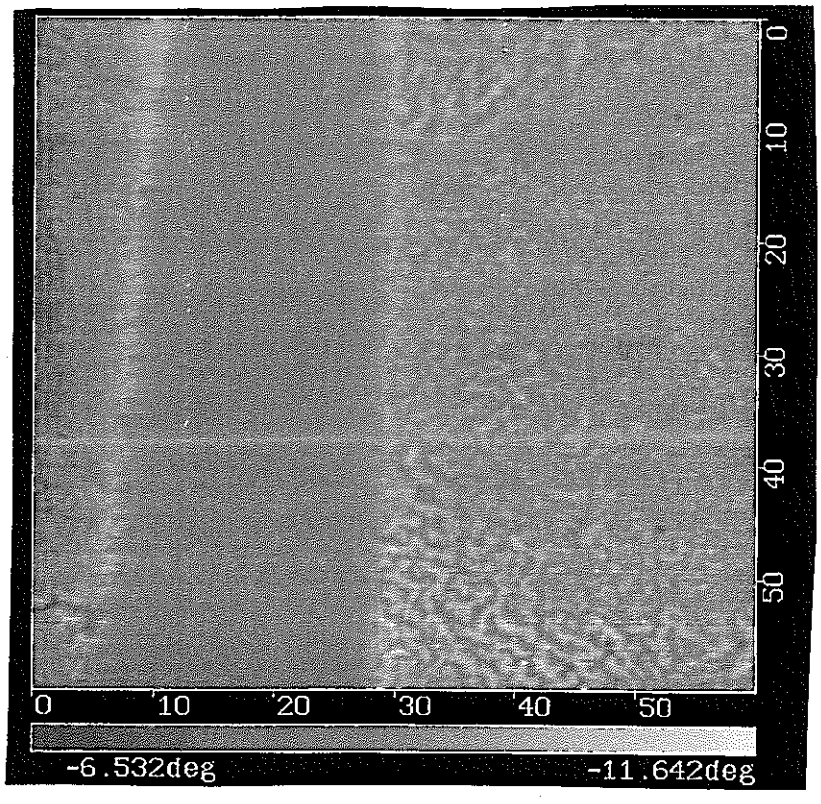

Fig.3.26 An example of the MFM image at the crack region observed before chemical polishing (Provided by Prof.Y.Nakasone and Dr.T.Suzuki, To be published)

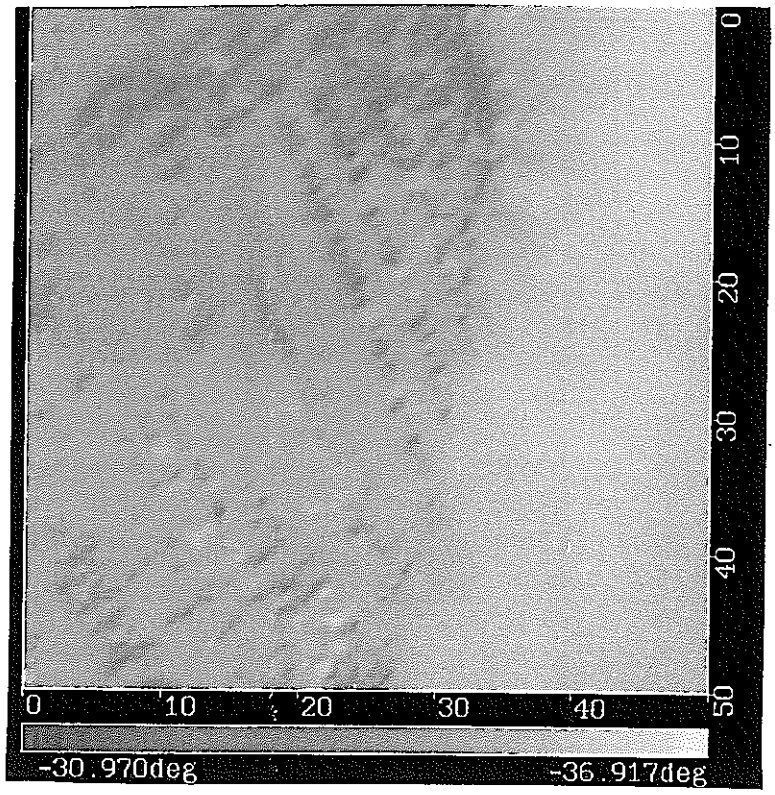

Fig.3.27 An example of the MFM image at the crack region after chemical polishing
(Provided by Prof.Y.Nakasone and Dr.T.Suzuki, To be published)

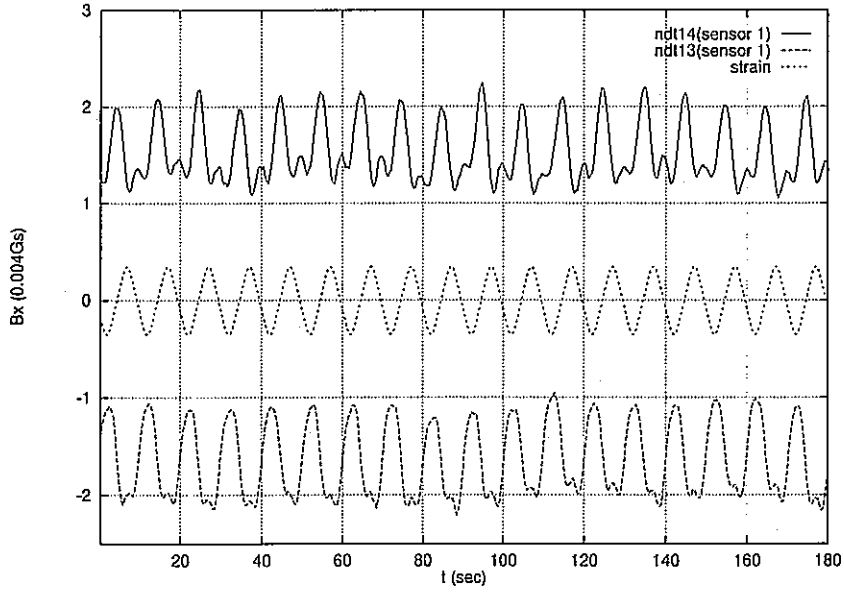

Fig.3.28 Comparison of magnetic field signal during the fatigue testing of test-piece NDT14 (with residual strain) and NDT13 (virgin material)

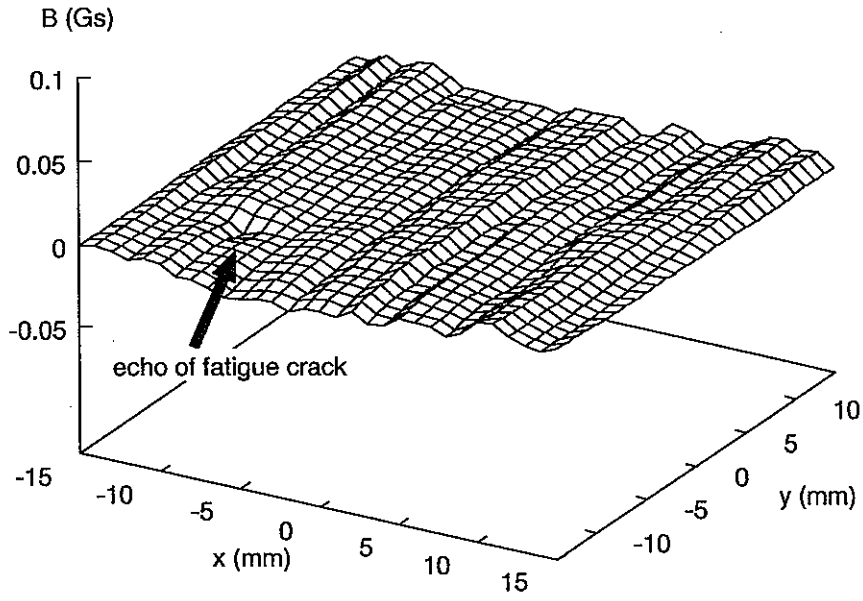

Fig.3.29 Distribution of magnetic field measured after fatigue crack initiated (NDT13, 63000 cycle)

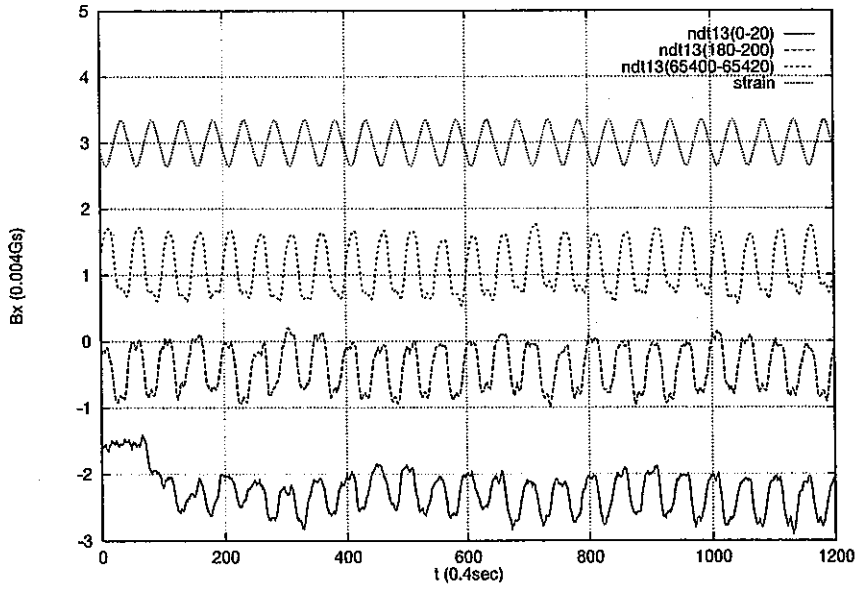

Fig.3.30 Magnetic field signal at different cyclic number for test-piece NDT13 (virgin material)

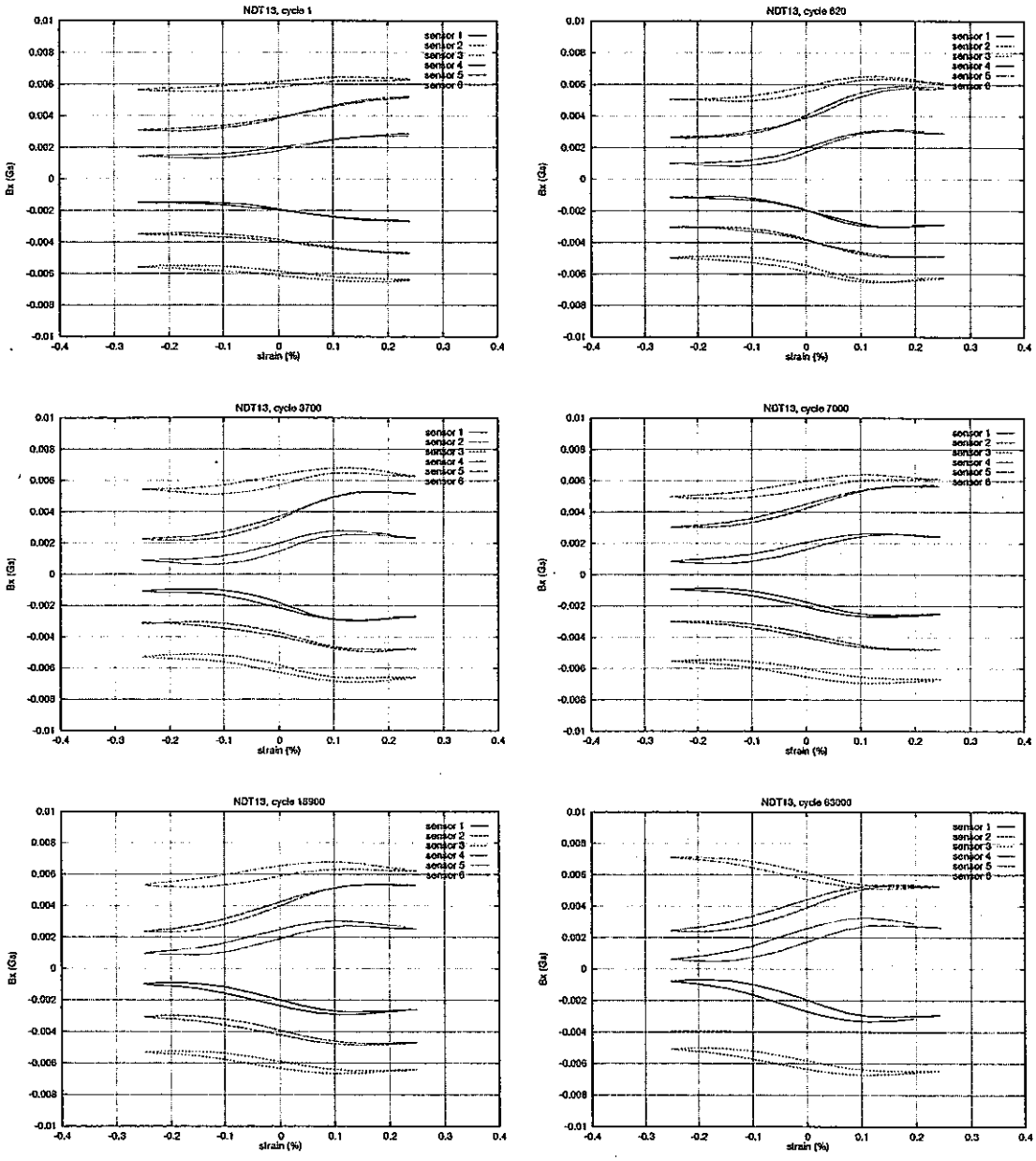

Fig.3.31 Typical hysteresis curves of the magnetic field versus applied strain

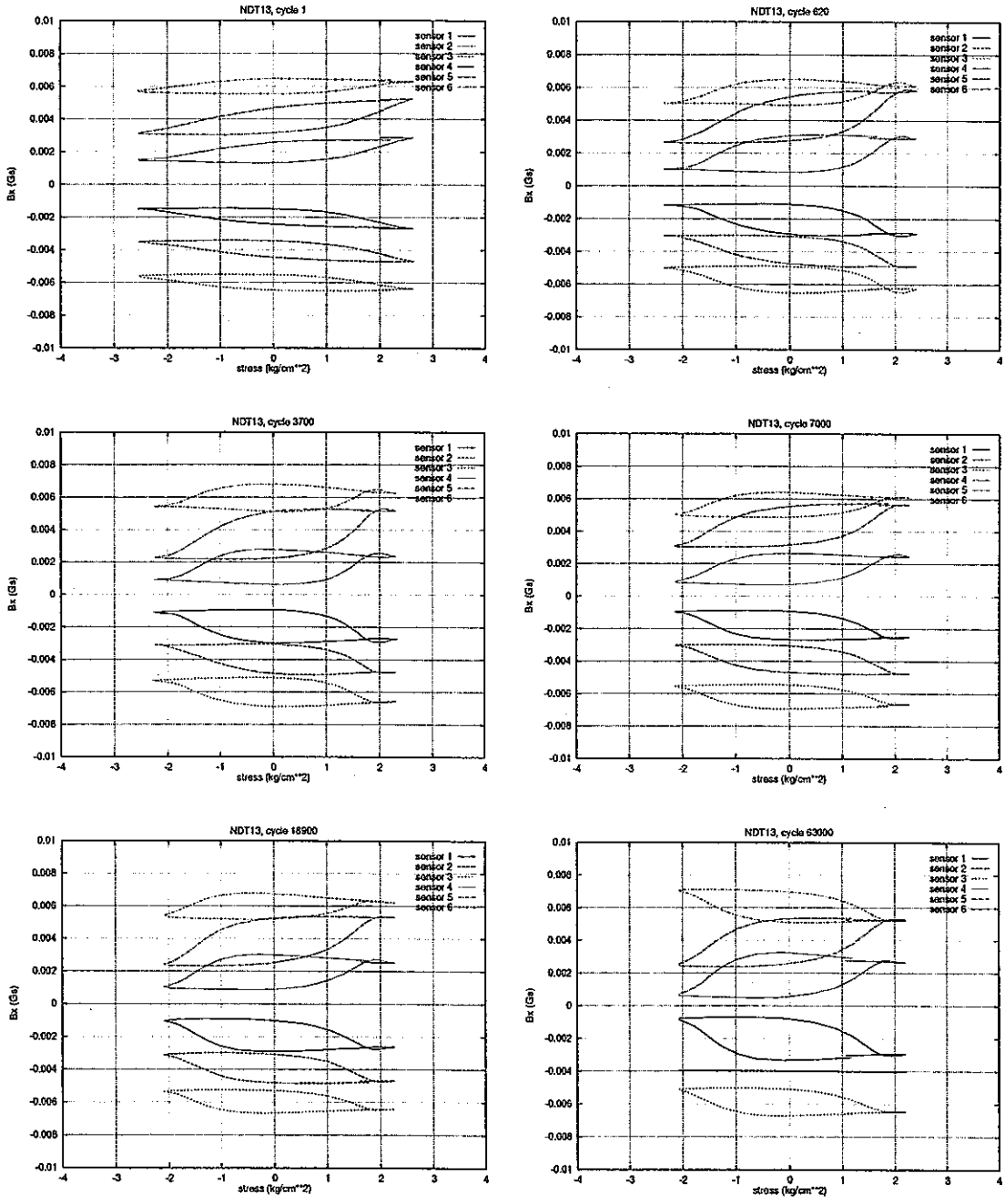

Fig.3.32 Typical hysteresis curves of the magnetic field versus applied loading

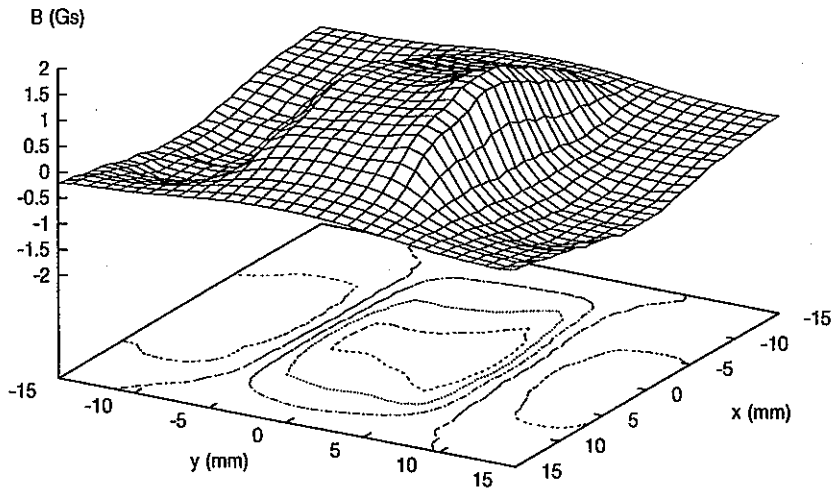

Fig.3.33 Distribution of the residual magnetic field B_y after magnetized with a permanent magnet (NDT12, Residual strain: 0.84%)

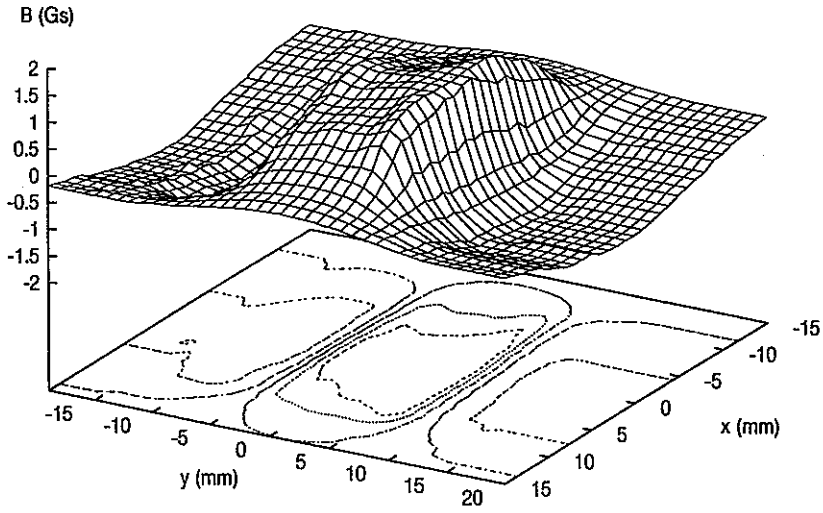

Fig.3.34 Distribution of the residual magnetic field B_y after magnetized with a permanent magnet (Residual strain: 1.82%)

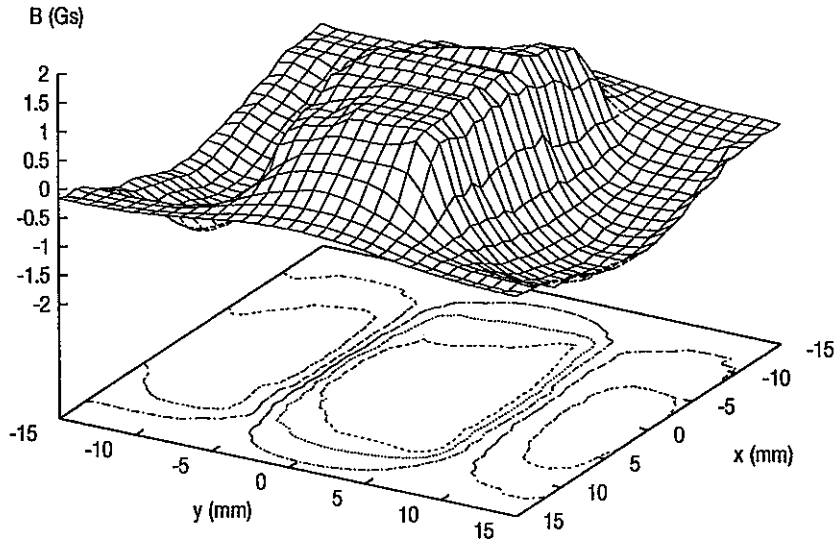

Fig.335 Distribution of the residual magnetic field B_y after magnetized with a permanent magnet (Residual strain: 5.76%)

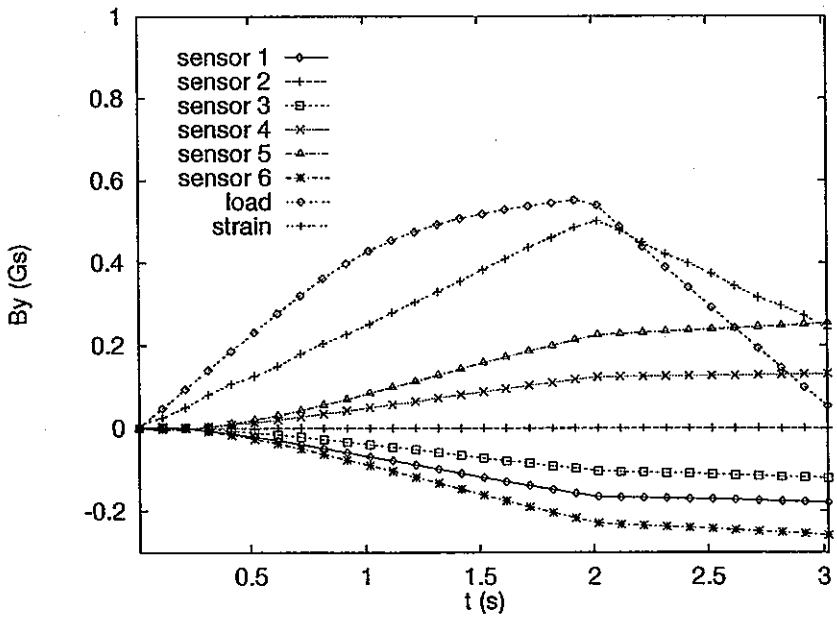

Fig.336 In-Situ measuring result for the magnetized test-piece NDT12 (strain range, 0 ~ 0.2%)

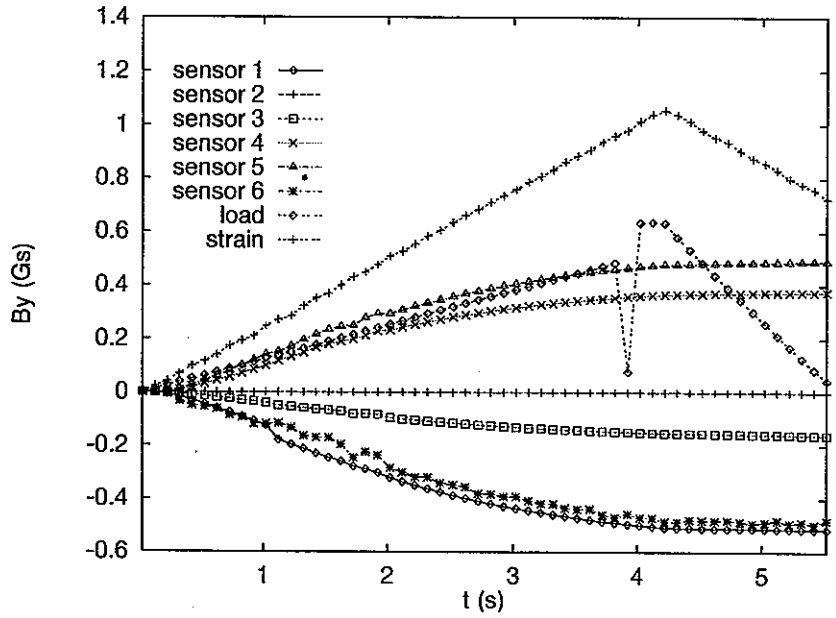

Fig.337 In-Situ measuring result for the magnetized test-piece NDT12
(strain range, 0.08% ~ 0.5%)

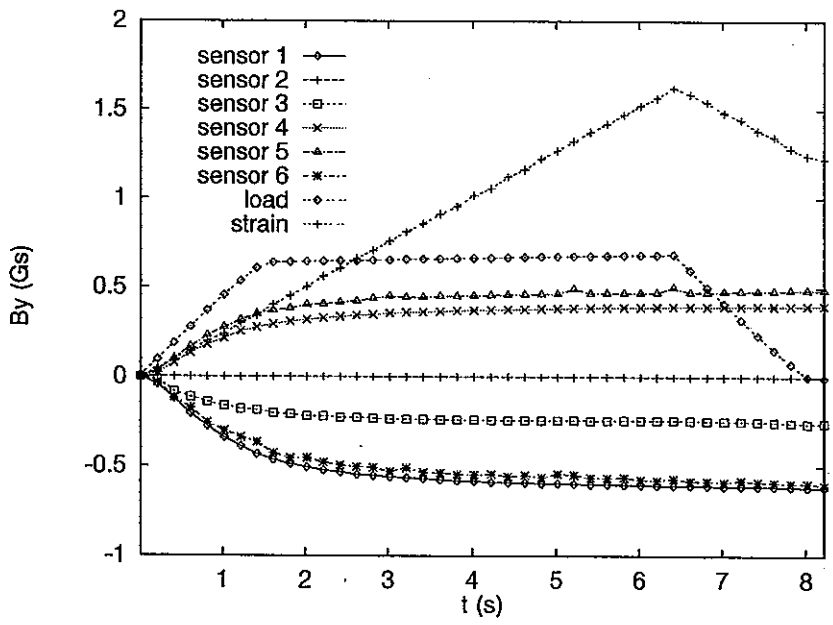

Fig.338 In-situ measuring result for the magnetized test-piece NDT12
(strain range, 0.35% ~ 1.0%)

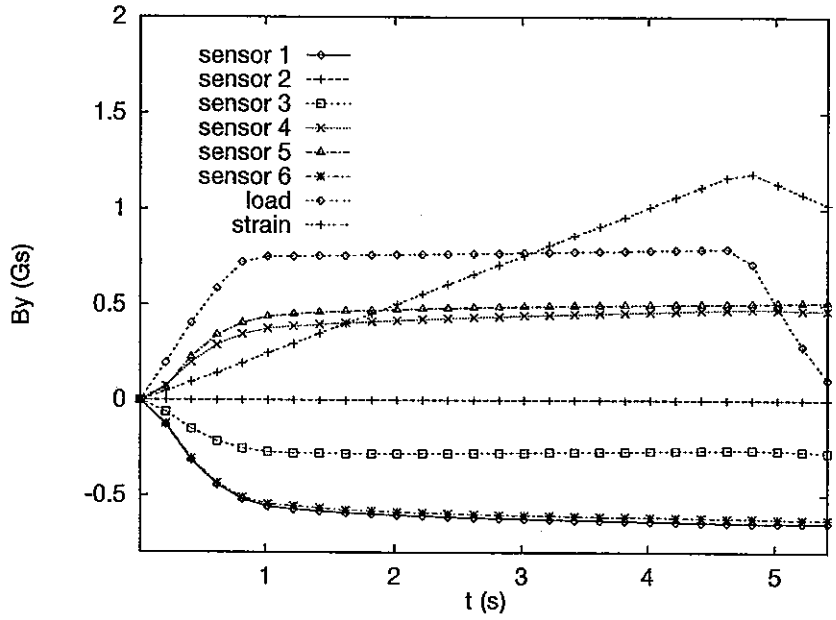

Fig.339 In-situ measuring result for the magnetized test-piece NDT12 (strain range, 0.95% ~ 2.0%)

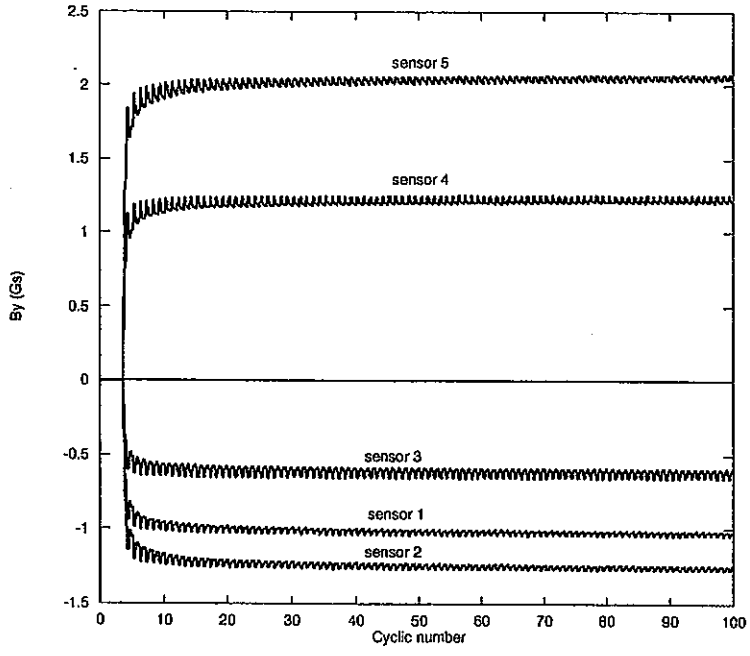

Fig.340 In-Situ signal of the magnetic field for test-piece NDT12, which is demagnetized/magnetized after a tension to a strain of 6.0% (0 ~ 100 cycle)

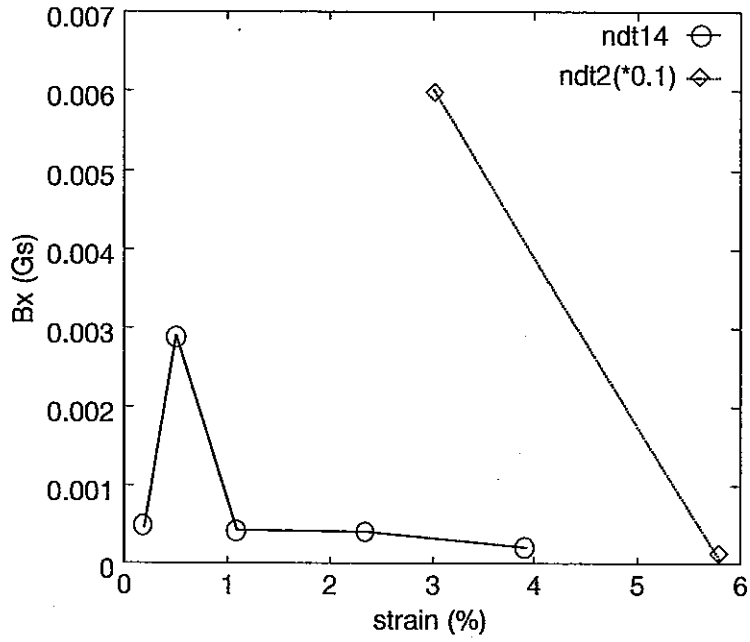

Fig.341 The decrement of the plastic deformation induced magnetization for the test-piece NDT14 and test-piece NDT2

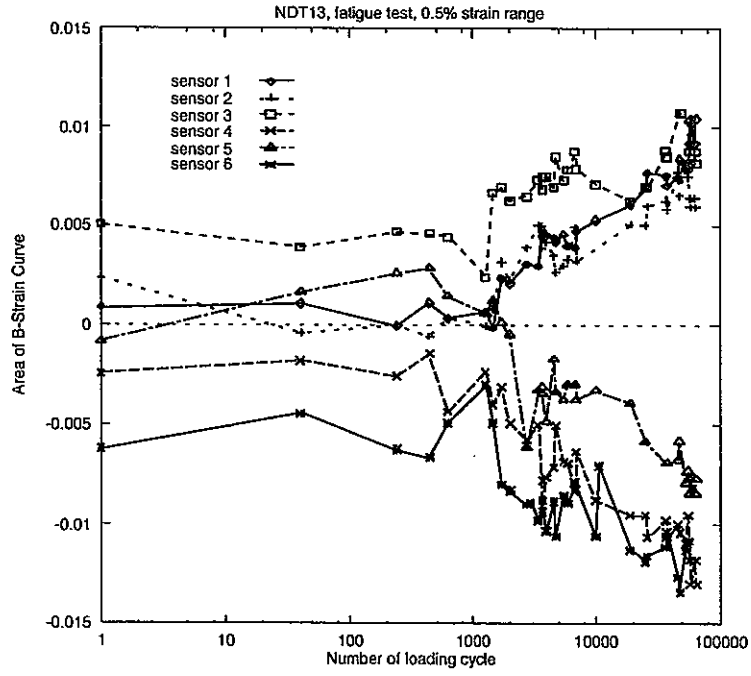

Fig.342 Evolution of the area of the $B-\varepsilon$ hysteresis curve during fatigue testing for test-piece NDT13

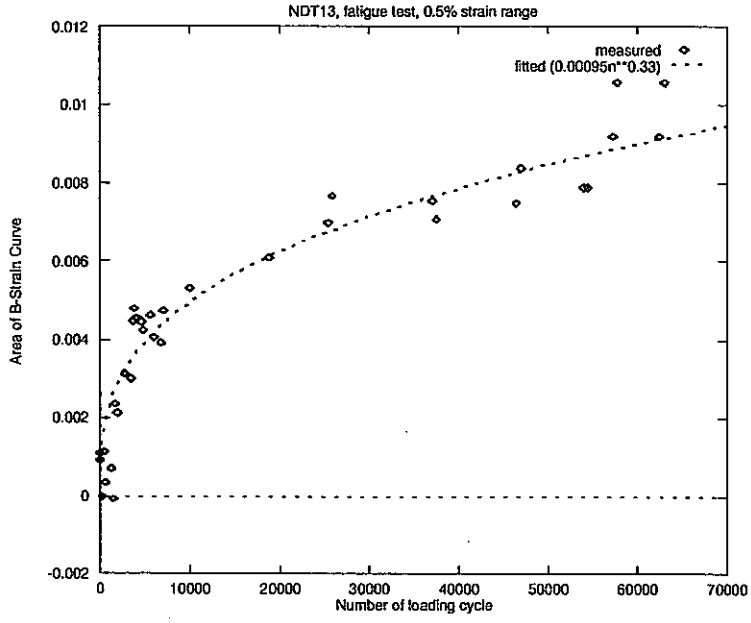

Fig.343 Evolution of the area of the $B-\varepsilon$ hysteresis curve during fatigue testing for test-piece NDT13 and sensor 1

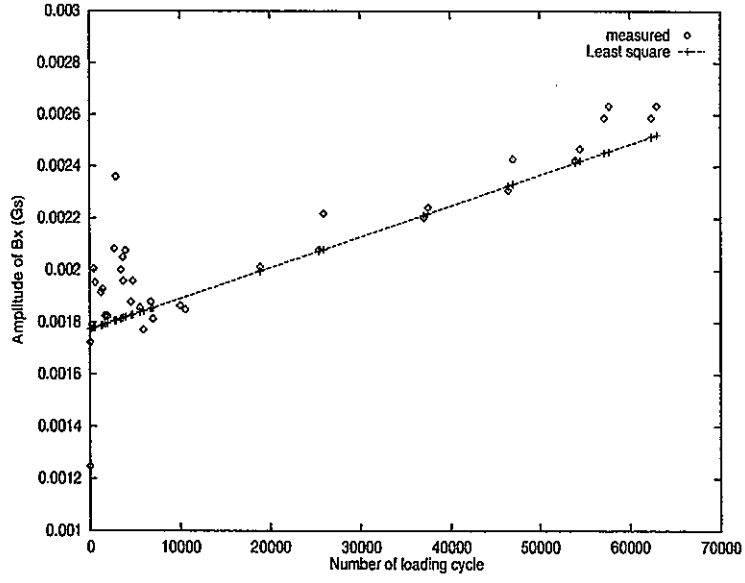

Fig.344 Correlation of the cycle number and the amplitude of the measured natural magnetic field

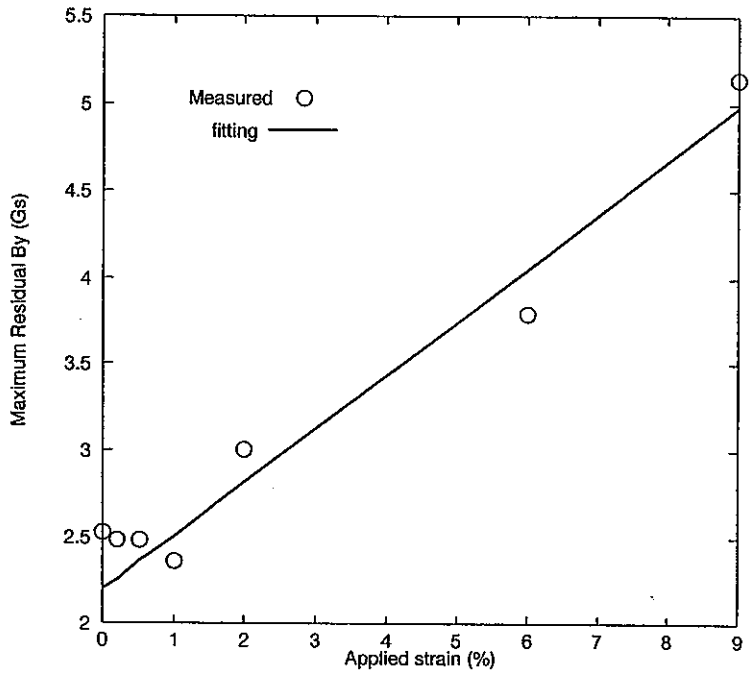

Fig.345 Correlation of the residual magnetic field and the applied plastic strain

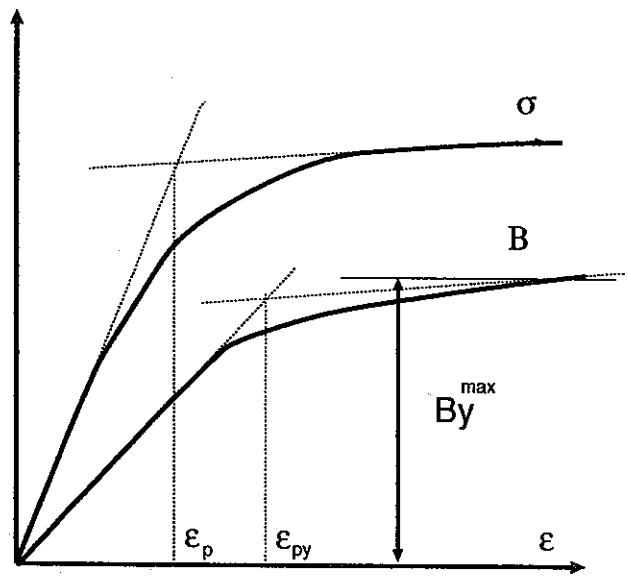

Fig.346 The concept diagram for the definition of the ε_p, ε_{py} and B_y^{max} used in table 5

Chapter 4

Reconstruction of Magnetic Charges in an Inspection Objest from the Detected Magneic Field Signals

Chapter 4

Reconstruction of Magnetic Charges in an Inspection Objest from the Detected Magneic Field Signals

4.1. Introduction

In the chapter 3, experiments are conducted for investigating the correlation between local plastic deformation and the corresponding magnetizations for the major structural material of FBR (SUS304 stainless steel). As the magnetization in material is impossible to be measured directly, the leakage magnetic flux density at a plan parallel with the testpiece surface has been measured. To predict the distribution of the magnetization in the material, an inverse analysis is necessary.

In this chapter, the approach for the reconstruction of the magnetization from the measured magnetic field is proposed. the magnetic charges are selected as the unknown parameters to be reconstructed in view of the equivalence of the magnetizations and a distribution of magnetic charges in the explanation of related physical phenomena[5]. Another motivation to choose charge as unknowns is for improving the condition number of the corresponding ill-posed inverse problem. Moreover, as an approximation of the practical problem dealing with a test piece in plane stress state, the charges are assumed constants in its thickness direction, i.e., only reconstruction of the magnetic charges in a two-dimensional distribution is considered. Three ways are adopted in the inversion procedure for evaluating there feasibilities. From examples using simulated signals, the least square method using a direct solver of linear equations is found hard to give a satisfactory reconstruction results, while the predicted charge profiles by using an iteration algorithm (the steepest descent method or conjugate gradient method) agree with the true distributions well for signals with a low noise level. In case of signals containing a relative large noise, the iteration method also failed to give acceptable solutions. To enhance its robustness, wavelet transformation is introduced to the equations discretized with the moment method to weaken

the constraint conditions. A strategy to select the weight coefficients is also proposed based on the wavelet decomposition of the reconstructed functions. Numerical results show that the method using wavelet can give good reconstruction even for signals with a noise level over 50%, which demonstrated the validity of the strategy.

4.2. Reconstruction of magnetic charges

The magnetic charge is a concept introduced referring to the definition of the electric charge. Though experimental results do not support the practical existence, the magnetic charge still keeps as an important physical quantity in view of its equivalence with the current dipole model for describing many physical phenomena. Concerning the bad condition number of the ill-posed inverse problem in the reconstruction of the magnetization vector, choosing the amplitude of magnetic charges as unknown parameters is much more reasonable in order to imag the magnetizations inside the object. Moreover, such a treatment can also result in a significantly reduced number of unknowns in the inverse analysis, or in other word, can save much computer burden.

At a field point (denoting as $\mathbf{r}$) outside the volume V of the magnetized object, the magnetic scalar potential induced by the magnetization at a source point (denoting as $\mathbf{r}'$) is equivalent to that induced by a related magnetic dipole. Refering to formulae for magnetic dipoles, the magnetic scalar potential due to magnetizations can be expressed as[8],[9]

$$\phi(\mathbf{r}) = \frac{1}{4\pi\mu_0}\int_V \mathbf{m}(\mathbf{r}')\cdot\nabla'\frac{1}{|\mathbf{r}-\mathbf{r}'|}dv' = \frac{1}{4\pi\mu_0}\{\oint_\Omega \mathbf{m}(\mathbf{r}')\cdot\mathbf{n}\frac{1}{|\mathbf{r}-\mathbf{r}'|}ds' + \int_V \nabla'\cdot\mathbf{m}(\mathbf{r}')\frac{1}{|\mathbf{r}-\mathbf{r}'|}dv'\}, \tag{4.1}$$

where, $\phi(\mathbf{r})$ is the magnetic scalar potential at the field point $\mathbf{r}$ in air region, $\mathbf{m}(\mathbf{r}')$ is the magnetization vector at the source point $\mathbf{r}$, $q(\mathbf{r}') = \nabla'\cdot\mathbf{m}(\mathbf{r}')$ is magnetic charge density at point $\mathbf{r}'$ according to its definition, and $\mathbf{m}(\mathbf{r}')\cdot\mathbf{n}$ is the surface charge density at a surface point with $\mathbf{n}$ being its normal unit vector.

From eq.(4.1), it is not difficult to find that the effect of the magnetization is equivalent to that caused by both the volume and the surface charges. For a button type CCT test piece under a loading of plane stress state, the surface magnetic charges at the planar and side surfaces are zero considering the symmetry condition and the vanishing property of the total charge. Moreover, for a problem dealing with magnetizations nearby the tips of cracks initiated at the central part of a test piece, the magnetic charges at the other surfaces can also be neglected. Under such conditions, the formula for the flux density induced by the charges can be obtained by taking gradient operation at the two sides of eq.(4.1) but with the term of surface integral omitted. eq.(4.2) shows the correlation of the flux density and the volume distributed magnetic charges which will be used as the basic governing equation in the following part,

$$\mathbf{B}(\mathbf{r}) = \frac{1}{4\pi}\int q(\mathbf{r}')\nabla'\frac{1}{|\mathbf{r}-\mathbf{r}'|}dv', \tag{4.2}$$

where, $\mathbf{B}(\mathbf{r})$ is the leakage flux density vector at the field point $\mathbf{r}$.

4.2.1 Inversion with the least square method[11],[12],[13]

In the follows, we consider the magnetizations localized in a limited volume V as described in the previous sections. By subdividing V into $\bar{n}'$ cells and taking the charge density as a constant value in each cell, the magnetic charges in any source point $\mathbf{r}'$ can be approximated as,

$$q(\mathbf{r}') = \sum_{j}^{\bar{n}'} q_j \xi_j(\mathbf{r}') \tag{4.3}$$

where, $\xi_j(\mathbf{r}')$ is a box function with a zero value outside and a unit value inside the $j-th$. cell.

Substituting the discretization equation into eq.(4.2), some calculation shows that the leakage flux density $\mathbf{b}(\mathbf{r}_i)$ at an arbitrary field point $\mathbf{r}_i$ can be obtained from the discretized charge parameters with the following formula,

$$\mathbf{b}_i(\mathbf{r}) = \sum_{j}^{\bar{n}'} \frac{1}{4\pi} v_j \frac{(\mathbf{r}_i - \mathbf{r}'_j)}{|\mathbf{r}_i - \mathbf{r}'_j|^3} q_j. \tag{4.4}$$

Similarly, a component of the leakage flux density vector (for instance, the x component $\{q_x\}$) at $\bar{n}$ inspection points connects to the charge parameters under governing of the following system of equations,

$$\{b_x\} = [K]\{q\} \tag{4.5}$$

with the coefficient $k_{ij} = \frac{1}{4\pi} v_j (x_i - x'_j)/|\mathbf{r}_i - \mathbf{r}'_j|^3, i = 1, 2, ..., \bar{n}, j = 1, 2, ..., \bar{n}'$.

Theoretically, the charge parameters can be obtained by solving eq.(4.5) with $\{b\}$ using as a component of the measured flux density vector. Of course, eq.(4.5) can not be solved directly as it is usually an over defined or a less defined problem, in other word. $\bar{n} \neq \bar{n}'$. To find a reasonable solution of such a system of equations, the least square method is an usual way which solves the system of equations from a point of view of minimizing the square residual. The system of linear equations derived with the least square method is as follows,

$$[K]^T\{b\} = \{[K]^T[K]\}\{q\}. \tag{4.6}$$

Unfortunately, matrix $[A] = [K]^T[K]$ usually is in a bad condition number, i.e, the solution of eq.(4.6) is not unique from a rigorous point of view. One can only obtain a severely vibrated solution if a normal elimination algorithm is employed in its solving. In other word, the solution is easy to fall into a local minimum in the residual function because of the ill-poseness of the inverse problem. Fig.4.1 gives an example of the solution for an 1-D distribution of magnetic charges. From this result, it is not difficult to find that only a very small difference existed between the magnetic fields produced by the reconstructed and true charges while the charges themselves have a much different distribution. Therefore, the ill-posed problem need to be regularized somehow in order to obtain an acceptable solution.

In practical, magnetic charges in a severe oscillated distribution usually is not realistic. Imposing the solutions satisfy constraints based on such a priori knowledges is the basic idea to regularize the ill-posed problem. In next subsection, a method of iteration using gradient will be introduced for this purpose.

4.2.2 Inversion with the steepest descent method[14],[15],[16]

To avoid falling into the local minimum in solving the system of equations, an iteration method can gives a better solution when an appropriate initial profile can be determined somehow. Actually, once the boundary condition of the parameters to be reconstructed was known, such an initial condition is not too difficult to be selected, e.g, we can choose zero distribution if we know that the values at the boundary is vanished.

An iteration method using gradient has a superior convergence speed than a zero order algorithm. In addition with the considerations previously mentioned, we choose the method of steepest descent method or its accelerated version (the conjugate gradient method) to solve the eq.(4.6). The basic procedure of the method is as follows:

By choosing the objective function as the square residual of the magnetic field, eq.(4.6) can be transformed into an optimization problem which minimizes the objective function subject to a prior knowledges on the charge distribution. Denoting ε as the residual function, it can be defined as,

$$\varepsilon_m = \sum_i^i w_i[b_i^{obs} - b_i(\{q\}^m)]^2, \tag{4.7}$$

where, w_i is one of the weight coefficients, b_i^{obs} is an observed data of magnetic flux density and $b_i(\{q\}^m)$ is a field data due to an estimated charge distribution at $m-th$ iteration step, say, $\{b(\{q\}^m)\} = [K]\{\{q\}^m\}$.

The iteration formula for solving eq.(4.7) reads,

$$\{q\}^m = \{q\}^{m-1} + a_n\{f\}^m, \tag{4.8}$$

where, $\{f\}^m = \{\partial\varepsilon_{m-1}/\partial q_i\} + G_m\{f\}^{m-1}$, and $\{\partial\varepsilon_{n-1}/\partial q_i\}$ is a gradient of the objective function at the direction along $i-th$ coordinate vector which can be calculated from the coefficient matrix $[K]$ as,

$$\frac{\partial\varepsilon_{m-1}}{\partial q_j} = 2\sum_{i=1}^{\bar{n}} k_{ij}[b_i^{obs} - b_i(\{q\})], \quad j = 1, 2, ..., \bar{n}' \tag{4.9}$$

The updating step length a_n in eq.(4.8) is usually chosen as $a_m = P/Q$, and with

$$P = \sum_{i=1}^{\bar{n}}(b_i^{m-1} - b_i^{obs})\frac{\partial b_i^{m-1}}{\partial a_m}, \qquad Q = \sum_{i=1}^{\bar{n}}\left|\frac{\partial b_i^{m-1}}{\partial a_m}\right|^2. \tag{4.10}$$

and,

$$\frac{\partial b_i^{m-1}}{\partial a_m} = \sum_{j=1}^{\bar{n}} k_{ij}\frac{\partial\varepsilon^{m-1}}{\partial q_j} \tag{4.11}$$

Using the algorithm just conducted, a code for reconstructing an 1-D or a 2-D distribution of charge has been developed and reconstruction with use of simulated input signals has been successfully carried out. The details of the numerical simulation will be presented in the next section.

4.2.3 Application of wavelet to the inversion analysis[17],[18],[19],[20]

Imposing eq.(4.6) to be exactly satisfied at each selected measuring points is a strong constraint on the unknowns which may worsen the ill-poseness of the problem. An approach to weaken such a constraint is to use the moment method, i.e., only ask the equations to be satisfied from a point of view of weighted average. In this category, the Galerkin approximation is usually applied which chooses the weight function as the bases used in the discretization of the unknown variable. Hereafter, this strategy will be selected to establish the system equation of the inverse problem given in section 3.2.

As the magnetic charges possibly exist with a complicated distribution in the material to be inspected, discretizing it on basis of the wavelet functions is an attractive idea considering the merits of the wavelet transformation and wavelet decomposition for treating signals with abrupt change. Taking an 1-D problem as example, the Galerkin approximation using wavelet can be described as follows:

At first, we expand the charge function and the function of singular kernel $g(x,x')(\equiv (x-x')/|\mathbf{r}-\mathbf{r}'|^3$ for x component) in eq.(4.2) on the Daubechies' wavelet bases as,

$$q(x') = \sum_j c_{n,j}\phi_{n,j}(x) \tag{4.12}$$

$$g(x,x') = \sum_j \alpha_{n,j}(x)\phi_{n,j}(x'). \tag{4.13}$$

where, n is the resolution level, j is the shifting parameter, N is the index of the mother wavelet and $\phi_{n,j}(x) = 1/2^{n/2}\phi(2^n x - j)$ with $\phi(x)$ being the mother wavelet of the Dabechies basis which is supported at $(0, 2N-1)$. $\alpha_{n,j}$ can be calculated by numerically calculating the integral $\alpha_{n,j}(x') = \int g(x,x')\phi_{n,j}(x)dx$.

Substituting eq.(4.12),(13) into eq.(4.2), the x component of the flux density can be expressed as,

$$b_x(x) = \int_\Omega \sum_i \alpha_{n,i}(x)\phi_{n,i}(x') \sum_j c_{n,j}\phi_{n,j}(x')dx'. \tag{4.14}$$

Assuming that the supports of the wavelet bases are contained in the integral region Ω, we can obtain the following equation by applying the orthogonal property of the wavelet bases,

$$b_x(x) = \sum_{i=2-2N}^{2^n-1} \alpha_{n,i}(x)c_{n,i}. \tag{4.15}$$

Choosing the bases for wavelet expansion as the weight function, i.e.,multiplying $\phi_{n,i}(x)$ at the two side of eq.(4.15) and taking integration over its support, we can obtain the system of equations for the unknown wavelet coefficient as,

$$\beta_{n,j} = \sum_{i=2-2N}^{2^n-1} h_{n,ji}c_{n,i}, j = 2-2N, ..., 2^n-1. \tag{4.16}$$

or written in a matrix form,

$$\{\beta\} = [H]\{c\}, \tag{4.17}$$

where, $\beta_{n,j} = \int b_x(x)\phi_{n,j}(x)dx$ is the wavelet coefficient of the detected magnetic field data, and matrix element $h_{n,ji} = \int\int g(x,x')\phi_{n,j}(x)\phi_{n,i}(x')dxdx'$.

From the reconstruction results, the parameters at a lower resolution level can be obtained by using the following Mallat's decomposition equation,

$$c_{n-1,k} = \frac{1}{2}\sum_j c_{n,j} p_{j-2k}, \tag{4.18}$$

with $p_k (k = 0, 1, ..., 2N - 1)$ being the filtering coefficient of the Daubechies' wavelet.

To solve eq.(4.17), the gradient method given in the preceding subsection is applicable without much modification. Moreover, as the coefficient matrix $[H]$ is independent of the charge parameters, they can be precalculated and stored in data-bases for some selected resolution level and lift-off values. This procedure make the matrix $[H]$ possibly to be formed by just reading in the precalculated data-bases. Therefore, most of the computational burden can be reduced in a practical reconstruction especially for a 2-D or 3-D problem.

In addition to the capability to improve the ill-poseness of the inverse problem, the application of wavelet as the expansion bases and weight functions can also reduce the affect of noises because of the filtering effect of wavelet transformation. This means a slowly changed charges can be reconstructed well from a noisy signal with use of a low resolution level. Even for charges with abrupt spatial change, the reconstruction can be improved by designating the charge distribution reconstructed at a low resolution level as initial values of the high level reconstruction.

A general way to select the weight coefficients used in the weighted square residual is still an unclarified problem. Usually, the coefficient for a signal of relative small signal has to be selected as a small value concerning the relative small S/N ratio there. However, these coefficients are difficult to be directly determined from the measured data in case of a high noise level. Bearing in mind these considerations, we propose a strategy to determine the weight function by using the features of the wavelet function. The basic idea of the method is to apply the reconstructed results at a low resolution level or decomposed coefficients from a result at high resolution level . As the affect of noise is small in a low resolution level, taking the corresponding normalized magnetic field as the weight coefficients can reduce the affect of noise further, i.e.

$$\{w_i\} = [K]\{q\}_n, \tag{4.19}$$

where $\{q\}_n$ is the reconstructed charge parameters at resolution level n with $q_{n,i} = \sum c_{n,j}\phi_{n,j}(x_i)$.

4.3. Numerical results

The formulae of the steepest descent method were implemented for both an 1-D and a 2-D problem while those using Galerkin approximation and wavelet was implemented for a 1-D problem only. For the 1-D problem, charges located at a line in 20 mm length is reconstructed from magnetic field measured along a line with 1 mm or 5 mm lift-off (Fig.4.2 a). The scanning region is selected as in 30 mm length just over the line of source. It is also assumed that the charges at the boundary and outside the region are zero. The 2-D

problem is an extension of the 1-D case (Fig.4.2 b). In this case, the charges are assumed located in a square region of size 20 × 20 mm. The field data are of either a horizontal component or the normal component of the flux-density vector which were acquired from a 2-D scanning in a 30 × 30 mm region h_0 over the source plane. The simulated magnetic field as well as those measured from the experiment are adopted in the reconstruction. Artificial white noises are added into the input data for investigating the robustness of the analysis method. In the follows, the numerical results will be presented respectively for the direct and wavelet used method.

4.3.1 Results of the least square method

a). 1-D problem

Fig.4.3 depicts a comparison of the reconstructed and the true distribution of the magnetic charges. In this case the initial values of the charges are selected as zero and no noise was included in the input data. Unlike the result using Gauss elimination method, very good convergence was realized in a short CPU time. In this case, both the conjugate gradient method and the steepest descent method give excellent results though the conjugate gradient method can converge in a much less iteration number.

Once noise was added into the inputed data, the convergence of the iteration was very slow and even become unstable for the conjugate gradient method. For the steepest descent method, as a result of the random noise the residual value can not decreased to a level designated previously, and the square residual between the predicted charges and the true values do not decrease with the reducing residual of the magnetic field. From lot of reconstruction testings for various of input data and noise level, we find that after about 50 ∼ 100 iterations, a relative good reconstruction of the charges can be realized. More iterations may not improve the charge distribution significantly even make worse. Therefore, we decide to take the reconstructed result at 100 iteration as the final values in practical applications. Fig.4.4 shows the evolution of the square residual during iteration when different noise was added into the input signals. We can find that 60 iteration is an appropriate number to stop the iteration.

Fig.4.5 shows a simulated results for signals with 20% and 50% noise. We can find that it is difficult to distinguish the true charges from the result of 50% noise. Therefore, more efforts are needed to improve the robustness of the method.

b). 2-D problem

Fig.4.6 gives results for a two dimensional problem with the initial profile of the charges selected as zero. The applied 2-D model corresponds to the experiment described in the section 2 with an assumption that the charges do not change too much in the thickness direction. The result shown in Fig.4.6 is a comparison of the reconstructed and the true distribution of the charges when the simulated signals with zero noise was applied. The corresponding comparison of magnetic field is shown in Fig.4.7. We can find that even for

a two dimensional problem, the gradient method can gives excellent reconstruction results.

For investigating the robustness for a 2-D problem, the reconstruction was also performed with signals including artificial noise. Fig.4.8 (a) is a reconstruction result for signal with 20% noise. Fig.4.8 (b) gives the corresponding magnetic field. We can find that a relative good reconstruction was obtained again. For a magnetic charges with a more complicated distribution, it can also be reconstructed in a short CPU time. Fig.4.9 depicts results of a typical example for such a problem.

4.3.2 Results of the wavelet used Galerkin method

Fig.4.10 shows a reconstruction result using the wavelet method with the resolution level chosen as 6 and the lift-off as 1.0 mm. The other conditions are the same as that described in section 4.1. The initial values were also used as zero. Though there are some errors in the location where the charges change abruptly, satisfactory reconstruction results is obtained. The iteration number of this result is taken as 100.

For comparison of the results of the gradient method and that of the method using wavelet, several reconstruction were performed for signals including artificial noise. Fig.4.11 gives an example of 1-D problem with the same condition as described in the preceding subsection. A noise level of 50% was applied and the iteration number was chosen as 100 for both methods. One can find that the reconstruction result using wavelet has a relatively better precision.

Up to now, the results presented are reconstructed with the weight function used as 1 or in other word, the weight function was not introduced. By applying the weight function proposed in the section 3.3, it is not difficult to find that the reconstruction results can be improved. Fig.4.12 shows an example with an 1-D problem for signals with 20% noise. From this figure we can find that the application of the weight coefficients can improve the results of charge distribution significantly.

4.3.3 Reconstruction with measured data

The reconstruction results given in preceding subsections are obtained by using simulated data of magnetic field. Though these results are important for evaluating the feasibility of proposed methods, more validation is necessary for practical flux density data in order that the method possibly be applied to real problems. For this purpose, magnetic field data shown in Fig.3.22 was applied to the reconstruction using the 2-D code of the gradient method. Fig.4.13 depicts a reconstructed distribution of charges in the planar region of the test-piece. The magnetic field produced by the reconstructed charges is shown in Fig.4.14. The magnetic field due to the predicted charges shows a good agreement with the measured data. Comparing the reconstructed distribution of charges with the position of fatigue cracks which has initiated at the two ends of the central slit, it also can find that the the reconstructed charges is in a reasonable distribution if one pays attention at the peaks corresponding to the crack tips. This result supports the expect-ion that the proposed method is suitable in the correlation analysis of magnetic and damage parameters.

4.3.4 Some discussions

As described in the preceding sections, some treatments on the selection of weight coefficients, the maximum iteration number and the component of magnetic flux density are introduced. As a highlighting, we summarize these considerations as follows:

To reconstruct the magnetic charges, one component of the flux density vector is enough. This is a fortunate fact as it is impossible to use more components in the inversion because the 3 components of flux density are not independent each other considering the vanishing divergence and rotation in the vacancy area. Usually, the normal component of the flux density vector is applied in the reconstructions concerning the affect of lift-off change. However, there is no much difference between the reconstruction results using different component for simulated data. This fact has been demonstrated when we try to find the affect of the different component. In case of our experiment, the lift-off do not varies much because of the application of x-y stager. On the other hand, the lift-off of sensor for the vertical is bigger than that of the horizontal one. Therefore, we decide to use the horizontal component in the reconstruction from the point of view of a high space resolution.

Once noise presented in the input data, selection of the threshold condition for convergence is of difficult. As described in section 4.1, we choose a given max. step number as the condition for different problems. This treatment can be explained by considering the property of the iteration method. In fact, at the iterations of low step number, the method try to find a solution which approaches to the measuring data from a globe point of view. After this procedure, the local distribution of the data is reconstructed in detail which may lead to a severe vibration in the solution because of the affect of noise. Therefore, using a maximum iteration number designated by experience is valid for our problems.

The application of weight coefficients can focus the inverter to the signals with a high S/N ratio. However, as we do not know the distribution of sources, designation of such coefficients is not easy. The method we proposed in the section 3.3 is to overcome this difficulty. The basic idea of this method is to choose the coefficient as magnetic field induced by an approximately reconstructed source. As the reconstruction at a low resolution level is very fast, this procedure does not need much computations. By designating a small value at the position of small field, the high S/N signals can make a full play in the inversion which, in turn, can improve the precision of the reconstruction results.

4.4. Concluding remarks

Based on the work described in the preceding sections, we come to the following concluding remarks.

1. The reconstruction of the magnetic charges from measured magnetic field is a typical ill-posed inverse problem. Solving of the system of equations of the least square method with an eliminate algorithm is impossible to give an acceptable solution.

2. In spite of the local minimum problem of an iteration algorithm using gradient method, it can give a satisfactory reconstruction result with use of a zero initial values. An acceptable charge distribution can be obtained by select an appropriate iteration number even for noise polluted signals.

3. The wavelet used Galerkin method can give a better reconstruction than that using the the least square method for signals with high noise level. It is also verified that applying the reconstructed magnetic field at a low resolution level as the weight coefficients used in the objective function can improve the robustness of the proposed inversion method.

4. From the natural crack signal measured from the testpiece with fatigue crack initited, the magnetic charges are reconstructed by using the gradient method. Comparing with the results measured by using the colloidal method, the recontructed result is reasonable which inturn verified the validity of the proposed method for the actual problem.

4.5. References

[1] R.B.Mignogna, and et al., Passive nondestructive evaluation of Ferromagnetic materials during deformation using SQUID gradiometers, IEEE Trans. Appl. Supercond., Vol.3, No.1, p1922-1925, 1993.

[2] M.Uesaka and et al.,Round-robin test for nondestructive evaluation of steel components in nuclear power plants, in Studi. Appl. Electromagn. mech., Vol.14, p39-48, 1999.

[3] A.Gilanyi and et al., Magnetic property assessment as basis for nondestructive evaluation for steel component in nuclear engineering, Nonlinear electromagnetic systems, IOS press, p190-193, 1996.

[4] N.Kasai and et al., A possibility for NDE of magnetic materials using SQUID, in Stud. Appl. Electromagn Mech., Vol.12, 95-101, 1997.

[5] K.Yamada, and et al, Nondestructive cross evaluations of iron-based materials by magnetic sensors and laser speckle interferometry, Proc. Int. Symp. Mag. Mater., 1998.

[6] Report of research committee on electromagnetofracture and its applications on nondestructive evaluation of degradation and damages, JSAEM report, JSAEM-R-9803, 1998.

[7] Y.Yamada, and et al., Application of thin-file flux-gate sensor, New Ceramics, No.2, p15-18, 1998.

[8] K.Miya, Electromagnetics and Electromagnetic Structure Analysis, Yokendo Lt.d, 1996.

[9] S.Chikazumi, Magnetics, Kyouritsu Publisher, Lt.d, 1969.

[10] A.Tarantola, Inverse problem theory, Elsevier, 1987.

[11] S.Kubo Inverse problem, Keifukan, 1993.

[12] Kurokawa K.Sugiyama, and K.Miya, An inverse analysis with the current vector potential T, Elsevier Stud. Appl. Electromagn. in Material, Vol.5, p197-200, 1994.

[13] S.J.Norton, and J.R.Bowler, Theory of eddy current inversion, J.Appl.Phys., Vol.73, No.2, 501-512, 1993.

[14] Z.Chen and K.Miya, ECT inversion using a knowledge based forward solver, J.Nondestr. Eval., Vol.17, No.3, p167-175, 1998.

[15] Z.Chen, An approach to reconstruction of a natural crack using signals of eddy current testing, I. Reconstruction of an idealized natural crack, JNC report, JNC TN9400, 99-009, 1999.

[16] I.Daubechies, Orthonormal baes of compactly supported wavelet, Common. Pure Appl. Math., Vol.47, No.7, p909-996, 1998.

[17] G.Mallet, A thoery for multiresolution signal decomposition: the wavelet representation, Commun. Pure Appl. Math., Vol.41, No.7, p674-693, 1998.

[18] G.Chen, K.Miya and A.Yamagochi, Inverse analysis for current potential using fast wavelet transform, in Stud. Appl. Electromagn. mech., Vol.8, p283-294, 1995.

[19] Z.Chen, Y.Yoshida and K.Miya, Analysis of relations between the defect shapes and the wavelet coefficients of ECT data, in Studi. Appl. Electromagn. mech., Vol.8, p295-302, 1995.

[20] Z.Chen and K.Miya, A wavelet based method for numerical calculation of singular integrals in eddy current analysis, Vol.119-A, No.7, IEEJ Trans., p957-964, 1999.

[21] I.Marinova, S.Hayano, N.Ishida, and Y.Saito, J. Appl. Phys., Vol.75, No.10, pp5904, 1994.

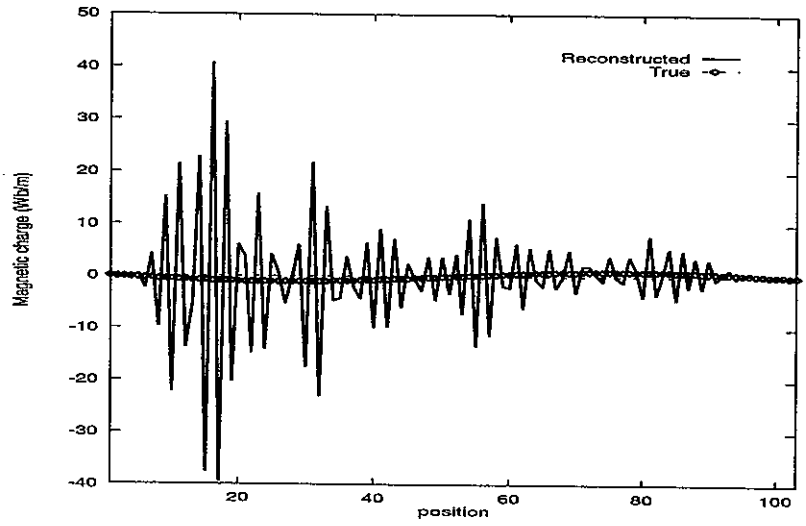

(a) magnetic charges

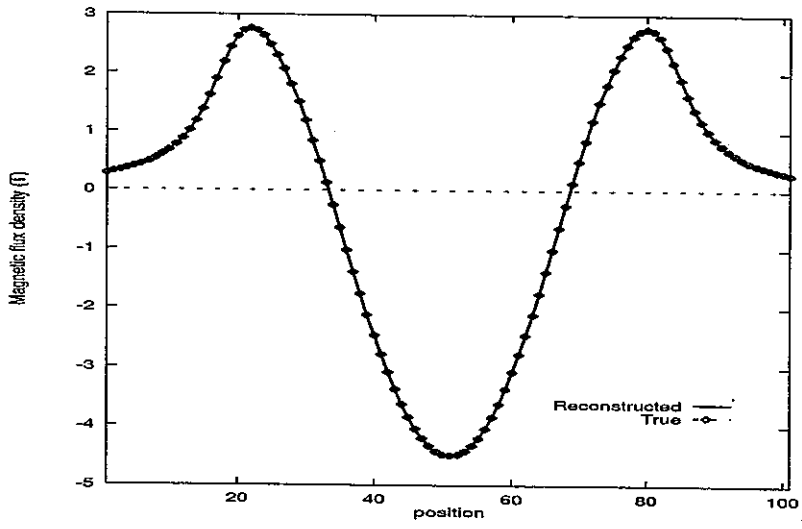

(b) Comparison of magnetic flux density

Fig.4.1 An example of result using elimination algorithm for equations of the least square method

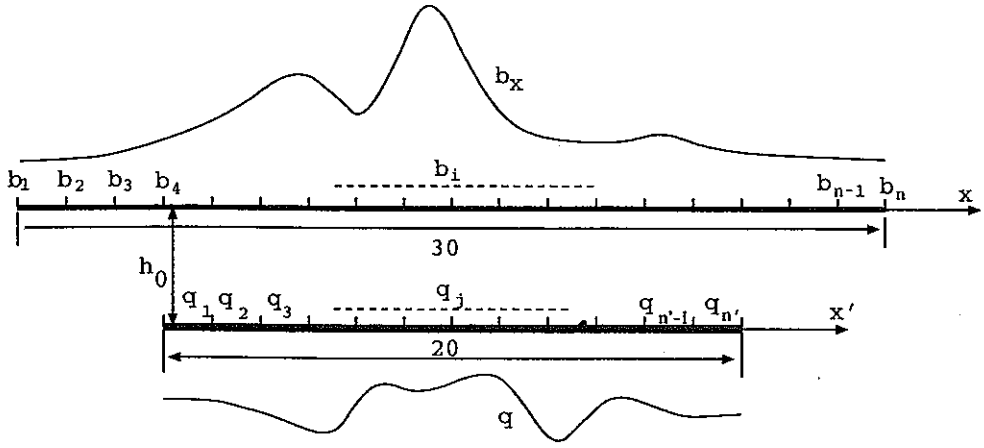

a) model of the 1-D problem

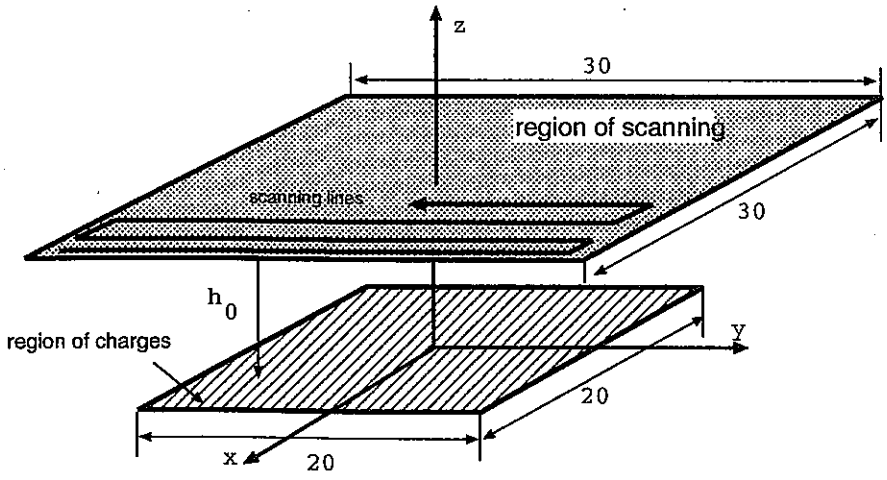

b) Model of the 2-D problem

Fig.4.2 Concept diagram of the problems

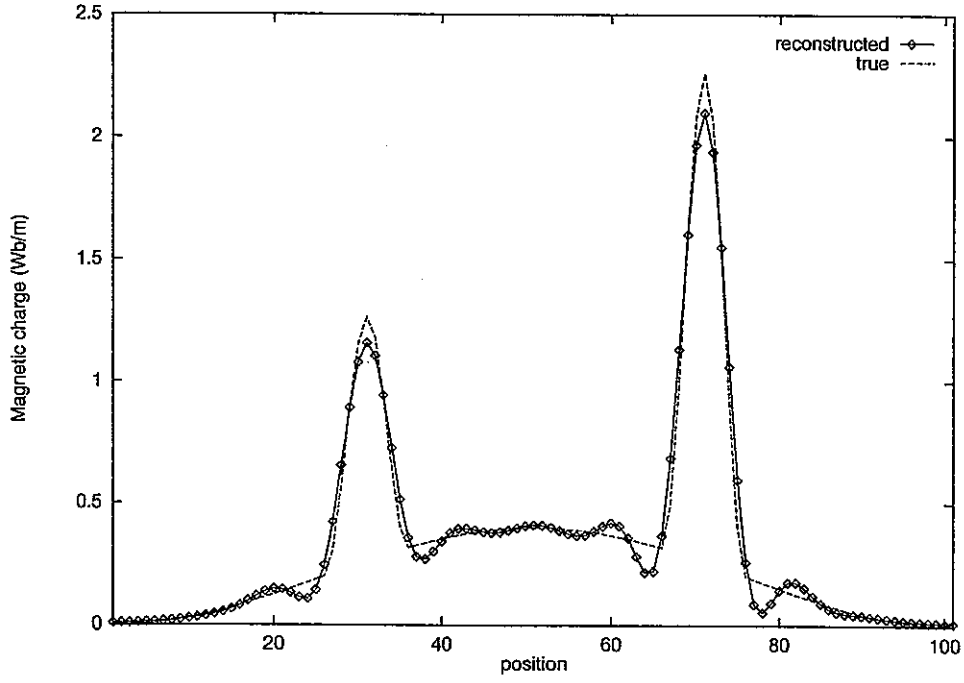

Fig.4.3 Comparison of reconstructed and the true distributions of 1-D charges from noise free signals by using gradient method and equations of the least square method

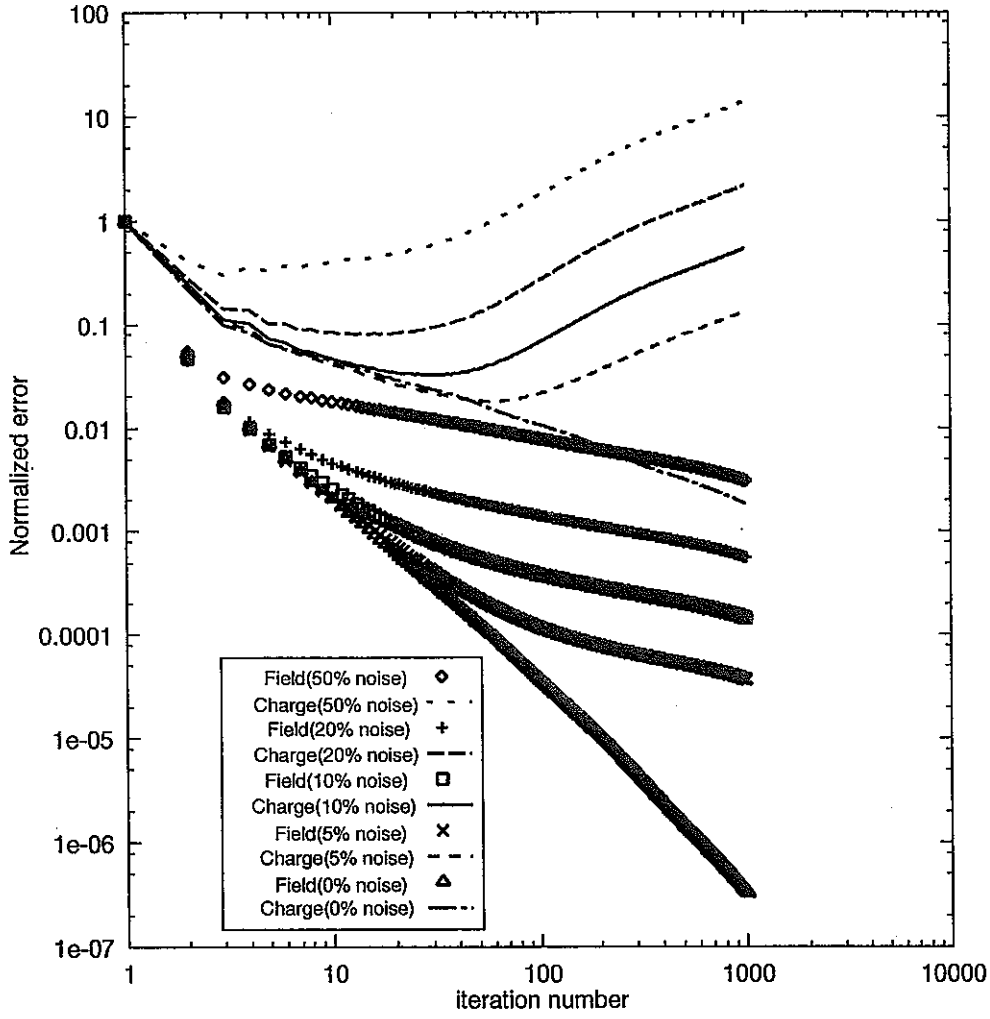

Fig.4.4 Evolution the residuals of the reconstructed field and charges for different noise level

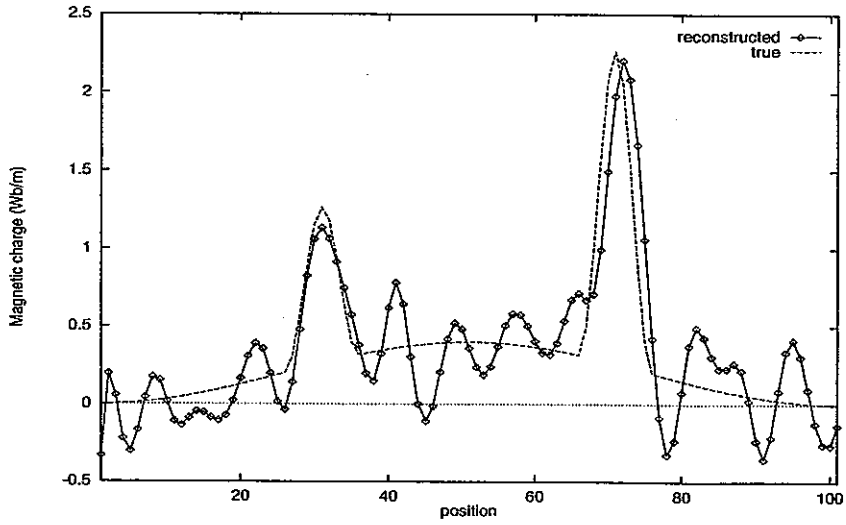

a). Result for signal with 20% noise

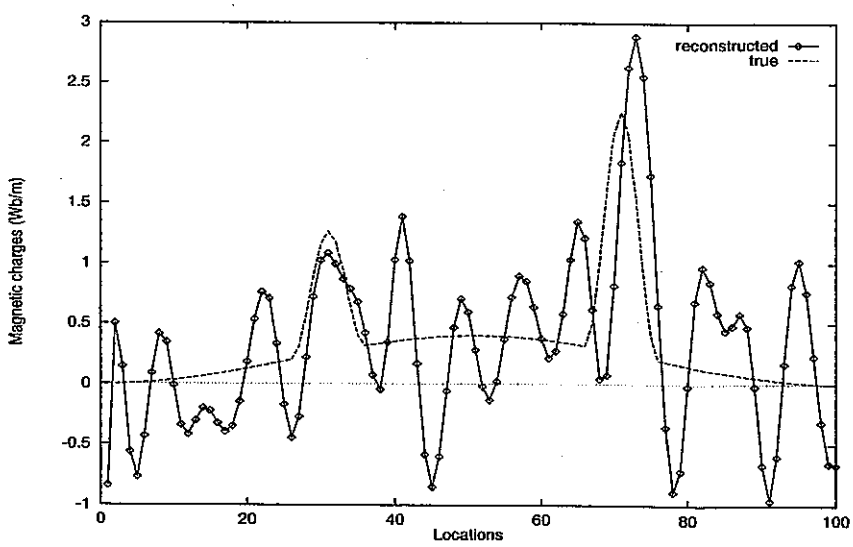

b). Result of signal with 50% noise

Fig.4.5 Reconstruction results of 1-D charges for signals with noise included by gradient method

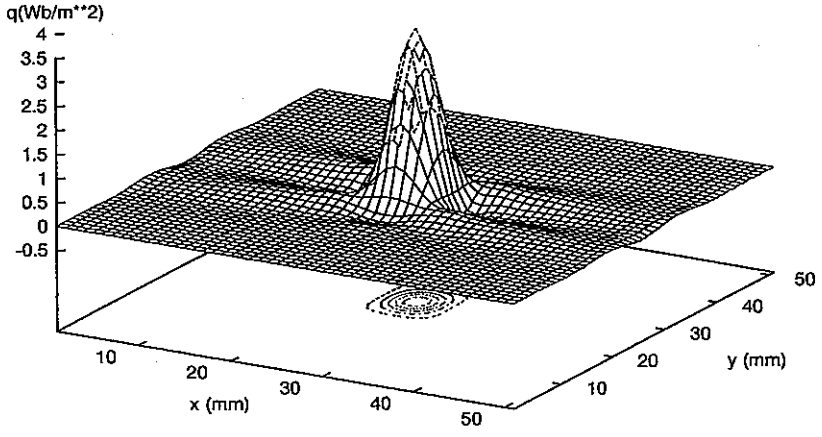

a). Reconstructed result

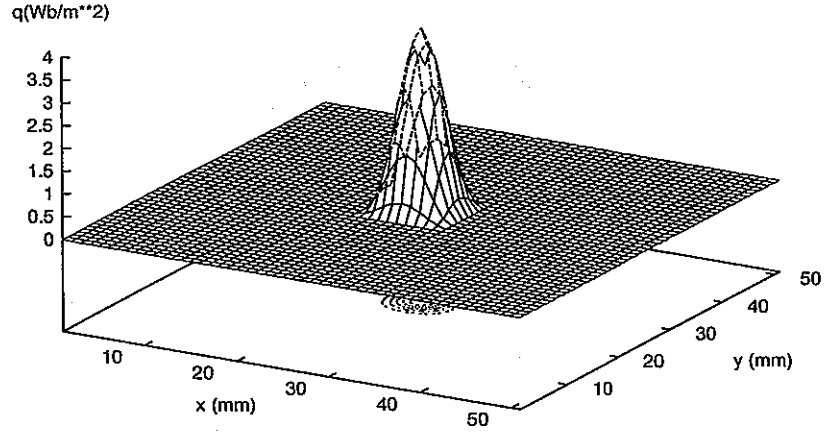

b). True distribution

Fig.4.6 Comparison of reconstructed and true distributions of 2-D magnetic charges by gradient method and the least square equations

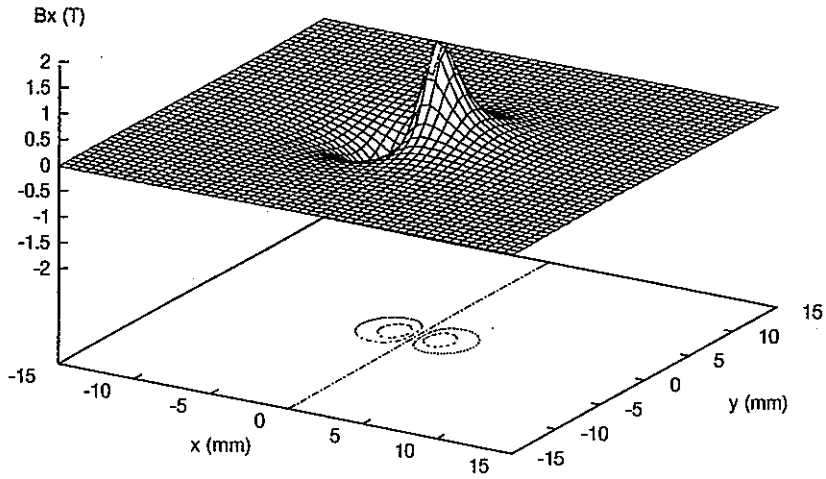

a). Reconstrcuted magnetic field

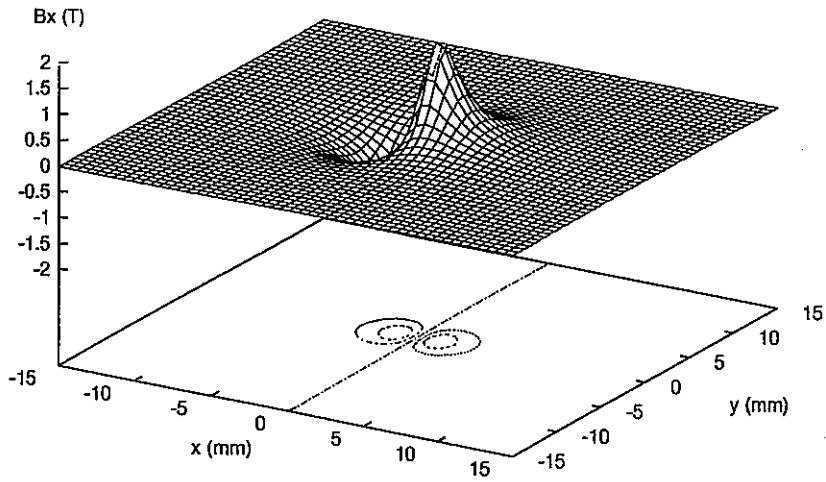

b). The true magnetic field

Fig.4.7 Comparison of reconstructed and true magnetic field

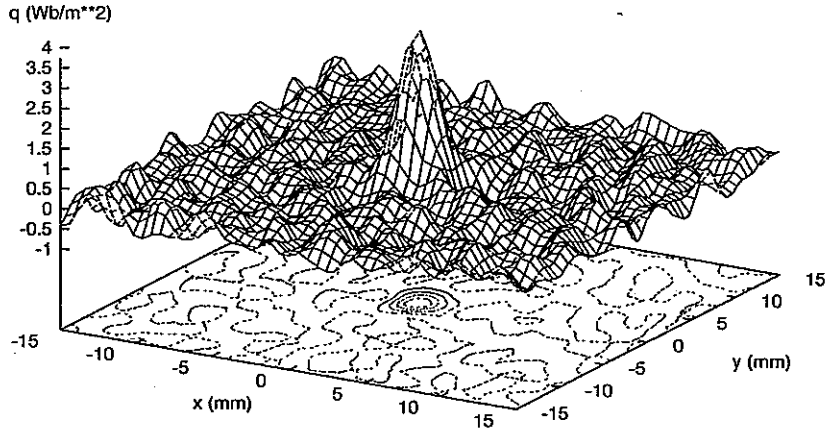

a). Reconstructed charges

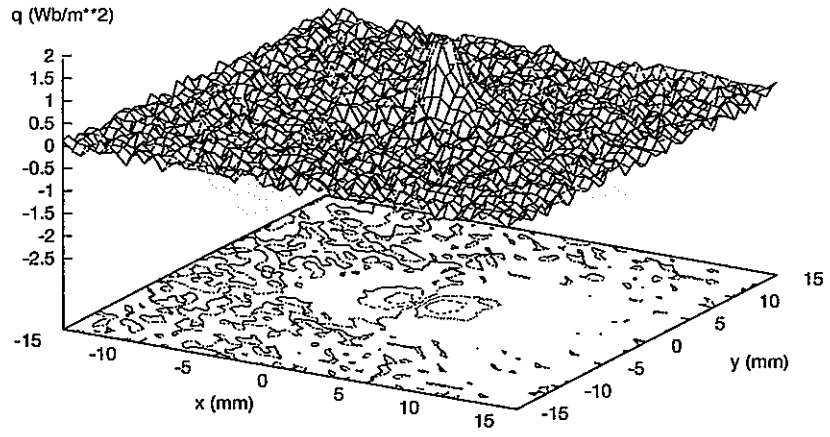

b). magnetic fileds due to reconstructed charges

Fig.4.8 Reconstructed results for signals with 20% noise distribution of leakage flux density

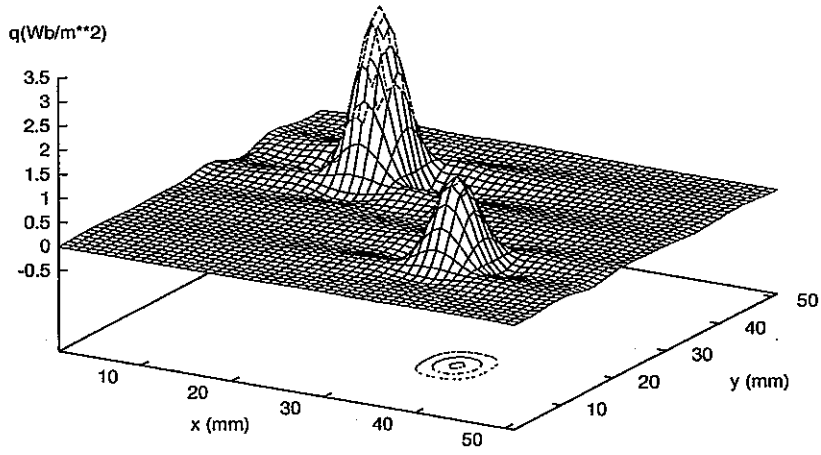

a). Reconstructed magnetic charges

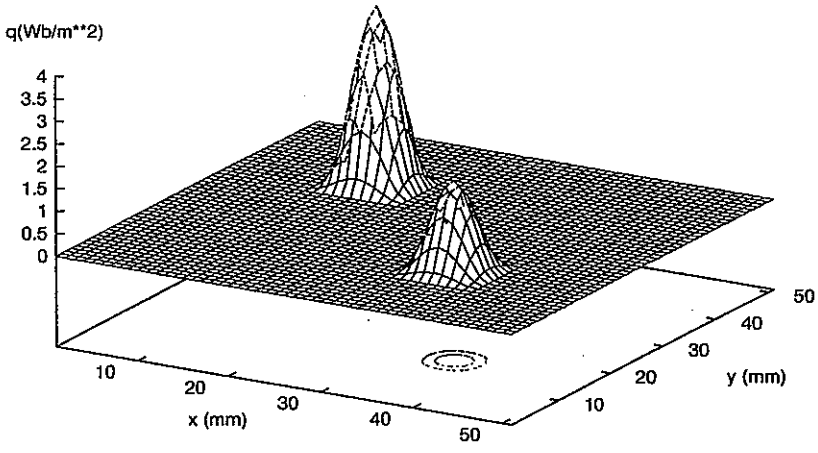

b). True distribution of magnetic charges

Fig.4.9 Reconstructed results for a more complicated distribution of 2-D magnetic charges distribution of leakage flux density

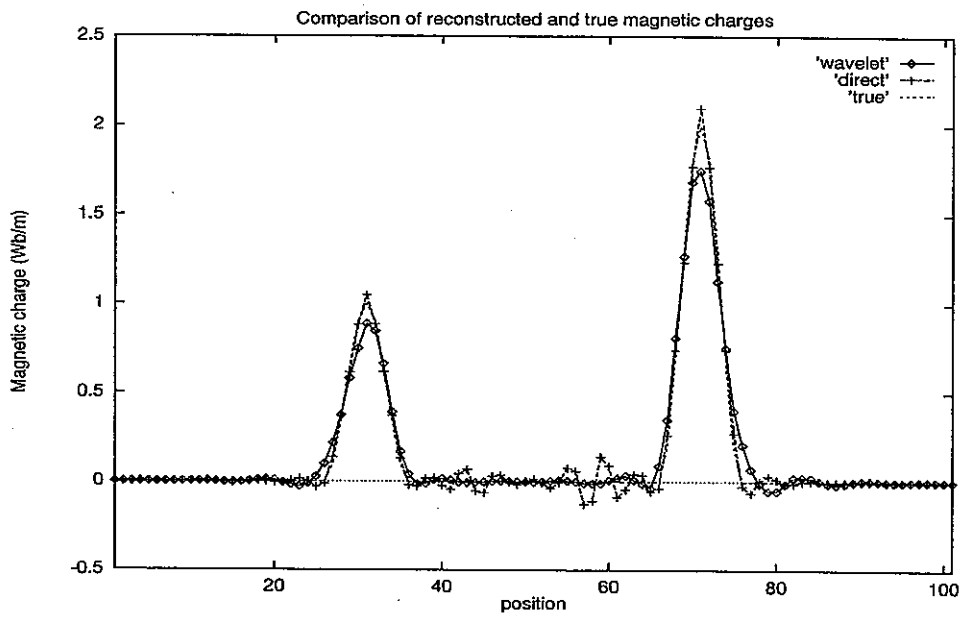

a). Comarison of reconstructed charges

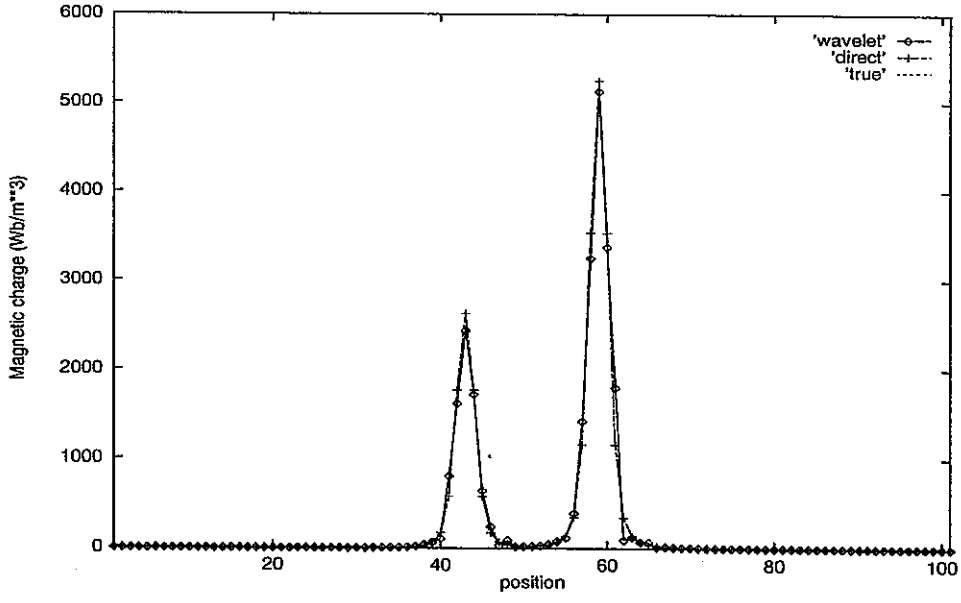

b). Comparison of reconstructed magnetic field

Fig.4.10 Comparison of reconstructed results of the wavelet based Galerkin method and of the least square method

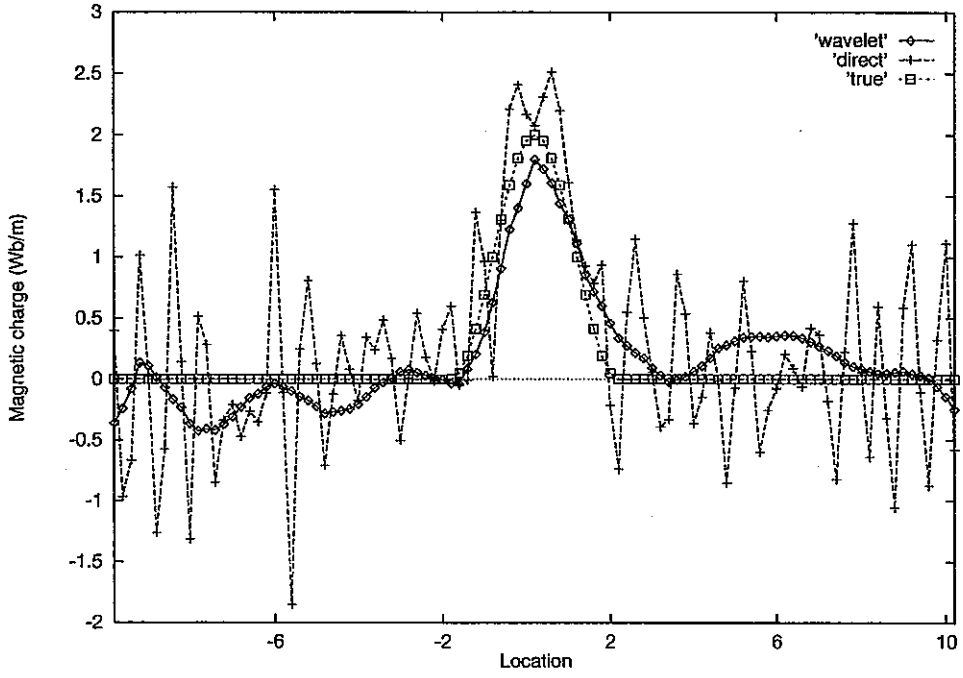

Fig.4.11 Comparison of reconstructed results of for signals with noise

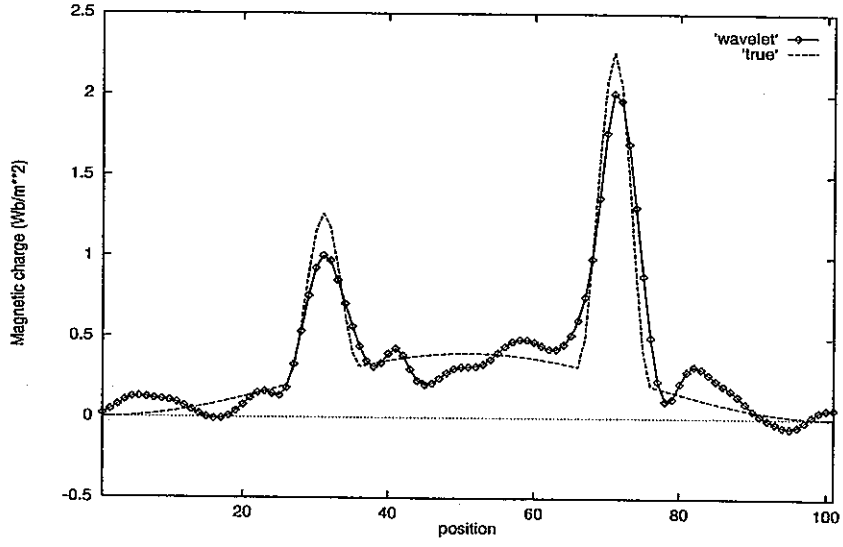

a).Reconstrcuted result with use of new weight coefficients
(wavelet, 1-D, 20\% noise)

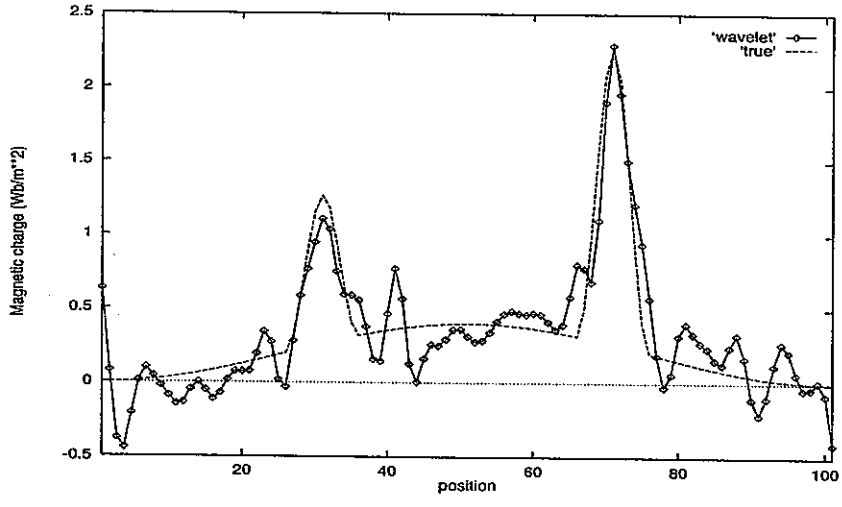

b). Reconstruction result without using weight coefficients
(wavelet, 1-D, 20\% noise)

Fig.4.12 Effect of proposed new weight coefficients

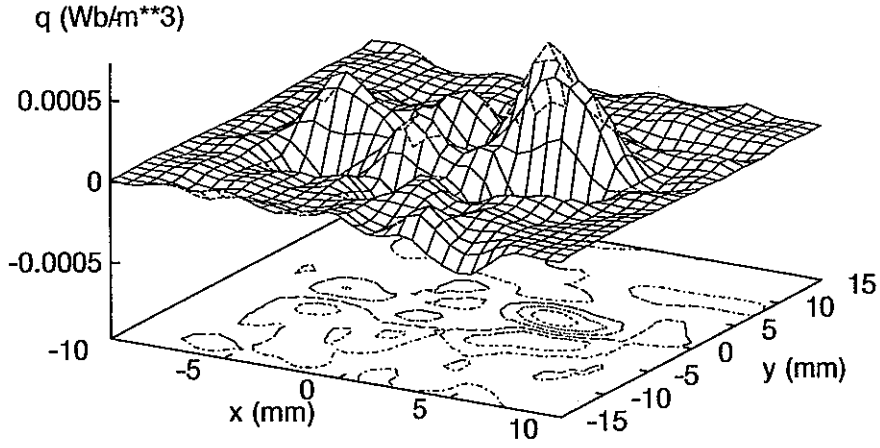

Fig.4.13 Reconstructed result from the measured magnetic field data

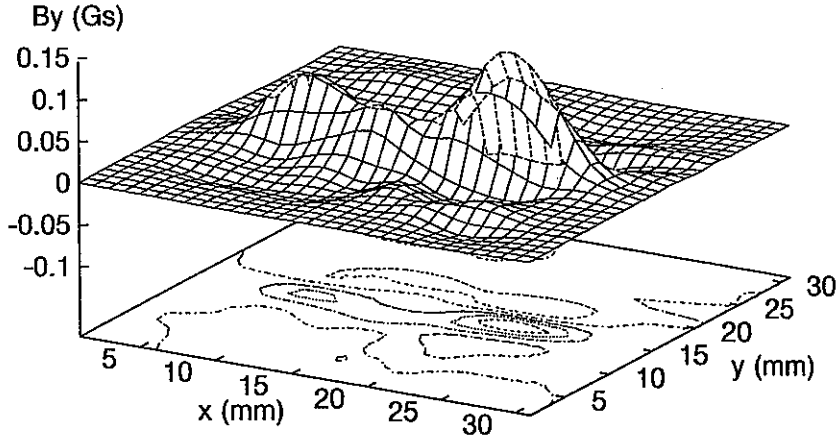

Fig.4.14 Comparison of the measured and the reconstructed distributions of the leakage flux density

Chapter 5

Conclusions and Prospects

Chapter 5

Concluding Remarks and Prospects

Based on the results described in the previous chapters, the following concluding remarks are obtained:

1. By proposing new crack models for a natural crack and extending the inverse scheme developed for the cavity notch, the reconstruction of a crack with non-vanishing conductivity is successfully realized at a personal computer. The simulation results shows that the two edge model of unknown constant conductivity is more efficient comparing with the conductivity model in view of both computational burden and accuracy, and is more suitable for signals including noise.

2. From the experimental work described in chapter 3, it is demonstrated that the natural magnetizations occurs for the SUS304 stainless steel due to a mechanical damage especially at the vicinity of the fatigue cracks. The measurement of the natural magnetic field can be considered as an efficient method for the NDE of fatigue cracks in such materials. The area of the field-strain hysteresis curve of the signals measured during the fatigue testing increases with the cyclic number, which can be applied to the online monitoring of the status of the fatigue damage for key structure components subjecting cyclic loadings. From the observation of the microstructure of the test-pieces containing plastic or fatigue damages, it is verified that the martensite transformation occurred for a relative large tensile loading in case of a flat test-piece, and occurred at the crack tips even for a fatigue testing of low strain range The material magnetic coefficient such as the residual magnetic field is possibly to be applied to detect the change of magnetic phase, and consequently, may be applicable for the detection of several damages before crack initiated.

3. In spite of the local minimum problem of an iteration algorithm using gradient method, the magnetic charge can be reconstructed in a satisfactory precision from the measured magnetic field signals by selecting proper initial value, iteration number and weight coefficients. In addition, the equation of Galerkin method using the Daubechies' wavelet is more robust against noise comparing with the results using

the least square method directly. From the natural magnetic flux leakage of the test-piece with a fatigue crack, the magnetic charges are successfully reconstructed by using the approach of the gradient method. The reconstructed distribution of charges qualitatively agrees with that measured by the colloidal method.

As prospects, the following works are important,

1. For the reconstruction of crack with touch, more work is necessary for the measured data and for the problems with a unknown position and unknown crack opening.

2. For the experiment, the correlation of the N/N_f and the feature parameter of the measured natural magnetic field for various test conditions and test-pieces is important. For applying maximum residual magnetic field B_r to the detection of damage and martensite transformation, to investigate the correlation of the N/N_f with the residual magnetic field is necessary.

3. For the inverse analysis of the magnetic charge, the validation of the wavelet used method for a 2-D problem and extension of the least square scheme to 3-D problems are necessary.

Acknowledgment

I would like to express my sincere gratitude to my cooperator Dr.Kazumi Aoto, Group leader of the Structure Safety Engineering Group, for his encouragement and constructive discussions throughout the 2 years period of this doctoral fellowship. I am particularly appreciative of the willing friendship of the members of the Kian Group for their various helps and cooperations. I am grateful to the JNC for financial supports and providing excellent experimental and office environment.

The author would like to thank Professor Kenzo Miya of the University of Tokyo for his competent advice at the very beginning of this subject. I owe special thanks to the members of the Research Committee of Electromagnetic Fracture Mechanics and Applications to Nondestructive Evaluation of JSAEM, especially professor Y.Nakasone of Tokyo University of Science, for valuable discussions and providing observation results of MFM and magnetic colloidal method. The FG sensors used in the testing are provided by the Shimatsu Corporation. The helps from Mr. Fujiyama of Shimatsu Corporation are sincerely acknowledged.

A sincere gratitude directs to Mr.Ishigami, Mr.Tomida, Mr.Sugaya and etc. of the JOY-O Industries Ltd. for their helpful cooperation during the fatigue testings, the microstructure observations and setting up my computer system that works very well throughout the period of this study.

List of Papers and Reports

1. Zhenmao Chen, Kazumi Aoto, and Kenzo Miya, Reconstruction of cracks with physical closure from signals of eddy current testing, IEEE Trans, Mag., July, 2000, (accepted for publication).

2. 陳、宮、高松、電磁非破壊検査の最近の進展 (I)、日本 AEM 学会誌、Vol.7, No.3, 278-282, 1999.

3. 陳、宮、高松、電磁非破壊検査の最近の進展 (II)、日本 AEM 学会誌、Vol.7, No.4, 382-392, 1999.

4. Zhenmao Chen, Kazumi Aoto, and Shyoichi Kato, A study on the correlation of magnetization and demages in SUS304 stainless steel, Proceedings of MAGDA'Brisbane, 2000.

5. Zhenmao Chen, Kazumi Aoto, and Kenzo Miya, Reconstruction of cracks with physical closure from signals of eddy current testing, Proceedings COMPUMAG'Sapporo, 298-299, 1999.

6. Zhenmao Chen, Kazumi Aoto, and Syoichi Kato, Reconstruction of magnetic charges using gradient method and wavelet, Proceedings 11th SEAD, 590-593, 1999.

7. Zhenmao Chen, K.Miya and M.Kurokawa, An approach to reconstruction of natural cracks using signals of eddy current testing, Stud. Applied Electromagn. Mech., Vol.15, 233-240, 1999.

8. Zhenmao Chen, and K.Miya, Fast reconstruction of crack shapes using eddy current testing, in Proceedings of JBSAEM Sophia, 1998.

9. Zhenmao Chen, Kenzo Miya and Kazumi Aoto, 渦電流探傷法を用いたき裂形状の再構成、日本材料学会第４７期第２回高温強度部門委員会講演会資料、16-25, 1998.

10. Zhenmao Chen, An approach to reconstruction of a natural crack using signals of eddy current testing, I. reconstruction of an idealized natural crack, Report of Japan Nuclear Cycle Development Institute, JNC TN9400 99-009, 1999.

11. Zhenmao Chen, Kazumi Aoto, and Syoichi Kato, Passive electromagnetic NDE for mechanical damage inspection by detecting leakage magnetic flux, (I. Reconstruction of magnetic charges from detected field signals) Report of Japan Nuclear Cycle Development Institute, JNC TN9400 99-061, 1999.

12. Zhenmao Chen, Kazumi Aoto, Syochi Kato and Yuji Nagae, Passive electromagnetic NDE for mechanical damage inspection by detecting leakage magnetic flux, (II. An experimental study on the correlation of natural magnetization and mechanical damages in the SUS304 stainless steel), Report of Japan Nuclear Cycle Development Institute, 2000 (in press).

13. Weiying Cheng, Kenzo Miya and Zhenmao Chen, Reconstruction of cracks with multiple ECT coils using a database approach, J. Nondestr. Eval., 1999 (in press).

14. Weiying Cheng, Kenzo Miya and Zhenmao Chen, Reconstruction of cracks with multiple ECT coils using database approach, Stud. Appl. Electromagn. Mech., Vol.15, 241-252, 1999.

15. Weiying Cheng, Zhenmao Chen and K.Miya, Reconstruction of multiple cracks from ECT signals using a dataabase aprroach, JSAEM Stud. Appl. Electromagn. and Mech, Vol.7, 169-174, 1998.